

UNDERSTANDING THE DAY-TO-DAY VARIABILITY OF THE
EQUATORIAL ELECTROJET

Gabriel Brando Soares

Tese apresentada ao Programa de Pós-graduação em Geofísica do Observatório Nacional, como parte dos requisitos necessários à obtenção do título de Doutor em Geofísica.

Orientador(a): Dra. Katia Pinheiro

Co-orientadores: Dr. Yosuke Yamazaki
Dr. Jürgen Matzka

Rio de Janeiro
Fevereiro de 2023

UNDERSTANDING THE DAY-TO-DAY VARIABILITY OF THE
EQUATORIAL ELECTROJET

Gabriel Brando Soares

TESE SUBMETIDA AO PROGRAMA DE PÓS-GRADUAÇÃO EM GEOFÍSICA
DO OBSERVATÓRIO NACIONAL COMO PARTE DOS REQUISITOS
NECESSÁRIOS PARA A OBTENÇÃO DO TÍTULO DE DOUTOR EM
GEOFÍSICA.

Examinada por:

Dra. Maria Alexandra Pais

Dra. Lívia Ribeiro Alves

Dr. André Wiermann

Dr. Andrés Reinaldo Rodriguez Papa

RIO DE JANEIRO, RJ – BRASIL
FEVEREIRO DE 2023

Gabriel Brando Soares - Ata.pdf

Documento número #dc35ca80-42f5-4e4f-983b-2392f7a09a7c

Hash do documento original (SHA256): 5c70f0ea12333c893932e2fc2591aed219f757b2a89d98899c3c8bb7adf35230

Assinaturas

✓ **GIANE DO CARMO BOLDRIM**

CPF: 004.446.047-31

Assinou em 12 dez 2022 às 09:39:20

✓ **KATIA JASBINSCHER DOS REIS PINHEIRO**

CPF: 086.710.057-55

Assinou em 08 dez 2022 às 07:33:10

✓ **LIVIA RIBEIRO ALVES**

CPF: 222.689.308-31

Assinou em 08 dez 2022 às 10:37:22

✓ **MARIA ALEXANDRA PAIS**

Assinou em 07 dez 2022 às 15:03:13

✓ **Juergen Matzka**

Assinou em 08 dez 2022 às 14:44:34

✓ **Yosuke Yamazaki**

Assinou em 12 dez 2022 às 06:41:06

✓ **GABRIEL BRANDO SOARES**

CPF: 132.567.897-06

Assinou em 08 dez 2022 às 09:22:51

✓ **ANDRE WIERMANN**

CPF: 669.385.037-53

Assinou em 07 dez 2022 às 14:27:22

✓ **ANDRES REINALDO RODRIGUES PAPA**

CPF: 045.347.027-01

Assinou em 07 dez 2022 às 15:38:44

Brando Soares, Gabriel

Understanding the day-to-day variability of the equatorial electrojet/Gabriel Brando Soares. – Rio de Janeiro: ON, 2023.

iii, 115 p.: il.; 29, 7cm.

Orientador(a): Katia Pinheiro

Co-orientadores: Yosuke Yamazaki

Jürgen Matzka

Tese (doutorado) – ON/Programa de Pós-graduação em Geofísica, 2023.

Bibliography: p. 100 – 115.

1. Geomagnetism. 2. Equatorial Electrojet. 3. Inverse Problems. I. Yamazaki, Yosuke *et al.* II. Observatório Nacional, Programa de Pós-graduação em Geofísica. III. Título.

Dedicatória
Aos meus pais, Lícia e Flávio

ACKNOWLEDGEMENTS

Fortunately, during the development of this thesis, I was supported by fantastic people and institutions to which I will be always indebted. Here I owe express my deepest gratitude.

It was a pleasure to be supervised by three great researchers.

I thank my supervisor, Dr. Katia Pinheiro. Thanks for the nearly 10 years of partnership and for giving me opportunities to grow and to learn. I wish all young student could be received with your warm and friendly welcome, just as you did with me. Also, thanks for the dog.

I thank my supervisor Dr. Jürgen Matzka. I will be always grateful for the countless opportunities and new experiences that you kindly provided to me. Thanks for the exciting years working with you. Your enthusiasm with science and with providing high-quality data will always be a reference for me. I learned a lot from you. Thanks for all.

I thank my supervisor Dr. Yosuke Yamazaki. It was a pleasure working with you and an honour to learn from such a brilliant researcher. This work would not be possible without your supervision and suggestions. Thanks for your patience during these years. This journey would have been much more complicated without your careful explanations.

A special thanks goes to Dr. Achim Morschhauser, who taught me many important concepts for developing my research. Thanks for all the kindness and for the help in Germany.

Dr. Patrick Alken is here also acknowledged for his great contribution with the thesis methodology and with the satellite data sets used in this work.

I would like to thank the examiners that kindly accepted to evaluate this work, namely Dr. Maria Alexandra Pais, Dr. Livia Ribeiro Alves, Dr. André Wiermann and Dr. Andrés Papa.

I thank the institutions that allowed me to develop this thesis, namely Observatório Nacional and GFZ-Potsdam. I am grateful to all professors, technicians and staff from Observatório Nacional. It was a pleasure to work in a nearly 200 hundred years institution with a rich history and data archives that are a true treasure. Special thanks to Vassouras and Tatuoca observatories teams. I am also grateful to all

professors, technicians and staff from GFZ-Potsdam, where I developed a significant part of this thesis. I sincerely thank the staff in Niemegk and Potsdam which helped me in several ways.

I thank CAPES for supporting my studies by a PhD research grant.

I thank INTERMAGNET, MAGDAS, LISN, WDC-Mumbai and WAMNET magnetometer networks for providing the data used in this thesis.

I thank my family, my parents and my sister which were and are always around, providing anything that I need and helping me in the difficult moments. I am sure that I naturally learned the basis of how to be a scientist at home. Anything that you do is in an organized, thorough and analytical manner. Thanks for all!

Last but not least, I thank my dear fiancée Laís. Thanks for supporting me during these years, for encouraging me during the challenging times and for your companionship. Thanks for your tremendous patience with all the travels, reports, presentations, articles and weekends of work. You are awesome.

Resumo da Tese apresentada ao Programa de Pós-Graduação em Geofísica do Observatório Nacional como parte dos requisitos necessários para a obtenção do título de Doutor em Geofísica.

UNDERSTANDING THE DAY-TO-DAY VARIABILITY OF THE EQUATORIAL ELECTROJET

Gabriel Brando Soares

Fevereiro/2023

Esta tese está dividida em três partes principais: Partes I, II e III.

A Parte I consiste em uma breve revisão sobre conceitos essenciais associados ao campo magnético e atmosfera terrestres, visando um melhor entendimento das Partes II e III subsequentes.

A Parte II apresenta um estudo sobre a corrente ionosférica do eletrojato equatorial (EEJ). A intensidade do EEJ apresenta variações temporais e espaciais que não são completamente compreendidas ou modeladas de maneira precisa. Sabe-se que marés solares atmosféricas estão entre os principais mecanismos geradores da variação do EEJ. Visando compreender melhor quais marés solares atmosféricas são importantes na variação do EEJ, nós desenvolvemos um novo modelo do EEJ, denominado PCEEJ, baseado na análise de componentes principais (PCA) de dados geomagnéticos. Além de apresentar um melhor ajuste aos dados observados quando comparado ao modelo EEJM-2, o modelo PCEEJ nos permitiu derivar a série temporal das amplitudes de marés solares, baseado no ajuste da equação das marés. Os resultados indicam que é possível obter um espectro representativo do EEJ associado a marés solares para um período de tempo relativamente curto de 70 dias.

A Parte III está relacionada à recuperação e processamento dos valores médios horários da componente horizontal do campo geomagnético (H) medida no observatório geomagnético de Tatuoca (TTB), de 1957 a 2019. Além de disponibilizar um conjunto de dados de cerca de 60 anos da região da Anomalia Magnética do Atlântico Sul, este trabalho permitiu a investigação de mudanças de longo período na variação diurna registrada em TTB em função da influência da variação secular, atividade solar, estação do ano e fase lunar. Diante da intensa variação secular na região e da longa série temporal, uma transição incomum entre os padrões de variação diurna de baixa latitude e equatorial foi registrada nos dados de TTB. Tal transição impactou

em diversas feições da variação diurna observada e foi comparada às simulações realizadas com o modelo TIEGCM (Thermosphere-Ionosphere-Electrodynamics General Circulation Model). Os resultados confirmaram que a dinâmica do campo geomagnético principal foi a principal causa das mudanças de longo período observadas no campo geomagnético externo.

Abstract of the Thesis presented to the National Observatory's Graduate Program in Geophysics as a partial fulfillment of the requirements for the degree of Doctor in Geophysics.

UNDERSTANDING THE DAY-TO-DAY VARIABILITY OF THE EQUATORIAL ELECTROJET

Gabriel Brando Soares

February/2023

This thesis is divided in three main parts: Parts I, II and III.

Part I is a brief review about essential concepts related to Earth's magnetic field and atmosphere, aiming a better understanding of the subsequent Parts II and III.

Part II presents a study about the equatorial electrojet (EEJ) ionospheric current. The intensity of the EEJ shows temporal and spatial variability that is not yet fully understood nor accurately modeled. It is known that atmospheric solar tides are among the main drivers of the EEJ variability. Aiming to better understand which atmospheric solar tides are important in the EEJ variability, we developed a new model of the EEJ, namely PCEEJ, which is based on the principal component analysis (PCA) of geomagnetic data. Apart from showing better match to the observed data when compared to the EEJM-2 model, the PCEEJ model allowed us to derive the time series of solar tides amplitudes based on tidal equation fitting. The results indicate that it is possible to obtain a meaningful EEJ spectrum related to solar tides for a relatively short time interval of 70 days.

Part III is related to the recovery and processing of the hourly mean values of the geomagnetic field horizontal (H) component measured at the geomagnetic observatory Tatuoca (TTB), from 1957 until 2019. Besides delivering a 60-year long processed data set from the South Atlantic Anomaly region, the work allowed the investigation of long-term changes in the daily variation recorded in TTB due to the influence of secular variation, solar activity, season and lunar phase. Due to the pronounced secular variation in the region and to the long time series, an unusual transition from typical low-latitude solar quiet daily variation to EEJ higher-magnitude daily variation was recorded at TTB data set. This transition impacted several features of the observed daily variation and was compared to simulations performed with the Thermosphere-Ionosphere-Electrodynamics General Circulation

Model (TIEGCM). The results confirmed that the geomagnetic main field dynamics was the main cause of the observed external field long-term changes.

CONTENTS

LIST OF FIGURES	xiv
LIST OF TABLES	xvii
LIST OF ABBREVIATIONS	xviii

I THE ROLE OF EARTH'S ATMOSPHERE IN GEOMAGNETIC VARIATIONS 1

1 Earth's Magnetic Field	2
1.1 FIELD REPRESENTATION AND MEASUREMENTS	3
2 Earth's Atmosphere	7
2.1 THE ATMOSPHERE AND ITS STRUCTURE	7
2.2 IONOSPHERE	8
3 Ionosphere Electrodynamics	10
3.1 THE IONOSPHERIC DYNAMO	10
3.2 CONDUCTIVITY	11
3.3 THERMOSPHERIC WINDS	15
3.4 IONOSPHERIC ELECTRIC CURRENTS	18

II USING PRINCIPAL COMPONENT ANALYSIS TO MODEL THE EQUATORIAL ELECTROJET AND DERIVE ITS TIDAL COMPOSITION 21

4 Summary and Introduction	22
4.1 SUMMARY	22
4.2 THE GEOMAGNETIC DIURNAL VARIATION AND THE EQUATORIAL ELECTROJET	22
4.3 OBJECTIVES AND SCIENTIFIC CONTRIBUTION	25

5	Data and Model	27
5.1	GROUND-BASED MAGNETIC DATA	27
5.2	SATELLITE MAGNETIC DATA	28
5.3	SABER TEMPERATURE SATELLITE DATA	32
5.4	EEJM-2 CLIMATOLOGICAL MODEL	33
6	EEJ Modeling and its Inversion for Solar Tides	34
6.1	COMBINING GROUND AND SATELLITE EEJ DATA	34
6.2	PRINCIPAL COMPONENT ANALYSIS (PCA)	35
6.2.1	PRINCIPAL COMPONENTS FIT	41
6.3	INVERTING EEJ FOR TIDES AMPLITUDES	42
6.4	EEJM-2 MODEL SETTINGS	43
6.5	COMPARISON WITH SABER TEMPERATURE DATA	43
6.6	WORKFLOW FOR RETRIEVING IMPORTANT TIDAL MODES	44
7	Results and Discussion	46
7.1	OBSERVED EEJ, PCEEJ, EEJM-2 AND RECONSTRUCTION WITH TIDES	46
7.2	PCEEJ vs EEJM-2	51
7.2.1	MATCH TO OBSERVED DATA	51
7.2.2	AVERAGE TIDAL COMPOSITION PER YEAR	53
7.3	MIGRATING TIDES TIME SERIES	55
7.4	NON-MIGRATING TIDES TIME SERIES	57
8	Conclusions	63
 III EVOLUTION OF THE GEOMAGNETIC DAILY VARIATION AT TATUOCA, BRAZIL, FROM 1957 TO 2019		64
9	Summary and Introduction	65
9.1	SUMMARY	65
9.2	EVOLUTION OF THE GEOMAGNETIC DAILY VARIATION AT TATUOCA, BRAZIL	66
10	Data and Model	69
10.1	TATUOCA GEOMAGNETIC OBSERVATORY	69
10.2	ADDITIONAL GROUND-BASED DATA	72
10.3	SATELLITE DATA	72
10.4	GEOPHYSICAL INDICES	72

10.5 TIEGCM MODEL SETUP	73
11 Methods for Data Analysis	74
11.1 GEOMAGNETIC ACTIVITY	74
11.2 SOLAR FLUX DEPENDENCE	75
11.3 TRANSITION FROM SQ TO EEJ	75
11.4 SEASONAL DEPENDENCE	75
11.5 DAY-TO-DAY VARIABILITY	76
11.6 LUNAR VARIATION	76
11.7 COUNTER-ELECTROJET OCCURRENCE	77
11.8 TIEGCM SIMULATION	77
12 Results and Discussion	78
12.1 SOLAR FLUX DEPENDENCE	78
12.2 TRANSITION FROM SQ TO EEJ	78
12.3 SEASONAL DEPENDENCE	83
12.4 DAY-TO-DAY VARIABILITY	84
12.5 LUNAR VARIATION	87
12.6 COUNTER-ELECTROJET OCCURRENCE	88
12.7 TIEGCM SIMULATION	92
13 Conclusions	94
13.1 EVOLUTION OF THE GEOMAGNETIC DAILY VARIATION AT TATUOCA, BRAZIL	94
IV PUBLICATIONS	96
14 Publications	97
14.1 RELATED TO THIS THESIS	97
14.2 ADDITIONAL PUBLICATIONS	97
V BIBLIOGRAPHY	99
Bibliography	100

LIST OF FIGURES

PART I

1.1	Geomagnetic field components.	3
1.2	Maps of declination, inclination and total field obtained with the IGRF-13 for epoch 2020.	6
2.1	Typical profiles of neutral atmospheric temperature and ionospheric plasma density with the various layers designated.	8
3.1	Height profiles of the parallel, Pedersen and Hall conductivities calculated for geographic coordinates 35° N, 135° E, under noon-time, March equinox, low solar activity conditions.	15
3.2	Thermospheric winds distribution at 110 km height obtained from TIE-GCM model simulations for geomagnetically quiet equinox conditions.	17
3.3	Diagram showing a view-from-above of the zonal electric field component, the equatorial geomagnetic field and the charge densities at the terminators.	18
3.4	Enhancement of the eastward ionospheric current due to the Cowling effect.	19

PART II

5.1	Geographical and temporal distribution of ground-based magnetometers and satellite data.	30
5.2	Satellite altitude variation with time for Ørsted, SAC-C, CHAMP and Swarm missions.	32
6.1	Relation between ground-based and satellite EEJ data for eight considered longitudinal sectors.	36
6.2	Sketch of the initial longitude versus local time data grid to be applied in the PCA.	37
6.3	Cumulative variance explained by the principal components.	39
6.4	Principal components 1 to 10, derived from EEJ satellite data.	40

6.5	Longitude versus local time grid with the number of samples within each bin for different epochs of 2017.	42
6.6	Flowchart with the proposed workflow to retrieve the tidal modes that are important in the EEJ day-to-day variability.	45
7.1	Observed EEJ, PCEEJ, EEJM-2 and EEJ reconstruction with tides data displays for 2017.	48
7.2	Observed EEJ, PCEEJ, EEJM-2 and EEJ reconstruction with tides data displays for 2018.	49
7.3	Observed EEJ, PCEEJ, EEJM-2 and EEJ reconstruction with tides data displays for 2016.	50
7.4	Histograms of residuals between observed data and EEJM-2 model and between observed data and PCEEJ model.	52
7.5	Time series of residuals metrics and data grid bins coverage.	53
7.6	Correlation coefficient between observed data and PCEEJ model and between observed data and EEJM-2 model.	54
7.7	Average yearly EEJ tidal spectrum given by $\log(\text{mA/m})^2$ for each combination of n and s, during the years of 2015, 2016, 2017 and 2018.	55
7.8	Time series of DW1 tide amplitude obtained from EEJ data during the Swarm period.	56
7.9	Time series of SW2 tide amplitude obtained from EEJ data during the Swarm period.	56
7.10	Time series of DE3 tide amplitude obtained from EEJ data and from SABER temperature data during the Swarm period.	58
7.11	Time series of DE2 tide amplitude obtained from EEJ data and from SABER temperature data during the Swarm period.	58
7.12	Time series of DE4 tide amplitude obtained from EEJ data and from SABER temperature data during the Swarm period.	59
7.13	Time series of SW4 tide amplitude obtained from EEJ data and from SABER temperature data during the Swarm period.	60
7.14	Time series of TW1 tide amplitude obtained from EEJ data and from SABER temperature data during the Swarm period.	61
7.15	Time series of DE3 tide amplitude obtained from EEJ data and from SABER temperature data during the CSØ period.	61
7.16	Time series of SW4 tide amplitude obtained from EEJ data and from SABER temperature data during the CSØ period.	62

PART III

10.1	Tatuoca geomagnetic observatory: long time series and fast magnetic equator movement.	70
------	---	----

12.1	Monthly averages of TTB H_A range versus $\sqrt{F10.7}$	79
12.2	Average yearly values of H_N range at TTB, from 1957 to 2019.	80
12.3	Quasi-dipole (QD) latitudinal profile of satellite-derived (CHAMP and Swarm) height-integrated current intensity.	82
12.4	Seasonal variation of the normalized H_N range at TTB.	83
12.5	Long-term changes on TTB and HUA H component day-to-day variability.	84
12.6	Histogram of day-to-day variability values observed at TTB and HUA, from 1957 to 2019.	85
12.7	Predicted average amplitude of the lunar variation L in TTB H-component, as a function of local time and lunar age.	87
12.8	Predicted average amplitude of the lunar variation L in HUA H-component, as a function of local time and lunar age.	88
12.9	Annual occurrence rates of morning and afternoon counter electrojet events at TTB and PAB derived from the TTB-KOU and TTB-PAB pairs during 1996-2019 and 1964-1965, respectively.	89
12.10	QD latitudinal profile of westward current occurrence rate at the Brazilian sector, derived from CHAMP and Swarm satellite data.	91
12.11	TIEGCM simulation results for TTB and HUA coordinates and comparison with observed data.	93

LIST OF TABLES

PART II

- 5.1 Summary with the equatorial and low-latitude ground stations used to derive the EEJ data. 29
- 5.2 Summary with the linear transformation coefficients c_1 and c_2 for each satellite. 31

PART III

- 12.1 Slope and intercept of the linear fits between H_A range and $\sqrt{F10.7}$ for 15 subsets used to normalize H_A data. 79
- 12.2 Summary of statistical measures of each distribution of TTB and HUA day-to-day variability. 86

LIST OF ABBREVIATIONS

AAE	Addis Ababa Magnetic Observatory
ABG	Alibag Magnetic Observatory
ACEJ	Afternoon Counter Electrojet
BCL	Bac Lieu Magnetic Station
CEJ	Equatorial Counter Electrojet
CHAMP	Challenging Minisatellite Payload Satellite Mission
CMIT	Coupled Magnetosphere-Ionosphere-Thermosphere Model
CSØ	Operation period of CHAMP, SAC-C and Ørsted satellites
D	Geomagnetic Declination Angle
DAV	Davao Magnetic Station
DE2	...	Diurnal Eastward-Propagating Non-Migrating Tide (Zonal Wavenumber 2)
DE3	...	Diurnal Eastward-Propagating Non-Migrating Tide (Zonal Wavenumber 3)
DE4	...	Diurnal Eastward-Propagating Non-Migrating Tide (Zonal Wavenumber 4)
DW1	Diurnal Westward-Propagating Migrating Tide (Zonal Wavenumber 1)
DoY	Day of Year
EEJ	Equatorial Electrojet
EEJM-2	Equatorial Electrojet Model Version 2.0
EUV	Extreme Ultraviolet Radiation
EUVAC	Extreme Ultraviolet Flux Model for Aeronomic Calculation
F	Geomagnetic Total Field Component
GFZ	German Research Centre for Geosciences
GUA	Guam Magnetic Observatory
H	Geomagnetic Horizontal Component

H_A	Geomagnetic Horizontal Component Daily Ranges
H_N	Normalized Geomagnetic Horizontal Component Daily Ranges
HUA	Huancayo Magnetic Observatory
I	Geomagnetic Inclination Angle
ICD	Height Integrated Current Density (satellite electrojet signal)
IGRF	International Geomagnetic Reference Field
INTERMAGNET	International Association of Geomagnetism and Aeronomy
IDD	International Geomagnetically Disturbed Days
IQD	International Geomagnetically Quiet Days
KOU	Kourou Magnetic Observatory
KTB	Kototabang Magnetic Station
LT	Local Time
MBO	Mbour Magnetic Observatory
MCEJ	Morning Counter Electrojet
MUT	Muntinlupa Magnetic Station
ON	Observatório Nacional
PAB	Paramaribo Magnetic Observatory
PC	Principal Component
PCs	Principal Components
PCA	Principal Component Analysis
PCEEJ	Principal Component Analysis Equatorial Electrojet Model
PIU	Piura Magnetic Station
PHU	Phuthuy Magnetic Station
PKT	Phuket Magnetic Station
QD	Quasi-Dipole
QW4	Quarterdiurnal Westward-Propagating Migrating Tide (Zonal Wavenumber 4)
SABER	Sounding of the Atmosphere using Broadband Emission Radiometry
SAM	Samogossoni Magnetic Station
SC	Solar Cycle
sfu	Solar flux unit

SPW	Stationary Planetary Wave
SPW2	Stationary Planetary Wave (Zonal Wavenumber 2)
Sq	Solar-quiet Daily Variation
SW2	..	Semidiurnal Westward-Propagating Migrating Tide (Zonal Wavenumber 2)
SW4		Semidiurnal Westward-Propagating Non-Migrating Tide (Zonal Wavenumber 4)
TAM	Tamanrasset Magnetic Observatory
TIMED	Thermosphere Ionosphere Mesosphere Energetics Dynamics Satellite
TIEGCM	..	Thermosphere-Ionosphere Electrodynamics General Circulation Model
TIR	Tirunelveli Magnetic Observatory
TND	Tondano Magnetic Observatory
TRD	Trivandrum Magnetic Observatory
TTB	Tatuoca Magnetic Observatory
TW1	Terdiurnal Westward-Propagating Migrating Tide (Zonal Wavenumber 1)
TW3	Terdiurnal Westward-Propagating Migrating Tide (Zonal Wavenumber 3)
UT	Universal Time
VSS	Vassouras Magnetic Observatory
X	Geomagnetic Component in the Geographic North Direction
WDC	World Data Centre
Y	Geomagnetic Component in the Geographic East Direction
YAP	Yap Island Magnetic Station
Z	Geomagnetic Vertical Component
ΔH	Ground-Based Equatorial Electrojet Signal

Part I

THE ROLE OF EARTH'S ATMOSPHERE IN GEOMAGNETIC VARIATIONS

Part I presents the theoretical background related to the geomagnetic field and its daily variation.

CHAPTER 1

EARTH'S MAGNETIC FIELD

The observed Earth's magnetic field is a result of the combination of magnetic fields generated by different sources (Olsen et al., 2010). Each geomagnetic source varies differently in space and time, resulting in a complex superposition of magnetic fields with different amplitudes and frequencies of oscillation (Campbell, 1997; Chapman and Bartels, 1940). These fields are then classified according to their internal or external origin.

The main field is the most important parcel of the geomagnetic field, responsible for about 90% of the total observed field. It is classified as an internal field due to its generation by convection mechanisms down at the Earth's metallic liquid outer core in a process known as the geodynamo (Jones, 2007). It can reach amplitudes ranging between 20000 and 70000 nanotesla (nT) and it varies slowly in time, leading to changes that are noticeable only after years or decades of measurements. This slow pace of the main field variation is directly related to the outer core dynamics and is known as the secular variation (Wardinski, 2007). Another part of the internal field is the lithospheric or crustal field, which is the magnetic field related to minerals with magnetic properties at the Earth's lithosphere (Thébault et al., 2010). The lithospheric field has amplitudes of hundreds of nT and its temporal changes occur in a geological time-scale. In addition, electromagnetically induced currents flowing in the conducting planetary interior due to the time-varying external fields give rise to the so-called induced field, which is also classified as an internal contribution (Saur et al., 2010).

Apart from the aforementioned internal fields, there are numerous external field sources caused by processes taking place at Earth's magnetosphere and ionosphere¹. Variations in the solar wind due to events like solar coronal mass ejections can increase the energy transfer rate from solar wind into Earth's magnetosphere. This process amplifies magnetosphere currents, which consequently lead to important magnetic disturbances at Earth, such as geomagnetic storms. Geomagnetic storms can reach amplitudes of around 500 nT under extreme events and usually last for a

few days (Gonzalez et al., 1994). The frequency of occurrence of geomagnetic storms depends on the solar activity. The Sun, by its turn, presents cycles of activity, such as its 11-year solar cycle.

Besides the phenomena taking place in the magnetosphere, a number of electric current systems, caused by different generation mechanisms, flow through the Earth’s ionized atmosphere (ionosphere). These ionospheric currents induce magnetic fields and drive, for example, the so-called geomagnetic daily variation, which has a periodicity of 24 hours and amplitudes up to 250 nT (Winch, 2007). The amplitude of such variations are subjected to changes related to solar activity, season, gravity (lunar tides) and main field intensity.

1.1 FIELD REPRESENTATION AND MEASUREMENTS

The geomagnetic field is a vectorial field and can be described in Cartesian coordinates X or N (horizontal, pointing northwards), Y or E (horizontal, pointing eastwards) and Z (vertical), or in spherical polar coordinates by F (total field vector), D (declination angle) and I (inclination angle) elements, as shown in Figure 1.1.

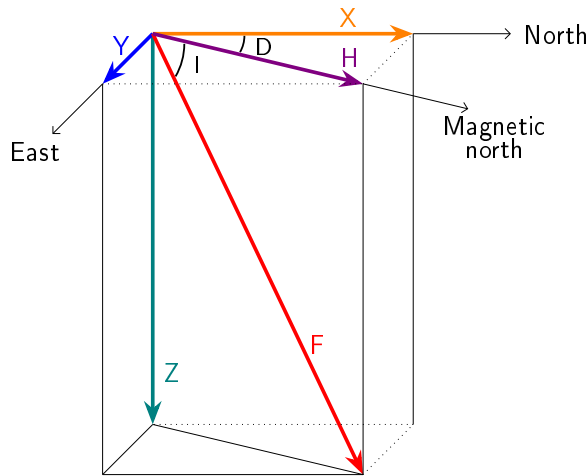


Figure 1.1: Geomagnetic field components. X and Y are the horizontal components pointing to the geographic north and east directions, respectively. H is the horizontal component pointing to the magnetic north direction. D is the magnetic declination angle, which is the angle between magnetic and geographic north directions. I is the magnetic inclination angle, which gives the total field inclination in relation to the horizontal plane. Z is the vertical component and F is the total field vector. From Soares (2018), which is based on St-Louis (2011).

¹The ionosphere the ionized portion of Earth’s atmosphere, ranging between 60 km and 1000 km of height. The magnetosphere extends to about 10 Earth radii at the day side (100 Earth radii for the night side) and it is the region around the Earth where its magnetic field is predominant.

Each geomagnetic field source mentioned above affect differently the components shown in Figure 1.1, depending on the relative position between the source and place of observation. Geomagnetic measurements are continuously performed by magnetometers placed either at ground surface or satellite altitudes. Vector field magnetometers and absolute scalar magnetometer are used in both ground and satellite measurements for a complete description of the field. These instruments differ in their construction principles: the vector magnetometers are typically a triaxial fluxgate magnetometer, while the scalar magnetometer is typically a proton, Overhauser or optically pumped, cesium or potassium magnetometer measuring the modulus of the total field (F).

Based on ground and satellite observations, the geomagnetic field sources can be investigated and even modelled in local or global scales. For instance, data from geomagnetic observatories and satellites are used to build the International Geomagnetic Reference Field (IGRF) model in order to represent the geomagnetic main field in a global perspective by means of spherical harmonic forward modelling (Alken et al., 2021). For example, Figure 1.2 shows contour maps with the global distribution of the declination (D), inclination (I) and total field (F) geomagnetic components for 2020, obtained with the latest IGRF version (13th generation, Alken et al., 2021). The maps depict another important characteristic of the geomagnetic field that is its spatial variation, which in the case of the main field reveals prominent features such as the South Atlantic Anomaly (region with the lowest values in the bottom map).

Other geomagnetic field sources, either of internal or external nature, can also be modelled based on magnetic observations distributed across the globe. IGRF and other models are routinely used by the scientific community to study Earth's core field, space weather, electromagnetic induction and local magnetic anomalies in the lithosphere. Such models are also widely used in satellite attitude determination, control systems and other applications requiring orientation information such as oil and gas industry drilling activities. Thus, a better understanding and modelling of the geomagnetic field benefits, at the same time, scientific investigations from any area related to Earth's magnetic field and industry applications.

Therefore, in geomagnetism, it is very important to treat the available measurements accordingly in order to isolate the signal of interest. Those who are interested in studying the geomagnetic main field need to properly select data, avoiding external field influence. In the same manner, those interested in studying geomagnetic storms need to process specific field components aiming to avoid internal field and other external field signals. In this thesis, the geomagnetic field caused by ionospheric currents are the main topic under debate. Thus, the next chapters of this part present more details on the Earth's atmosphere and its related geomagnetic

daily variation.

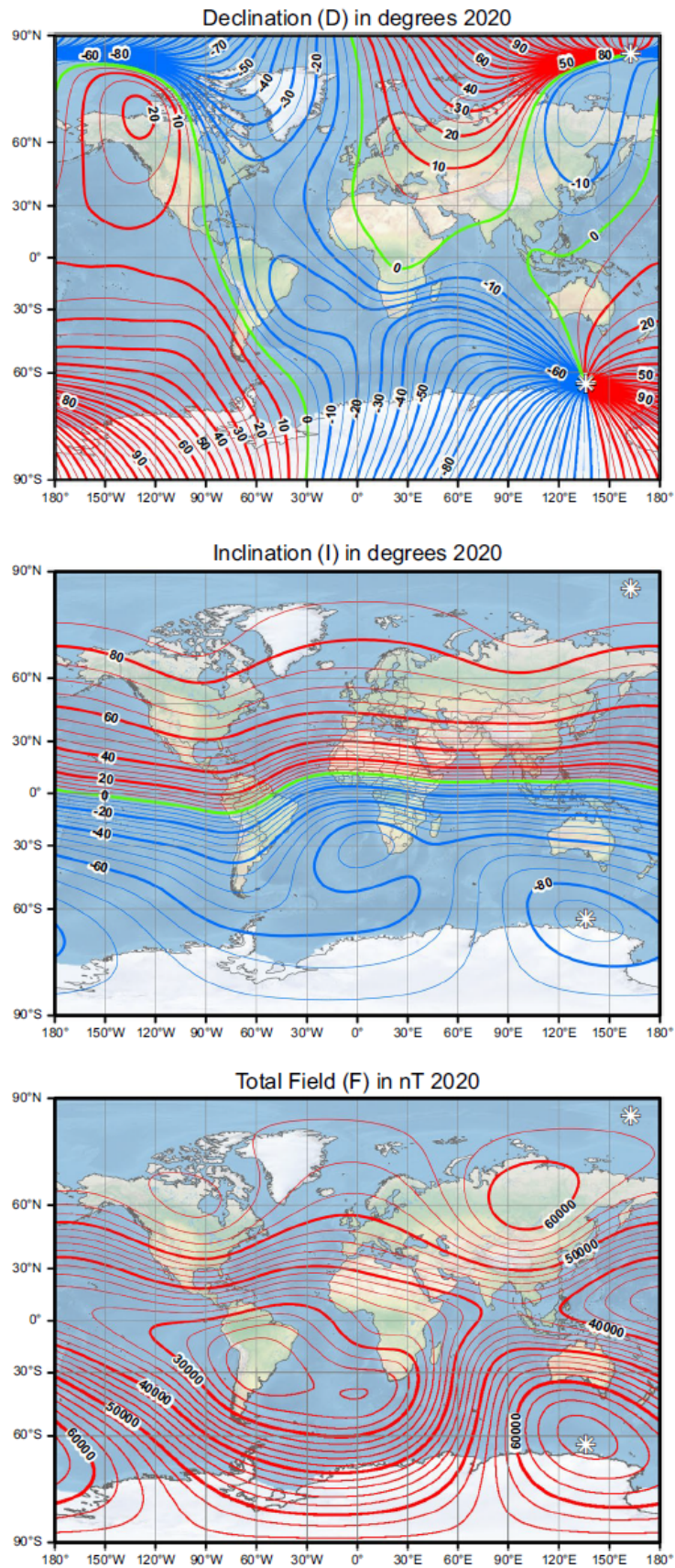


Figure 1.2: Maps of declination (top), inclination (middle) and total field (bottom) obtained with the IGRF-13 for epoch 2020. The zero contour is shown in green, positive contours in red, and negative contours in blue. White asterisks indicate locations of the magnetic dip poles. From [Alken et al. \(2021\)](#).

CHAPTER 2

EARTH'S ATMOSPHERE

2.1 THE ATMOSPHERE AND ITS STRUCTURE

The Earth's atmosphere is the envelope of gases that surrounds the planet Earth due to gravitational attraction. Its constituents can be classified in two different portions, the neutral atmosphere and the ionosphere. The ionosphere is the part of the Earth's upper atmosphere constituted by partially ionized plasma. The plasma constituent is produced by the ionization of neutrals due to their photodissociation caused by energetic short-wavelength (<150 nm) solar radiation ([Kamide and Chian, 2007](#)).

Since the nature of gases and forces acting on them depends on height, the Earth's atmosphere is subdivided into different regions. Both neutral and ionized gases are considered, to a first order, horizontally stratified. The neutral atmosphere structure is typically represented by its temperature profile, while the ionosphere structure is better represented by its plasma density profile as shown in Figure 2.1 ([Kelley, 2009](#)).

The typical temperature profile shown in Figure 2.1 shows that the atmospheric temperature initially decreases with altitude from the surface temperature in the so-called troposphere. It is characterized by lapse rate of temperature of about 7 K per km, decreasing up to the tropopause region. The region known as "upper atmosphere" starts with the stratosphere, which is found above the troposphere (8 to 16 km, depending on the latitude). In the stratosphere, the temperature trend changes and it starts to increase with altitude. This increase in temperature throughout the stratosphere is primarily due to the absorption of part of the ultraviolet portion of the solar radiation by ozone molecules. This effect maximizes at around 50 km (stratopause), where the temperature trend reverses once again. In the mesosphere, the temperature keeps decreasing until a minimum near 85 km (mesopause). The mesosphere sharp temperature decrease is explained by radiative cooling. Above the mesopause, where the thermosphere takes place, the temperature increases dramati-

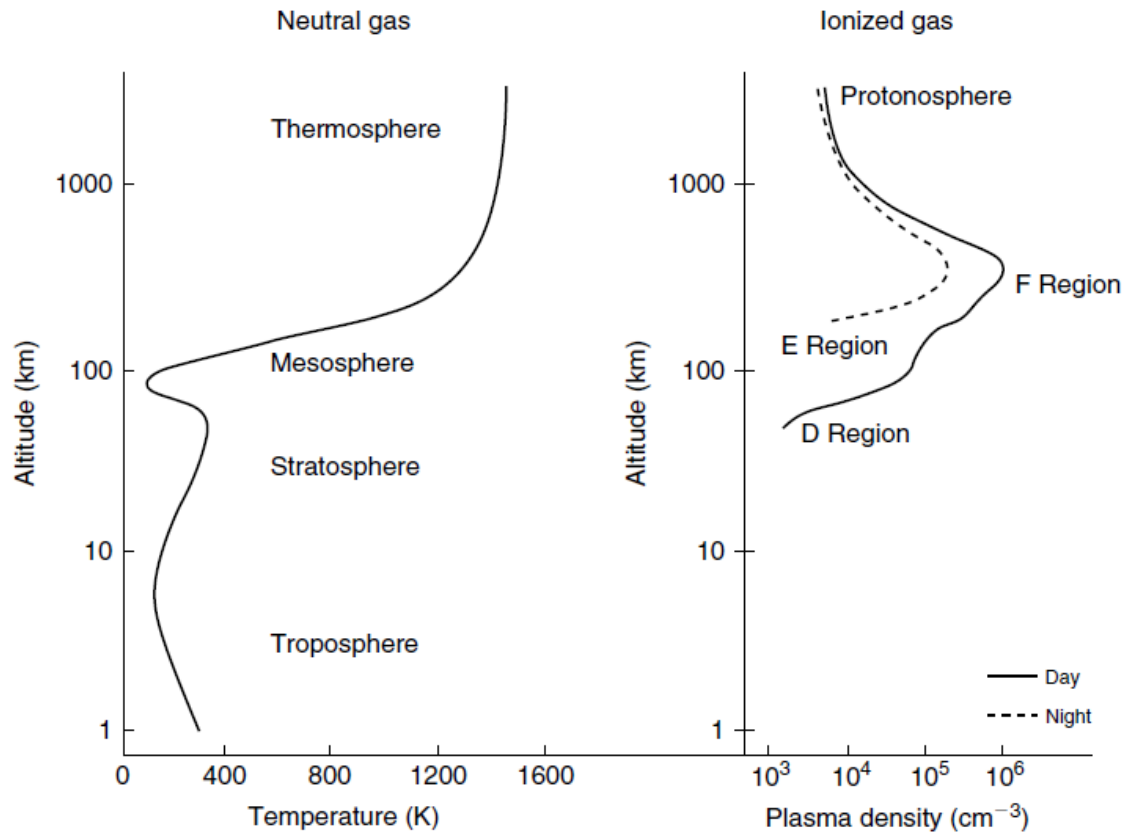


Figure 2.1: Typical profiles of neutral atmospheric temperature and ionospheric plasma density with the various layers designated. From [Kelley \(2009\)](#).

ically due to absorption of even higher energy solar photons, reaching values greater than 1000 K at heights above 400 km ([Dieminger et al., 1996](#)).

2.2 IONOSPHERE

The absorption of UV and EUV radiation from the sun in the thermosphere explains not only the temperature increase but also the production of plasma in the sunlit hemisphere at that thermospheric heights. This occurs because the solar photons have enough energy to ionize the neutral atmosphere, producing ions and electrons during such ionization process. This process explains the different plasma density profiles shown for day and night times in the right-hand side of [Figure 2.1](#). During daytime the solar photons are incident on the neutral atmosphere, leading to the process of photoionization ([Kivelson and Russell, 1995](#)). The combination of decreasing solar flux with decreasing height, increasing neutral density, and diffusion explains the plasma density structure seen in [Figure 2.1](#). This portion of ionized gas found in the upper atmosphere is considered as the Earth's ionosphere.

The ionosphere coexists with the upper part of the neutral atmosphere and receives considerable energy and momentum from the lower atmosphere as well as from

the magnetosphere. The energy and momentum fluxes are carried by particles, electromagnetic fields, and atmospheric waves. Like the neutral atmosphere, the ionosphere can also be divided in different regions (as observed in Figure 2.1). The F-region is found above 140 km, where the main source of ionization is the interaction between EUV radiation (10-100 nm) with atomic oxygen (O) and molecular nitrogen (N_2). It includes the heights with maximum plasma density in the ionosphere, namely the F peak, which consists mostly of atomic oxygen ions (O^+). The F-region is often sub-divided into F1 and F2 layers during daytime due to their different molecular ions distribution with height. Below the F-region, the E-region takes place (90-140 km) with ionization occurring mainly due to X-rays (1-10 nm) and UV (100-150 nm) radiation, leading to a predominance of NO^+ and O_2^+ molecular ions. The D-region is located between 90 and 60 km of altitude, with dominant source of ionization by photoionization of NO by Lyman- α (121.6 nm) solar radiation, and of O_2 by high energy cosmic rays (Kelley, 2009).

At all ionospheric regions, the recombination rate affects the plasma density as ions and electrons re-combine to form a neutral molecule or atom. For example, in the E-region, where NO^+ and O_2^+ molecular ions dominate, two fast reactions that can occur in favour of recombination are:



and



which are known as dissociative recombination, given that the molecule ion breaks apart. At higher altitudes, radiative recombination is also expected to occur ($O^+ + e^- \rightarrow O + \textit{photon}$), given that the emission of photon is required to conserve energy and momentum. However, the dissociative recombination has a much higher reaction rate, resulting in a much shorter lifetime for molecular ions than for atomic ions. Due to its smaller lifetime, molecular ions quickly reduce plasma concentration during night time, while O^+ plasma often survives during the night at higher altitudes.

CHAPTER 3

IONOSPHERE ELECTRODYNAMICS

3.1 THE IONOSPHERIC DYNAMO

Interactions between the ionospheric plasma and the much denser neutral gases in the upper atmosphere give rise to a wide number of electrodynamic phenomena. While the neutral atmosphere dynamics is dominated by hydrodynamic processes, the ionospheric plasma dynamics is dominated by electromagnetic processes. Although the mass of the plasma portion is much smaller than that of the neutral portion, the plasma can transfer significant momentum and energy to the neutrals through collisions, because the electric and magnetic forces experienced by the ions and electrons within the plasma are large (Richmond, 2011).

Electric fields and associated currents are created in response to the forces acting on the plasma. The energy to generate them comes basically from two different inputs: the kinetic energy of thermospheric winds and the kinetic and thermal energy of the magnetospheric plasma. The former is the main energy input during geomagnetically quiet periods, while the latter becomes important when the solar disturbances are enhanced. Gravity forces are also acting on the plasma, but they play a minor role on producing electrodynamic effects. The geomagnetic field, which is dominated by the main field generated in the Earth's molten outer core, strongly organizes the electric fields and currents distribution. The generation of the electric fields and associated currents by thermospheric winds motion is referred to as the ionospheric wind dynamo, or only ionospheric dynamo (Richmond, 2011).

Although the motion of the neutral atmosphere itself does not cause any electromagnetic field, electrodynamic effects arise from the collisions between neutral and plasma particles. In this work, by ionospheric dynamo, we refer to the dynamo process at E-region heights. The dynamo process at the F-region heights is out of our scope. In the E-region dynamo, the ion-neutral collision frequency is comparable with or larger than the gyro-frequency of ions while the electron-neutral

collision frequency is much smaller than the gyro-frequency of electrons. Thus, in principle, ions are coupled with neutral winds while electrons are frozen to magnetic field lines. The bulk motion of the plasma is driven by collisions between ions and neutrals (Yamazaki and Maute, 2017). This plasma flow generates an electric field by the product $-\mathbf{V} \times \mathbf{B}$, where \mathbf{V} is the plasma flow velocity and \mathbf{B} is the ambient geomagnetic field.

The electric field induced by the plasma flow is considered not curl-free, so that a magnetic field perturbation \mathbf{b} arises according to Faraday's law:

$$\nabla \times (-\mathbf{V} \times \mathbf{B}) = \frac{-\partial \mathbf{b}}{\partial t}. \quad (3.1)$$

The magnetic field perturbation relates to ionospheric currents \mathbf{J} through the Ampère's law:

$$\nabla \times \mathbf{b} = \mu_0 \mathbf{J}, \quad (3.2)$$

where μ_0 is the vacuum permeability.

Observations of \mathbf{J} provide important information about the processes driving it. Ionospheric currents, however, are difficult to be measured directly, and considerable information about them can be derived from other observations from secondary phenomena. For example, the geomagnetic perturbations associated with the currents can be measured both on the ground and in space.

3.2 CONDUCTIVITY

A direct measure of the ionosphere conductivity can not be obtained, but it can be calculated from a combination of observations and theoretical considerations. The ionosphere conductivity is an anisotropic tensor quantity $\hat{\sigma}$ that relates \mathbf{J} to the electric field \mathbf{E}' in a reference frame moving at the velocity \mathbf{U} of the local medium (Richmond, 2011). This relation is represented by the Ohm's law, given by:

$$\mathbf{J} = \hat{\sigma} \mathbf{E}', \quad (3.3)$$

where \mathbf{E}' is related to the electric field in the Earth-fixed frame, \mathbf{E} , by:

$$\mathbf{E}' = \mathbf{E} + \mathbf{U} \times \mathbf{B}. \quad (3.4)$$

Another manner to describe the current density \mathbf{J} is by:

$$\mathbf{J} = Nq(\mathbf{V}_i - \mathbf{V}_e), \quad (3.5)$$

which relates the ion and electron velocities \mathbf{V}_i and \mathbf{V}_e , number density N (i.e.,

number of charged species per unit volume), and charge q of the charged species. It tells us that any force that produces a relative motion between the ions and electrons will initially drive a current \mathbf{J} . A relation between the velocities \mathbf{V}_i and \mathbf{V}_e and electric field \mathbf{E}' can be found by understanding which forces are acting to move the charged particles and assuming that they are essentially in force balance (Heelis, 2004). The forces that are acting in this system are described below.

The force on charged particles caused by momentum-transfer due to collision with neutrals is given by:

$$\mathbf{F} = m\nu(\mathbf{V} - \mathbf{U}), \quad (3.6)$$

where m is the charged particle mass, ν is their collision frequency with neutrals, \mathbf{V} is the ion or electron velocity and \mathbf{U} is the neutral particle velocity. The mass of electrons is small enough to not significantly affect the motion of the ions or neutrals. Also, the collision frequency between ions and electrons is negligible given the much higher density of neutrals.

As we deal with plasma flowing in a magnetic field, the Lorentz force must be considered and is acting on the charged particles according to:

$$\mathbf{F} = q(\mathbf{V} \times \mathbf{B}). \quad (3.7)$$

In addition, there are forces due to gravity (\mathbf{g}):

$$\mathbf{F} = m\mathbf{g}, \quad (3.8)$$

due to electric fields (considered here to insure that the total current in the region is divergence free):

$$\mathbf{F} = q\mathbf{E}, \quad (3.9)$$

and due to plasma pressure gradients ∇p that are responsible for moving plasma from high pressure regions to low pressure regions:

$$\mathbf{F} = -\frac{1}{N\nabla p}, \quad (3.10)$$

or, equivalently, by considering the ideal gas law, we obtain:

$$\mathbf{F} = -\frac{1}{N\nabla(NkT)}, \quad (3.11)$$

where N is the number density, k is the Boltzmann's constant and T is the gas temperature. Since in this work we are interested in phenomena that evolve during long time scales of hours or more, we can ignore the acceleration of ions and electrons

and assume that all forces described above are in equilibrium. Based on this balance of forces, we can then write the equations of motion for ions:

$$-\frac{1}{N\nabla(NkT_i)} + m_i\mathbf{g} + q(\mathbf{E} + \mathbf{V}_i \times \mathbf{B}) - m_i\nu_{in}(\mathbf{V}_i - \mathbf{U}) = 0, \quad (3.12)$$

$$-\frac{1}{N\nabla(NkT_e)} + m_e\mathbf{g} + q(\mathbf{E} + \mathbf{V}_e \times \mathbf{B}) - m_e\nu_{en}(\mathbf{V}_e - \mathbf{U}) = 0, \quad (3.13)$$

where N , m , T , and \mathbf{V} are the ion/electron number density, mass density, temperature and mean velocity. \mathbf{g} is the acceleration due to gravity, k is Boltzmann's constant, q is the particle charge, \mathbf{E} is the electric field, \mathbf{B} is the geomagnetic field, ν_{in} is the collision frequency between neutrals and ions, ν_{en} is the collision frequency between neutrals and electrons and \mathbf{U} is the mean neutral thermospheric wind velocity. By solving these equations for the ion and electron velocities (details can be found in Heelis, 2004), it is possible to obtain an expression for the current density produced by relative motion between the ions and electrons:

$$\mathbf{J} = Nq(\mathbf{V}_i - \mathbf{V}_e) = \hat{\sigma} \frac{\mathbf{F}}{q} = \sigma_{\parallel} \frac{\mathbf{F}_{\parallel}}{q} + \sigma_P \frac{\mathbf{F}_{\perp}}{q} + \sigma_H \frac{\mathbf{F}_{\perp} \times \frac{\mathbf{B}}{|\mathbf{B}|}}{q} \quad (3.14)$$

where \mathbf{F} is the resultant force term independent of the ion/electron velocities. \mathbf{F}_{\parallel} and \mathbf{F}_{\perp} are the parallel and perpendicular (in relation to the geomagnetic field) force components, respectively. The current flows according to the Ohm's law, but the electric conductivity is anisotropic because of the effect of the geomagnetic field, and three conductivities are defined. σ_{\parallel} is the so-called parallel conductivity, which is the component in the direction of the geomagnetic field. σ_P and σ_H stand for Pedersen and Hall conductivities, respectively. The Pedersen conductivity peaks around 130 km and gives the component in the direction of the electric field for currents perpendicular to the geomagnetic field. The Hall conductivity peaks around 110 km and gives the component that is perpendicular to both electric and geomagnetic fields. In the ionosphere, the Hall conductivity is due to the drift motion of the electrons ($\mathbf{E} \times \mathbf{B}$ drift).

Thus, the final Ohm's Law relating \mathbf{J} to \mathbf{E}' by the conductivity tensor can be written in an expanded version as:

$$\mathbf{J} = \sigma_{\parallel} \mathbf{E}'_{\parallel} + \sigma_P \mathbf{E}'_{\perp} + \sigma_H \frac{\mathbf{B}}{|\mathbf{B}|} \times \mathbf{E}'_{\perp}, \quad (3.15)$$

where \mathbf{E}'_{\parallel} and \mathbf{E}'_{\perp} are the parallel and perpendicular (in relation to the geomagnetic field) electric field components, respectively:

Each conductivity can be calculated from observations (or models) of electron densities, as well as with modelled ion composition and collision frequencies. The

collision frequencies are mainly dependent on the neutral density, which is a function of height, location and time. The empirical model NRLMSISE00 (Picone et al., 2002) is one example of model used to estimate the densities. Some parameters like the ion-neutral collision cross sections are obtained from a combination of laboratory measurements and theoretical considerations (Richmond, 1995). Accordingly, there are formula established to derive ionospheric conductivities, as those from Equations 3.16, 3.17 and 3.18 that refer to σ_{\parallel} , σ_P and σ_H expressions, respectively.

$$\sigma_{\parallel} = \frac{e^2 n_e}{m_e \nu_e}, \quad (3.16)$$

$$\sigma_P = \sigma_{\parallel} \frac{(1 + \kappa) \nu_e^2}{(1 + \kappa)^2 \nu_e^2 + \Omega_e^2}, \quad (3.17)$$

$$\sigma_H = \sigma_{\parallel} \frac{\Omega_e \nu_e}{(1 + \kappa)^2 \nu_e^2 + \Omega_e^2}, \quad (3.18)$$

where $\Omega_e = (e | \mathbf{B} |)/(m_e)$; $\kappa = (\Omega_i \Omega_e)/(\nu_e \nu_{in})$; $\Omega_i = (e | \mathbf{B} |)/(m_i)$; $\nu_e = \nu_{en} + \nu_{ei}$; n_e is the electron density; ν_{en} is the electron-neutral collision frequency; ν_{ei} is the electron-ion collision frequency; ν_{in} is the ion-neutral collision frequency; Ω_e is the electron cyclotron frequency; Ω_i is the ion cyclotron frequency; e is the elementary charge; m_e is the electron mass. It is noted that the conductivity values depend inversely on the background geomagnetic field, leading to higher conductivities in the regions of weak geomagnetic field (e.g. South Atlantic Anomaly region), as implied from equations 3.17 and 3.18 above.

At all ionospheric altitudes, the parallel conductivity presents higher values when compared to Pedersen and Hall conductivities, as shown in Figure 3.1. The day-time Pedersen and Hall conductivities maximize in the E-region (Figure 3.1), where they are functions of solar zenith angle and solar activity level. The conductivity dependency on solar cycle variation (not shown on Figure 3.1) is explained by the variations of plasma and neutral densities with solar-cycle.

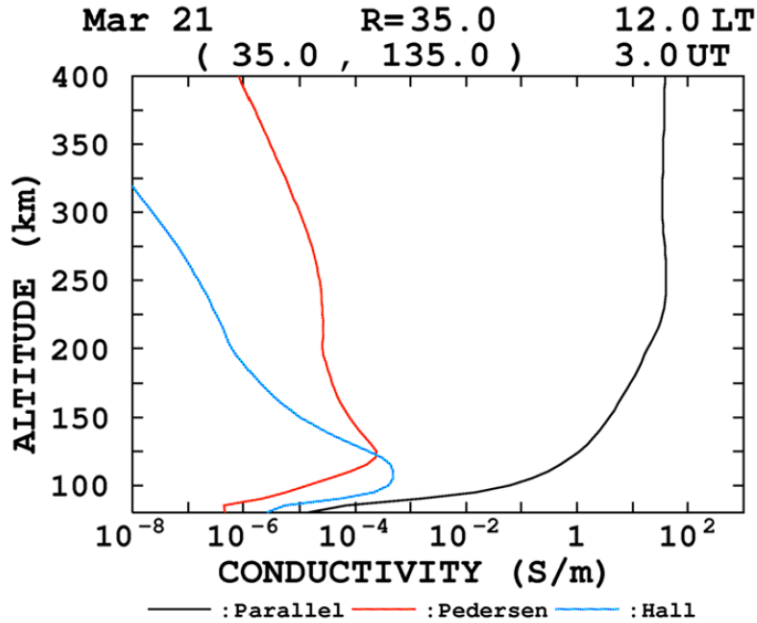


Figure 3.1: Height profiles of the parallel, Pedersen and Hall conductivities calculated for geographic coordinates 35° N, 135° E, under noon-time, March equinox, low solar activity conditions, based on the ionospheric conductivity model of the World Data Center for Geomagnetism, Kyoto. From [Yamazaki and Maute \(2017\)](#).

3.3 THERMOSPHERIC WINDS

The thermospheric winds that play an important role on driving the ionospheric dynamo are caused primarily by four different sources, which are described in the following four paragraphs.

The first main source is the daily absorption of solar ultraviolet radiation in the thermosphere that creates a diurnally varying temperature. Horizontal pressure gradients arise from the differential absorption between morning and afternoon sectors, which accelerate and decelerate winds as the Earth rotates. At low latitudes, the resulting winds due to these horizontal pressure gradients tend to be predominantly westward during the day and eastward at night sector. This effect is not uniform for all atmospheric altitudes. The acceleration due to the horizontal pressure gradients generally increases with altitude, because the increased scale height in the afternoon and the decreased scale height in the early morning leads to exponentially increasing differences with altitude of the constant-pressure surface heights between these times. Thus, the wind amplitude usually gets more pronounced with height throughout the thermosphere, and so wind dynamo tend to be more important toward higher atmospheric regions ([Richmond, 2011](#)).

Unlike the first source discussed above, the second major source of thermospheric

winds is related to oscillation propagating vertically in the atmosphere. These oscillations are caused by the upward propagation of atmospheric tides generated by diurnally varying heating in the troposphere and stratosphere (Hagan et al., 1999; Hagan and Forbes, 2002, 2003). The tides propagate vertically as global-scale waves due to different excitation mechanisms. Ultraviolet energy absorption by ozone found in the stratosphere and infrared solar radiation energy absorption by water vapour found in the troposphere produce tides that migrate westward around the Earth with the apparent motion of the Sun (Sun-synchronous). Another mechanism responsible for triggering tides vertical oscillations in the atmosphere is the latent heat release in clouds. As the development of clouds is strongly influenced by land-sea differences, the tidal development by latent heat release can generate tidal components that do not necessarily follow the apparent Sun movement (not Sun-synchronous), but rather can propagate both westward and eastward. The ability of tides to propagate into the thermosphere is influenced by their direction, speed, background medium of propagation and tidal dampening (Forbes et al., 2008). Some tidal components can propagate up to 120 km of altitude and are particularly effective in the context of the ionospheric dynamo, as they have substantial amplitudes through the regions where dayside Pedersen and Hall conductivities are large. The conditions of tides generation within their sources and of their propagation medium are subjected to changes due to season and to modulation by global-scale planetary waves with periods of multiple days. Lunar tides also play a role in the upper atmosphere thermospheric winds, but their excitation mechanism is gravitationally induced and their amplitudes are much weaker than those induced by the solar radiation.

The remaining major sources of thermospheric winds are related to geomagnetically disturbed periods, i.e., associated with geomagnetic storms occurrence. The third main source is the acceleration of winds by the rapidly drifting ions at high latitudes (Roble, 1992). This acceleration depends strongly on magnetospheric conditions and ion density, being pronounced during magnetic storms and where the ions are sufficiently decoupled from the neutral particles that they are able to drift.

The fourth and last main source of thermospheric winds is related to pressure gradients caused by high-latitude Joule heating. Like the previous source, the Joule heating is particularly important during magnetic storms. The increased high-latitude pressure drives equatorward winds above about 120 km, which afterwards tend to be turned westward at mid latitudes due to Coriolis effect. These westward winds build up positive and negative charges at the dusk and dawn terminators, respectively. This gives rise to polarization electric fields that are westward on the dayside and eastward on the nightside, opposed to the normal quiet-time fields. Thus, this process produces an "anti-Sq" current system on the dayside ionosphere

and is referred to as the disturbance dynamo (Blanc and Richmond, 1980).

In this study, we focus only on the first two sources of thermospheric winds, as these are related to geomagnetically quiet periods. Figure 3.2 shows, for illustration purposes, the average thermospheric winds distribution at 110 km of altitude obtained from a simulation of the TIE-GCM numerical model (Richmond et al., 1992) performed by Yamazaki and Maute (2017). The simulation considered geomagnetically quiet equinox conditions: low geomagnetic activity given by Kp^2 index equal to zero, epoch given by 21st of September 2009, time given by 12h (universal time) and low solar activity given by F10.7 index equal to 72 sfu. It can be seen in Figure 3.2 how the average wind pattern varies spatially in this specific snap shot and that the semidiurnal tide is the major component of the wind field at the particular height considered in the simulation.

Here, we do not investigate thermospheric winds and related phenomena during geomagnetically disturbed periods, firstly because these are sporadic events (smaller data set) and secondly because they correspond to different geomagnetic and ionospheric dynamics which are out of the scope of this work.

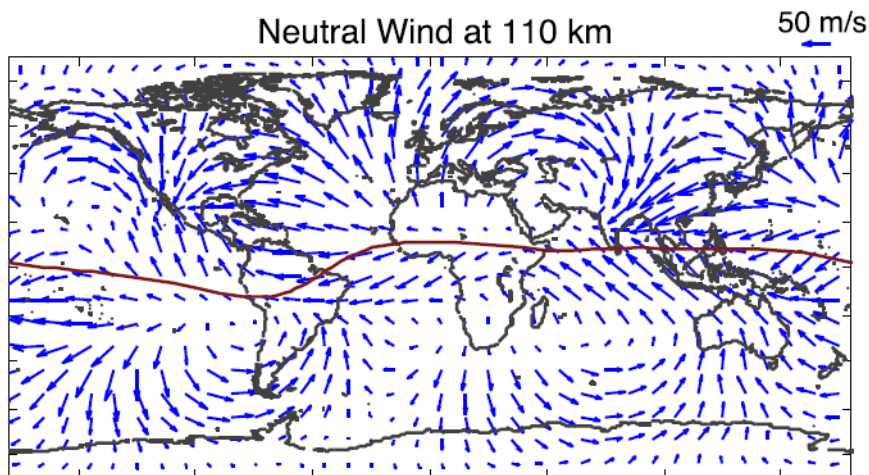


Figure 3.2: Thermospheric winds distribution at 110 km height obtained from TIE-GCM model simulations for geomagnetically quiet equinox conditions (Kp index = 0, 21st of September 2009, 12h universal time and low solar activity given by F10.7 = 72 sfu). From Yamazaki and Maute (2017).

²The geomagnetic three-hourly Kp index is derived from data of 13 selected magnetic observatories around the globe and it is provided by the GFZ-Potsdam (<https://kp.gfz-potsdam.de/en/>). It is designed to measure solar particle radiation by its magnetic effects and is considered a proxy for the energy input from the solar wind to Earth.

3.4 IONOSPHERIC ELECTRIC CURRENTS

Typically, in the dayside low-latitude ionosphere, the thermospheric winds set up the polarization electric field \mathbf{E} that usually points into the eastward direction. At low latitudes, a large-scale 24-h sun-synchronous variation dominates the neutral atmosphere motion, which is related to the so-called diurnal tides. The thermospheric winds triggered by such tidal dynamics drag the ions in the direction of the wind (Heelis, 2004). Considering the Lorentz force, the flow of ions across the ambient geomagnetic field causes their deflection, which forces them toward the dawn terminator. This effect causes a typical daytime build-up of positive ions near dawn and a lack of positive ions near dusk. This creates a polarization electric field due to wind-driven charge accumulation. This effect, along with electric field, geomagnetic field and the dawn/dusk terminators is illustrated in Figure 3.3.

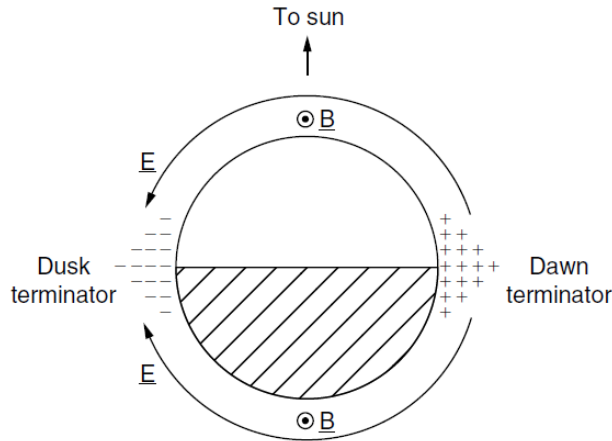


Figure 3.3: Diagram showing a view-from-above of the zonal electric field component, the equatorial geomagnetic field and the charge densities at the terminators. From Kelley (2009).

At the magnetic equator, where the magnetic field is exactly horizontal (i.e., I and Z equal zero and F equals H), the resulting upward $\mathbf{E} \times \mathbf{B}$ drift of the electrons generates a negative charge at the top and a positive charge at the bottom of the ionospheric E-region (about 90 to 130 km height). This secondary electric field prevents a further upward drift of electrons, which are then propelled westward by the eastward electric field. This westward movement of the electrons constitutes an eastward electric current flowing at around 110 km height and confined to an interval of $\pm 3^\circ$ latitude around the magnetic equator, which is called the Equatorial Electrojet (EEJ, Chapman, 1951, Yamazaki and Maute, 2017). The motion of the ions is largely inhibited at this altitude, due to their collisions with the neutral gas (Heelis, 2004). In other words, the process that amplifies the E-region electric field

involves the sum of Pedersen and Hall currents effects. The explanation of such a process lies on the Cowling effect, a mechanism that is valid for both global Sq and EEJ currents. However, its effects at the magnetic equator are stronger due to the horizontal ambient geomagnetic field.

The Cowling mechanism is illustrated schematically in Figure 3.4, which represents a scenario in the magnetic equator. The daytime eastward ionospheric electric field \mathbf{E}_1 gives rise to Pedersen currents $\sigma_P \mathbf{E}_1$ in the same direction, along with Hall currents $\sigma_H \mathbf{E}_1$ flowing downwards, perpendicular to both electric and geomagnetic fields. Because of the presence of poorly conducting boundaries above and below the E-region, the downward Hall currents lead to charge accumulation and further development of a vertical polarization electric field (\mathbf{E}_2). This upward electric field \mathbf{E}_2 generates a secondary upward Pedersen current $\sigma_P \mathbf{E}_2$ and an eastward Hall current $\sigma_H \mathbf{E}_2$. With that, the vertical but oppositely directed currents are balanced ($\sigma_H \mathbf{E}_1 \approx \sigma_P \mathbf{E}_2$), and the horizontal currents are summed constructively, resulting in a strong enhanced eastward current ($\sigma_P \mathbf{E}_1 + \sigma_H \mathbf{E}_2$). From these two relations, the equation 3.19 (and consequently 3.20) can be derived.

$$\sigma_P \mathbf{E}_1 + \sigma_H \mathbf{E}_2 = \left(\sigma_P + \frac{\sigma_H^2}{\sigma_P} \right) \mathbf{E}_1, \quad (3.19)$$

$$\sigma_H \mathbf{E}_2 = \left(\frac{\sigma_H^2}{\sigma_P} \right) \mathbf{E}_1. \quad (3.20)$$

The effective zonal conductivity $\sigma_P + \sigma_H^2/\sigma_P$ is called Cowling conductivity, maximized at the magnetic equator, and explains the current amplification related to the EEJ.

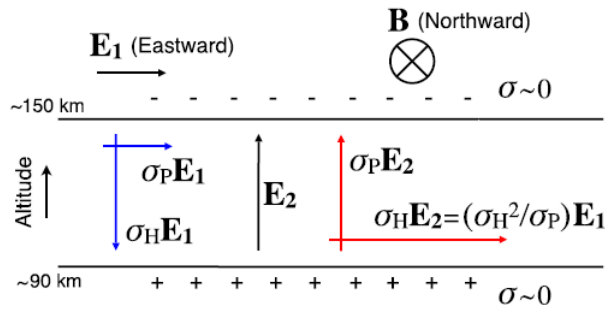


Figure 3.4: Enhancement of the eastward ionospheric current due to the Cowling effect. From Yamazaki and Maute (2017).

The resulting current density of the EEJ is on the order of 10^{-6} A/m², which is typically one order of magnitude greater than the solar-quiet (Sq) current (Onwumechili, 1997), which is the dominant current system at mid and low latitudes. Both Sq and EEJ currents are controlled by ionospheric conductivities, which depend on the plasma density and on the intensity of the geomagnetic main field

(Takeda, 1996; Cnossen, 2017). Additionally, the EEJ is accompanied by return currents, which flow at low latitudes (3-9° away from the magnetic equator) in the opposite direction and with lower strength compared to the EEJ (Onwumechili, 1992; Zhou et al., 2018a). The eastward flow of the EEJ is sometimes observed to reverse westwards, giving rise to the so-called equatorial counter electrojet (CEJ), a phenomenon that mainly depends on the variability of the atmospheric tides and its effects on the global wind system (Gouin, 1962; Mayaud, 1977; Marriott et al., 1979; Hanuise et al., 1983; Gurubaran, 2002; Zhou et al., 2018b; Soares et al., 2019b).

It is known that the Sq and EEJ currents drive the regular geomagnetic daily variation, which presents different patterns for different regions of the globe. In addition, the ionospheric currents undergo variability on various time scales (for example, solar cycle, season and day-to-day). Both spatial and temporal features of the geomagnetic daily variation can be mapped by satellite and ground based magnetometer measurements (Chapman, 1951; Marriott et al., 1979; Lühr et al., 2004; Olsen and Stolle, 2012). This quiet time geomagnetic daily variation is subjected to day-to-day changes in its amplitude and shape and a large part of the day-to-day variability causes are still to be explained (Yamazaki and Maute, 2017). This study deals with the regular geomagnetic daily variation and its spatio-temporal variations as described in Parts II and III.

Part II

USING PRINCIPAL COMPONENT ANALYSIS TO MODEL THE EQUATORIAL ELECTROJET AND DERIVE ITS TIDAL COMPOSITION

Part II was published in the Journal of Geophysical Research – Space Physics.

CHAPTER 4

SUMMARY AND INTRODUCTION

4.1 SUMMARY

The intensity of the equatorial electrojet (EEJ) shows temporal and spatial variability that is not yet fully understood nor accurately modeled. Atmospheric solar tides are among the main drivers of this variability but determining different tidal components and their respective time series is challenging. It requires good temporal and spatial coverage with observations, which, previously could only be achieved by accumulating data over many years. Here, we propose a new technique for modeling the EEJ based on principal component analysis (PCA) of a hybrid ground-satellite geomagnetic data set. The proposed PCA-based model (PCEEJ) represents the observed EEJ better than the climatological EEJM-2 model, especially when there is good local-time separation among the satellites involved. The amplitudes of various solar tidal modes are determined from PCEEJ based tidal equation fitting. This allows to evaluate inter- and intra-annual changes of solar tidal signatures in the EEJ. On average, the obtained time series of migrating and non-migrating tides agree with the average climatology available from earlier work. A comparison of tidal signatures in the EEJ with tides derived from neutral atmosphere temperature observations show a remarkable correlation for non-migrating tides such as DE3, DE2, DE4 and SW4. The results indicate that it is possible to obtain a meaningful EEJ spectrum related to solar tides for a relatively short time interval of 70 days.

4.2 THE GEOMAGNETIC DIURNAL VARIATION AND THE EQUATORIAL ELECTROJET

An important part of the geomagnetic variations recorded both at ground and at satellite altitudes is related to the dynamics of the Earth's upper atmosphere. The upper atmosphere consists of a combination of neutrals and plasmas. The plasma

constituent is produced by the ionization of neutrals due to their photodissociation caused by energetic short-wavelength (<150 nm) solar radiation, giving rise to the so-called ionosphere.

The dayside E-region ionosphere is electrically conductive due to the presence of free electrons and ions and an appropriate ion-neutral collision frequency. In the presence of the geomagnetic main field and subjected to tidal winds, electric fields and currents are generated. This process is referred to as the ionospheric dynamo, which can be described by:

$$\mathbf{J} = \hat{\sigma}(\mathbf{E} + \mathbf{U} \times \mathbf{B}), \quad (4.1)$$

where \mathbf{J} is the current density, $\hat{\sigma}$ is the ionospheric conductivity tensor, \mathbf{E} is the electric field, \mathbf{U} is the neutral wind and \mathbf{B} is the ambient geomagnetic field. This expression shows the connection between ionospheric dynamo currents and driving winds in the neutral atmosphere, including tidal winds. Geomagnetic diurnal variation, which reaches amplitudes of about 200 nT at ground, results from the ionospheric currents generated through the process expressed by Equation 4.1.

At the magnetic equator, the magnetic field is exactly horizontal, and the zonal electric field sets up a vertical polarization electric field by driving vertical Hall currents. This gives rise to an additional zonal current superposed to that caused by the original background electric field. This leads to an amplification of the eastward electric current flow at around 110 km height, confined within $\pm 3^\circ$ latitude around the magnetic equator. The resulting enhanced current is known as the equatorial electrojet (EEJ, e.g., [Forbes, 1981](#), [Yamazaki and Maute, 2017](#)).

The EEJ was discovered after the installation of the first geomagnetic observatories at magnetic equator latitudes due to its associated abnormally large horizontal component diurnal variation ([Chapman, 1951](#)). Since then, many EEJ features were reported by different studies, as its dependence on local time, longitude, season, solar flux, main geomagnetic field and lunar phase (e.g., [Forbes et al., 2008](#); [Onwumechili, 1997](#); [Yamazaki and Maute, 2017](#)). With magnetic data from dedicated satellite missions and its unprecedented longitudinal coverage, the EEJ spatio-temporal variation became much better described and understood (e.g., [Lühr et al., 2004](#); [Alken and Maus, 2007](#)).

The quiet-time EEJ intensity exhibits variations on day-to-day to year-to-year time scales. Year-to-year changes are mainly due to the 11-year solar flux variation (e.g., [Matzka et al., 2017](#)), but are also weakly driven by the secular variation of the main field (e.g., [Cnossen and Richmond, 2013](#); [Soares et al., 2019a](#)) as well as neutral winds (e.g., [Yamazaki et al., 2018](#)). Seasonal variations of the EEJ are attributed in part to changes in the solar zenith angle ([Chapman and Rao, 1965](#))

but more importantly to neutral winds (Yamazaki et al., 2014b). The EEJ day-to-day changes are primarily due to variable neutral winds (Miyahara and Ooishi, 1997; Fang et al., 2013; Yamazaki et al., 2014a). Large variability of neutral winds can be explained by upward-propagating waves from the regions below the ionosphere (e.g., Liu, 2016). Among various types of waves, atmospheric tides are particularly important for driving the EEJ, as they attain large amplitudes at dynamo region heights (e.g., Oberheide et al., 2011). Tides play a significant role not only for temporal variations of the EEJ but also for the longitudinal structure of the EEJ (e.g., Lühr et al., 2008; Soares et al., 2018a).

Atmospheric solar tides are global scale waves that oscillate periodically in time and propagate vertically and zonally in space (Forbes et al., 2008). Different tidal components $\xi_{n,s}$ can be described mathematically as:

$$\xi_{n,s} = A_{n,s} \cos(n\omega t + s\lambda - \Phi_{n,s}), \quad (4.2)$$

where $A_{n,s}$ and $\Phi_{n,s}$ are the amplitude and phase of $\xi_{n,s}$, respectively. The variable t is universal time, ω is the rotation rate of the Earth, λ is longitude, n is the subharmonic of a day (where $n=1, 2, 3, 4$ correspond to oscillations with periods of 24h, 12h, 8h and 6h, called diurnal, semidiurnal, terdiurnal and quarterdiurnal tides, respectively), and s is the zonal wavenumber ($s<0$ for waves propagating eastwards and $s>0$ for waves propagating westwards).

The tides with $n=s$ are called migrating tides as they propagate westwards with the same speed as the apparent motion of the Sun from the perspective of ground observers. All other tides ($n \neq s$) are called non-migrating tides. Different combinations of n and s represent different tidal modes, which can arise from different excitation mechanisms (e.g., Miyoshi et al., 2017). It is common to use a combination of two letters and one number as a notation to denote specific tidal modes (e.g., DE3, SW6, TW2, ...). The first letter stands for the period of oscillation (D=diurnal, S=semidiurnal, T=terdiurnal, Q=quarterdiurnal, ...), the second letter refers to the direction of propagation (W=westward or E=eastward) and the number is the zonal wavenumber.

By fitting Equation 4.2 to magnetic field measurements from the CHAMP satellite, Lühr and Manoj (2013) determined the average spectrum of the EEJ related to solar tides. They separated 10 years of the CHAMP data into monthly subsets for 2000-2005 (around solar maximum) and 2005-2010 (around solar minimum) periods. The fitting was performed on each of the 24 subsets of data so that the average seasonal dependence of different tidal modes could be determined for different levels of solar activity. The limitation of this approach is that it cannot resolve the tidal variability of the EEJ for individual years. It requires splitting the data into shorter time

windows to overcome this limitation. However, doing so would reduce the data available for the fit and the stability of the inverse problem being solved.

Instead of the actual raw observations, an EEJ model could be used in order to determine the EEJ spectrum related to solar tides. There are various types of EEJ models, obtained with different techniques and purposes. Those include, for example, the modelling of the EEJ ground magnetic effects (Doumouya et al., 2003; Hamid et al., 2015), the EEJ theoretical modelling (Sugiura and Poros, 1969; Richmond, 1973; Anandarao and Raghavarao, 1987), the EEJ morphology modelling (intensity, width, and position - Fambitakoye and Mayaud, 1976; Doumouya et al., 1998; Rigoti et al., 1999) and the EEJ climatology modelling by satellite data (Alken and Maus, 2007).

4.3 OBJECTIVES AND SCIENTIFIC CONTRIBUTION

In this work we propose a new technique aiming to accurately model the EEJ. Improved modelling of the EEJ allows a stable determination of the EEJ spectrum related to solar tides for individual years. To avoid problems during inversion related to the sparsity and quality of the data, we use a principal component analysis (PCA) technique to model an initial EEJ data set. Our approach is based on the combination of ground and satellite EEJ data, since ground data provides very good local time coverage and satellite data provides very good longitudinal coverage, maximizing the spatio-temporal coverage needed when Equation 4.2 is considered.

The beauty of this study is that it not only allows us to understand the physical process controlling EEJ variability, which is an interesting feature in its own right, but it also allows us to probe the upper atmosphere by the use of ground and satellite magnetometer data. Especially, the impact of evaluating tidal variability would be significant as it is otherwise difficult to quantify. Our objectives are:

- Obtain an accurate EEJ model based on the PCA technique which can be used for analysing the solar tides composition within the EEJ variability.
- Determine the dominant tidal modes responsible for EEJ variability, within a time scale of few days or months, by using geomagnetic ground and satellite data.
- Derive time series of upper atmosphere tides amplitude and look for correlation with other atmospheric data sets (e.g., atmospheric temperature data sets).

The proposed work directly relates to progress in understanding ionosphere / thermosphere coupling processes. The influence of the lower and middle atmosphere

on the variability of the upper atmosphere will be addressed in the context of tidal forcing to the EEJ.

This work is also relevant to current systems of the ionosphere, as it examines the EEJ, which is the most prominent feature of the dayside equatorial ionospheric currents. The outcome of this work will contribute to geomagnetic field modelling in two different aspects: first by providing a new EEJ model and, second, by providing information on the excitation mechanism of the EEJ variability, related to solar tides. The solar tides amplitudes and their temporal variation are used as inputs for other models, such as the first-principles model TIEGCM ([Qian et al., 2014](#); [Richmond et al., 1992](#)).

CHAPTER 5

DATA AND MODEL

Data sets from 2000 to 2019 were used and the sub-sections below detail the type and origin of each data set.

5.1 GROUND-BASED MAGNETIC DATA

Hourly mean values in units of nanotesla from geomagnetic observatories and magnetometer stations were used. The hourly time resolution is sufficient for resolving the local-time variation of the EEJ and it makes the inversion computationally less expensive. Minute mean values were also used during data pre-processing, as it will be explained in Section 6.1. The data was constrained to geomagnetically quiet periods with the geomagnetic activity index Kp (Matzka et al., 2021) being less than or equal to 3. It is true that some remaining isolated periods of enhanced geomagnetic activity, such as solar flare events, can not be well represented by the Kp index. However, in this study, such events will appear as time-limited outliers and will be naturally filtered during the PCA modelling.

To obtain EEJ data from the ground-based magnetometer data, we used the 2-station method described in Soares et al. (2018a). To extract the EEJ signal, we calculated the difference between the H component measured at an equatorial station and at a low-latitude station with a similar longitude, but outside the influence of the EEJ. The equatorial and low-latitude stations used in this study are listed in Table 5.1 and shown in the map of Figure 5.1. Then, the nighttime quiet level is defined for each longitude by calculating the average for each night by using an interval of 4 hours around local midnight and, then, linearly interpolating a baseline between successive nighttime averages. After subtracting the nighttime baseline, the final EEJ signal at the longitude of the equatorial station is obtained, being hereinafter referred to as ΔH .

Table 5.1 lists all the ground observatories and stations used to derive the EEJ

signal, their type (equatorial or low-latitude), sector (identifier of longitudinal sector), source of data, geographic latitude and longitude. A total of eight longitudinal sectors (I up to VIII) are used as sources of ground-based data in the analysis. In Table 5.1, the sector VII shows one equatorial station (DAV) and two low-latitude stations (MUT and TND) because TND is used for 2017, when MUT data is not available. The data providers and data repositories used are listed in Table 5.1. The complete data set is not provided in a free on-line data repository because most of the individual data sets were provided following data usage rules that impose limitations on the data sharing.

Figure 5.1 indicates the geographical positions of the equatorial (red circles) and low-latitude (blue circles) stations, as well as the magnetic equator for 2017. Figure 5.1b is a longitude versus time plot indicating the data availability for each ground station from 2000 until 2019 (red and blue lines). Note that if a data gap occurs either at the equatorial or at the low-latitude station, there will be a correspondent data gap in the EEJ data set. Some station pairs provide quite continuous records, namely HUA-PIU (Peru), TTB-KOU (Brazil) and TIR-ABG (India).

5.2 SATELLITE MAGNETIC DATA

Geomagnetic data from the Ørsted, CHAMP, SAC-C and Swarm satellite missions were used. Ørsted operated from February 1999 to January 2014 in a near polar orbit with an inclination of 96.5° , an apogee around 865 km and a perigee around 650 km, drifting slowly in local time by -0.88 minutes per day (Neubert et al., 2001). CHAMP operated from July 2000 to September 2010 with a local time drift rate of 5.44 minutes per day, starting its operation at a height of 454 km and progressively decayed until 200 km in 2010 (Reigber et al., 2002). SAC-C operated from November 2000 to August 2013 (data after 2010 is not used in this study to be consistent with CHAMP data availability) in a polar circular orbit of altitude 702 km with an inclination of 98.2° (Colomb et al., 2004). Its orbit is sun-synchronous, and it remains sampling at a fixed local time of around 10:25 AM. Swarm is a constellation of three satellites launched in November 2013 (Friis-Christensen et al., 2006, 2008) and still under operation. Swarm A and C fly at an altitude of around 450 km, while Swarm B flies at an altitude of around 530 km. The Swarm satellites drift faster in local time than the other missions, at an average rate of 10.5 minutes per day. The satellite data can be divided in two periods, according to its availability through time: the CHAMP/SAC-C/Ørsted (CSØ) period from 2000 until 2010 (indicated as green area in Figure 5.1b) and the Swarm period from 2014 until 2019 (magenta area in Figure 5.1b). There is a data gap between the end of the CSØ period and beginning of the Swarm period, as also indicated in Figure 5.1b.

Table 5.1: Summary with the equatorial and low-latitude ground stations used to derive the EEJ data. Their correspondent data repository and geographical coordinates (in degrees) are also shown.

STATION	TYPE	SECTOR	DATA REPOSITORY	LAT.	LON.
HUA	Equatorial	I	INTERMAGNET	-12.05	-75.33
PIU	Low-Latitude	I	LISN	-5.20	-80.60
TTB	Equatorial	II	GFZ Data Services, INTERMAGNET	-1.20	-48.51
KOU	Low-Latitude	II	INTERMAGNET	5.21	-52.73
SAM	Equatorial	III	WAMNET	11.39	-5.62
TAM	Low-Latitude	III	INTERMAGNET	22.79	5.53
TIR	Equatorial	IV	WDC-Mumbai	8.70	77.80
ABG	Low-Latitude	IV	INTERMAGNET	18.64	72.87
PKT	Equatorial	V	NICT Sealion	8.09	98.32
KTB	Low-Latitude	V	210° Meridian Chain	-0.20	100.32
BCL	Equatorial	VI	MAGDAS	9.32	105.71
PHU	Low-Latitude	VI	INTERMAGNET	21.03	105.95
DAV	Equatorial	VII	MAGDAS	7.00	125.40
MUT	Low-Latitude	VII	MAGDAS	14.40	121.00
TND	Low-Latitude	VII	WDC-Edinburgh	1.29	124.95
YAP	Equatorial	VIII	MAGDAS	9.30	138.50
GUA	Low-Latitude	VIII	INTERMAGNET	13.58	144.87

The satellite EEJ data used in this work were a pre-processed data, given as electric current intensity values in mA/m. These EEJ electric current intensity data were obtained by inverting the observed satellite magnetic field data based on a EEJ current sheet model. To perform the inversion, first, it is necessary to remove the core (by the CHAOS-6 model, [Finlay et al., 2016](#)), lithospheric (by the MF7 model, [Maus et al., 2008](#)), magnetospheric (by the POMME-6 model, [Maus and](#)

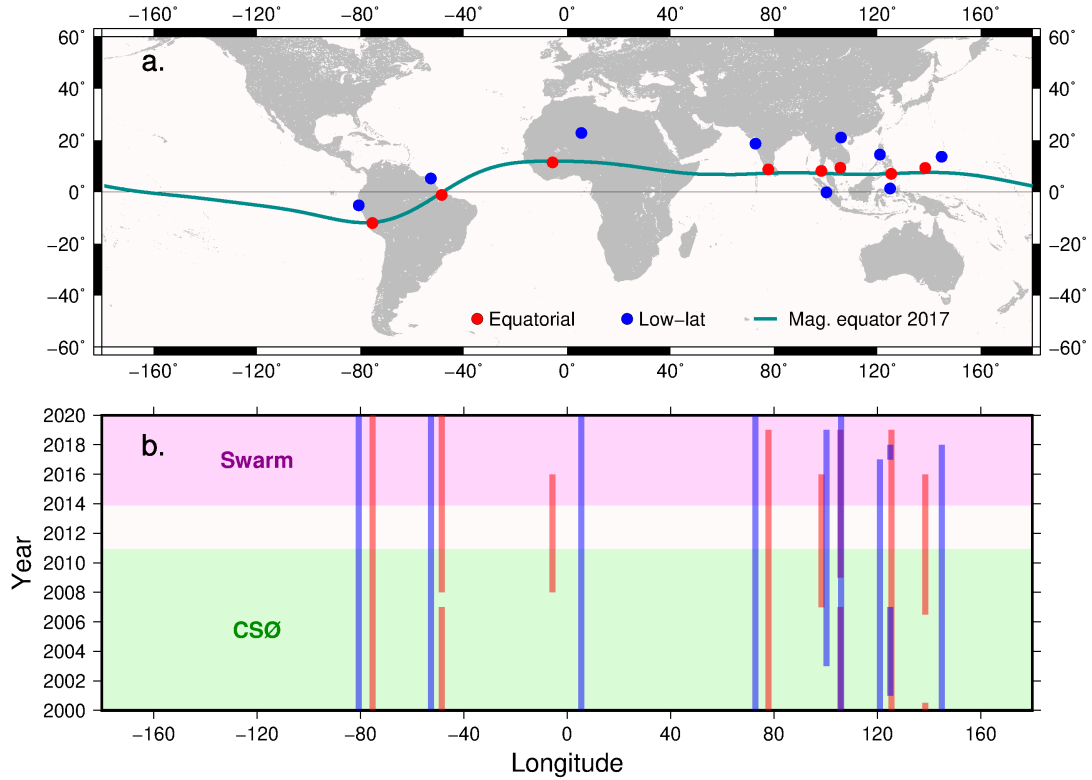


Figure 5.1: (a) Map with the equatorial (red circles) and low-latitude (blue circles) stations used to obtain the ground-based EEJ data. The magnetic equator for 2017 is shown as a green line. (b) Longitude versus time plot indicating the data availability of each ground station shown in the panel a (red and blue lines) and of the satellite missions (Swarm as purple area and CHAMP/SAC-C/Ørsted as green area with CSØ label), for the period from 2000 until 2019.

Lühr, 2005), and S_q (by fitting a low-degree spherical harmonic field model to the higher-latitude data) magnetic fields from the original 1Hz magnetic field data that comes from a scalar magnetometer. After removing these contributions, the residual data represents the latitudinal magnetic signature of the EEJ current for every orbit on the day-side. Then, the EEJ magnetic signature along each track is inverted for an estimate of its height integrated current. To do this, we considered a simple sheet current model of line currents spaced at 0.5 degrees, flowing longitudinally eastward along lines of constant quasi-dipole latitude, and at an altitude of 110 km. In this work, only the peak EEJ value at the magnetic equator is used (i.e., no latitudinal averaging is performed). This approach is presented and explained in detail in Alken et al. (2013). Like the ground-based data, the K_p index ≤ 3 criteria was also used to constrain the satellite data to geomagnetically quiet periods.

To guarantee that the EEJ variation is represented similarly by the different satellite data sets, we performed an inter-calibration of Swarm, CHAMP, Ørsted and SAC-C data by using a common reference data set. The EEJM-2 model (Alken and

(Maus, 2007; detailed in section 5.4) was used as the reference data set. We calibrated each satellite data set by minimizing its differences to the EEJM-2 reference values. This minimization was achieved by finding linear transformation coefficients c_1 and c_2 according to the following equation:

$$\mathbf{b}_{\text{sc}} = c_1 \cdot \mathbf{b}_{\text{s}} + c_2, \quad (5.1)$$

where \mathbf{b}_{s} and \mathbf{b}_{sc} are the initial and calibrated satellite data, respectively. The coefficients c_1 and c_2 were determined separately for each satellite data set, as listed in Table 5.2. This procedure was used to minimize any bias or sensitivity differences between the satellite data sets. The effect of the different satellite orbital altitudes was already addressed during the EEJ current modelling by the Bio-Savart law (Alken et al., 2013). Therefore, no further altitude correction is necessary, as the current intensities are always estimated at the same reference of 110 km height.

Table 5.2: Summary with the linear transformation coefficients c_1 and c_2 for each satellite.

SATELLITE	c_1	c_2
Swarm A and C	0.8511	1.3254
Swarm B	0.8600	-1.5380
CHAMP	0.9353	-2.0449e-5
SAC-C	0.7987	-7.6188
Oersted	0.7073	2.0909e-4

Figure 5.2 shows an overview of the satellite missions data availability versus the altitude of the spacecraft.

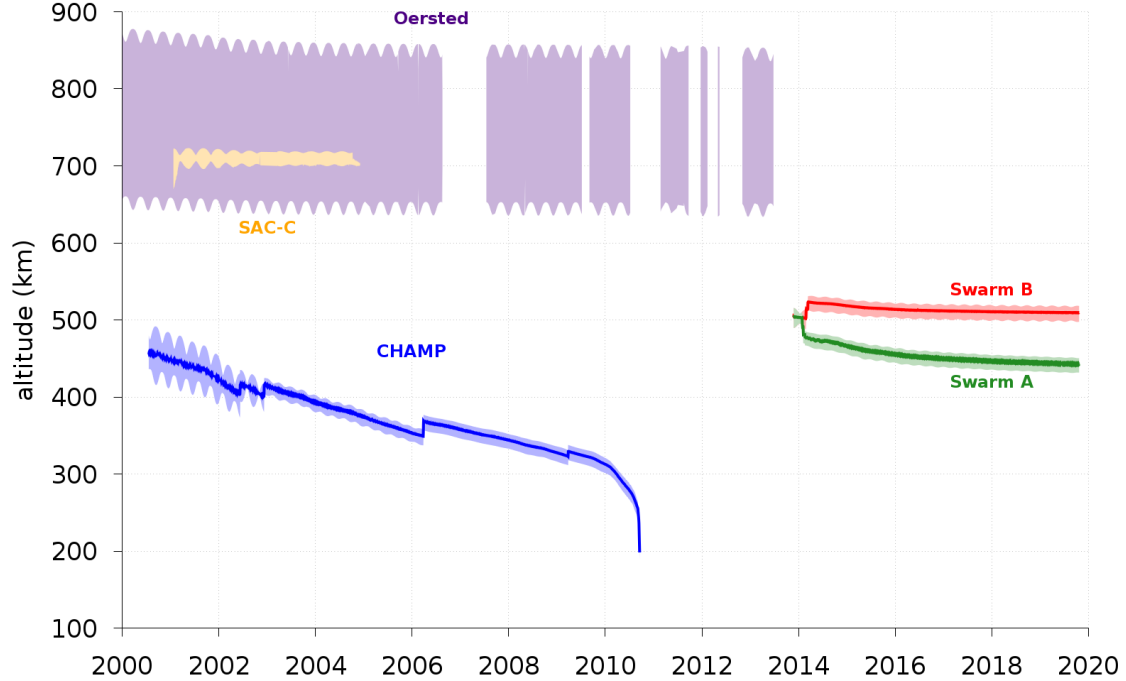


Figure 5.2: Satellite altitude variation with time for Ørsted, SAC-C, CHAMP and Swarm missions. Courtesy of Dr. Patrick Alken (NOAA, USA).

5.3 SABER TEMPERATURE SATELLITE DATA

Tidal signatures in the EEJ are compared with tides in the neutral atmosphere. The tides that affect the EEJ current involve temperature perturbations in the same height interval, and therefore similarity can be expected in temporal variations of tidal signatures in the EEJ and temperature.

We use atmospheric temperature data from the NASA TIMED (Thermosphere Ionosphere Mesosphere Energetics Dynamics) satellite (Kusnierkiewicz, 2003). The TIMED temperature data is recorded by its SABER (Sounding of the Atmosphere using Broadband Emission Radiometry) instrument (Russell III et al., 1999). The SABER instrument performs global measurements of the atmosphere using a 10-channel broadband limb-scanning infrared radiometer covering the spectral range from $1.27 \mu\text{m}$ to $17 \mu\text{m}$. SABER observes infrared emissions from CO_2 , O_2 , H_2O , NO , O_3 and OH . The measured thermal infrared radiance values are then mathematically inverted to obtain some of the mission data products (Russell III et al., 1999), including atmospheric temperature that is used in this work. SABER temperature data have been widely used for studying tides in the mesosphere and lower thermosphere region (e.g., Russell III et al., 1999; Forbes et al., 2008; Oberheide et al., 2009).

5.4 EEJM-2 CLIMATOLOGICAL MODEL

The EEJM-2 is an empirical climatological model of the EEJ based on CSØ satellite data (Alken and Maus, 2007). Besides its use in the satellite data intercalibration, the model is also used to evaluate the effectiveness of our PCA model in representing the EEJ variations. The EEJM-2 model was chosen as a reference for comparison due to two main reasons. First, like our PCA proposed model, the EEJM-2 is an empirical model which takes advantage of important longitudinal coverage from satellite data. Secondly, unlike the other aforementioned EEJ models, the EEJM-2 is publicly available (<https://geomag.colorado.edu/equatorial-electrojet-model-eejm2.html>).

EEJM-2 uses different basis functions to represent the EEJ longitudinal, local time, season and solar flux dependence. With our PCA approach, we aim at obtaining different basis functions to capture the EEJ variations.

CHAPTER 6

EEJ MODELING AND ITS INVERSION FOR SOLAR TIDES

Our strategy can be divided in two parts: first, performing an improved EEJ modeling and, secondly, obtaining its spectrum related to solar tides.

The EEJ modeling consists of three main steps. First, the ground and satellite EEJ data are combined to form a hybrid data set with common unit of measure. Second, EEJ basis functions are derived from multi-year satellite observations using the PCA method. Then, in the last step, the EEJ is modeled by fitting the PCA basis functions to the combined ground-satellite data. The obtained PCA model will be hereinafter called as PCEEJ model. This approach allows us to model the EEJ for a specific time of an individual year, a resolution that is not available in previous empirical models.

The tidal analysis part is performed after the PCEEJ model is obtained. The tidal components, which are oscillations defined by different periods and wavenumbers, are fitted to the PCEEJ model by using Equation 4.2 and considering windows of 70 days per fit, which is approximately the period needed by the Swarm satellites to cover all local times. These fits provide the importance of each tide in the modeled EEJ as a time series. Lastly, comparisons between geomagnetic EEJ data analysis and SABER temperature data analysis are performed to evaluate their level of similarity. This comparison is useful to confirm whether the PCEEJ has a realistic tidal composition or not, since the SABER analysis correspond to fitting tides oscillations directly to the observations and not to modelled data.

6.1 COMBINING GROUND AND SATELLITE EEJ DATA

In order to gain the best possible local time and longitudinal coverage for EEJ observations, we combine ground-based (expressed as ΔH in nT) and satellite (ex-

pressed as peak height integrated current density ICD, in mA/m) EEJ data. To keep all observations with the same unit of measure prior to running the inversion, we converted the ΔH data given in nT to mA/m, according to the following relation:

$$\Delta H = s \cdot ICD + i, \quad (6.1)$$

where s and i are the slope and linear coefficients, respectively. These coefficients were determined by linear regression, since the relationship between ΔH and ICD should be linear for the same longitude (Manoj et al., 2006). This was done by selecting ground and satellite data from the same temporal interval in a longitude interval defined as the longitude of the ground data $\pm 5^\circ$. For this purpose, we used ground data with the temporal resolution of one minute, and the analysis was made separately for different local times to take into account the local time dependence of the ΔH and ICD linear relation.

Figure 6.1 shows scatter plots of ICD vs ΔH for eight longitudinal sectors that have ground data available during the Swarm data period (see Table 5.1). In Figure 6.1 panels, data from all local times are shown together, with no distinction, to facilitate the visualization. The scatter plots confirm that a linear relation exists for all longitudinal sectors and a linear fit for each sector is shown at each panel of Figure 6.1, together with the corresponding linear fit coefficients s and i . This linear relation is not surprising, since it is expected from the Ampère’s law that a stronger electric current will generate a more pronounced magnetic field.

6.2 PRINCIPAL COMPONENT ANALYSIS (PCA)

Like the Fourier analysis, the PCA uses a series of orthogonal functions, but it does not use a fixed set of basis functions. The purpose of PCA is to find linear combinations of the data which are uncorrelated with each other and maximize the variance explained in the data, as mentioned for example in Alken et al. (2017), which also applied PCA technique to data of ionospheric currents. It indicates which parts of a data set provide redundant information or noise that are not useful for understanding a given system. In practice, it also acts as a filter and reduces the dimensionality of a complex data set. This is achieved after constructing a covariance matrix of all the data and deriving the associated eigenvalues and eigenvectors. The eigenvalues represent the amount of variance explained by each eigenvector, and the eigenvectors represent the principal components (basis functions) that describe the initial data set. Based on cumulative variance analysis, the most important principal components are used to model the data (Alken et al., 2017).

Fitting selected PCA basis functions to the initially sparse EEJ data set yields a

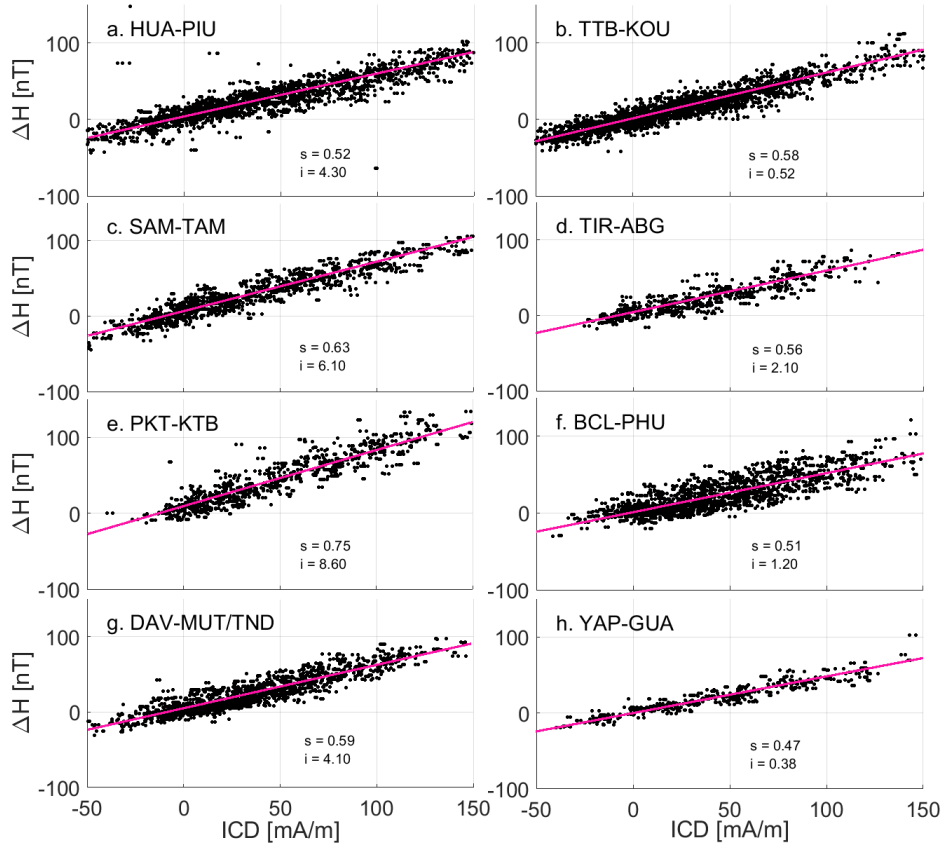


Figure 6.1: Relation between ground-based (ΔH , in nT) and satellite (ICD, in mA/m) EEJ data for eight considered longitudinal sectors, represented by the ground stations of HUA-PIU (a), TTB-KOU (b), SAM-TAM (c), TIR-ABG (d), PKT-KTB (e), BCL-PHU (f), DAV-MUT/TND (g) and YAP-GUA (h). Satellite data is from Swarm A and B satellites. Pink lines show a linear fit for each longitudinal sector. The estimated slope s and linear coefficient i values of the linear fit are shown in each panel. Data from all local times are considered in the panels.

densified EEJ data. This is important because the usage of modelled and densified EEJ data helps to stabilize the inversion when extracting solar tidal signatures from the data set in a later step. For our PCA analysis, the idea is to use a very large satellite data set, with good longitude and local time coverage, to derive the basis functions. Thus, we have used a total of 17 years of satellite data: 11 years from CSØ period and 6 years from Swarm period. Data from SAC-C and ground were not used in this step because they are limited to specific local time and longitudes, which could lead to certain level of bias in the basis functions.

The first step in PCA is to grid the data set according to longitude and local time bins. We found that increments of 10° in longitude and 1h in local time provide an optimum grid configuration, ensuring the presence of a substantial amount of data points in each bin. Figure 6.2 shows this grid, with dimensions of 36×12 , resulting in 432 bins.

The second step is to construct an EEJ time series matrix \mathbf{X} . As indicated in Figure

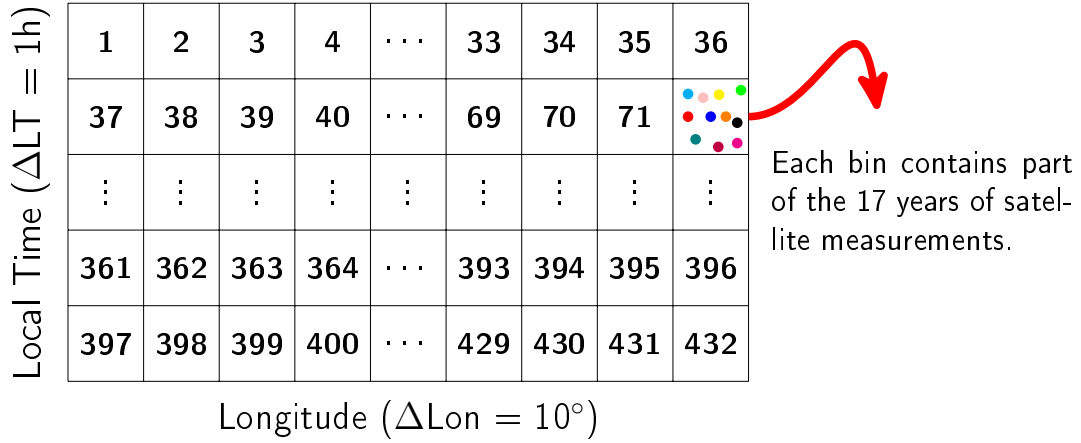


Figure 6.2: Sketch of the initial longitude versus local time data grid to be applied in the PCA. Here, the optimum 36x12 grid is shown, with a total number of 432 bins. The numbering of each bin is shown, starting at bin number 1 and ending at bin number 432.

6.2 (red arrow), each grid bin contains some of the 17 years worth of EEJ satellite measurements. The time series matrix \mathbf{X} reorganizes this information by splitting the data according to day of year (DoY). \mathbf{X} has the dimension 432x365, with 432 lines from the longitude and local time binning and 365 columns representing the 365 days of the year (from January 1st until December 31st). Each element of \mathbf{X} is given as an average value, since more than one sample can be found with the same longitude, local time and DoY.

The third step is the calculation of the covariance matrix \mathbf{COV} related to \mathbf{X} , as given by equation below:

$$\mathbf{COV} = \frac{1}{N} \mathbf{X} \mathbf{X}^T, \quad (6.2)$$

where N ($=365$) is the number of samples for each bin. The eigenvalues and associated eigenvectors of the covariance matrix \mathbf{COV} are computed and stored in the matrices \mathbf{V}_{val} and \mathbf{V}_{vec} , respectively. The matrix \mathbf{V}_{val} is a 432x432 diagonal matrix which is sorted in descending order, according to the eigenvalues, as shown in the equation below:

$$\mathbf{V}_{val} = \begin{bmatrix} \lambda_1 & 0 & \dots & 0 & 0 \\ 0 & \lambda_2 & \dots & 0 & 0 \\ \vdots & \vdots & \ddots & \vdots & \vdots \\ 0 & 0 & \dots & \lambda_{(d-1)} & 0 \\ 0 & 0 & \dots & 0 & \lambda_d \end{bmatrix} \quad (6.3)$$

where $\lambda_1 > \lambda_2 > \dots > \lambda_d$ and $d = 432$.

The matrix \mathbf{V}_{vec} is a 432x432 matrix which contains the principal components (PCs) basis functions of EEJ variation in its columns, as shown in the equation below:

$$\mathbf{V}_{vec} = \begin{bmatrix} v_{11} & v_{12} & \dots & v_{1(d-1)} & v_{1d} \\ v_{21} & v_{22} & \dots & v_{2(d-1)} & v_{2d} \\ \vdots & \vdots & \ddots & \vdots & \vdots \\ v_{(d-1)1} & v_{(d-1)2} & \dots & v_{(d-1)(d-1)} & v_{(d-1)d} \\ v_{d1} & v_{d2} & \dots & v_{d(d-1)} & v_{dd} \end{bmatrix} \quad (6.4)$$

where PC1 is given by column 1, PC2 by column 2, ..., PCd by column d.

To capture the most important sources of variance within the data and therefore reduce its dimensionality, only a small number of PCs are selected to model the EEJ variation. Two methods were used to determine the number of PCs: the cumulative variance plot and the visual inspection of the PCs. The cumulative variance of the i -th eigenvalue is defined as:

$$CV_i = \frac{\sum_{j=1}^i \lambda_j}{\sum_{j=1}^d \lambda_j}, \quad (6.5)$$

where $d = 432$, the total number of eigenvalues of the matrix \mathbf{COV} . Figure 6.3 shows the obtained cumulative variance plot. From a total of 432 eigenvalues, more than 95% of the variance within the data can be explained by the first 10 PCs.

With the cumulative variance plot, we also calculated its invariance, defined as:

$$I_i = \frac{CV_{i+1} - CV_i}{CV_i}, \quad (6.6)$$

where I_i is the metric of invariance of the cumulative variance shown in Figure 6.3. We found that at the 10th PC, the rate of change represented by the invariance metric is already small and below 0.003. Above the 10th PC, the rate of change gets even smaller. This metric also indicates that using the first 10 PCs is suitable for our purpose.

Figure 6.4 shows the first 10 PCs, organized in the longitude versus local time grid. The visual inspection of Figure 6.4 confirms that the first 10 PCs present structured spatio-temporal features (panels a to j). For instance, the most important contribution comes from PC1 (panel a), which resembles the average spatio-temporal variation of the EEJ, as seen in previous studies (Lühr et al., 2008; Lühr and Manoj, 2013).

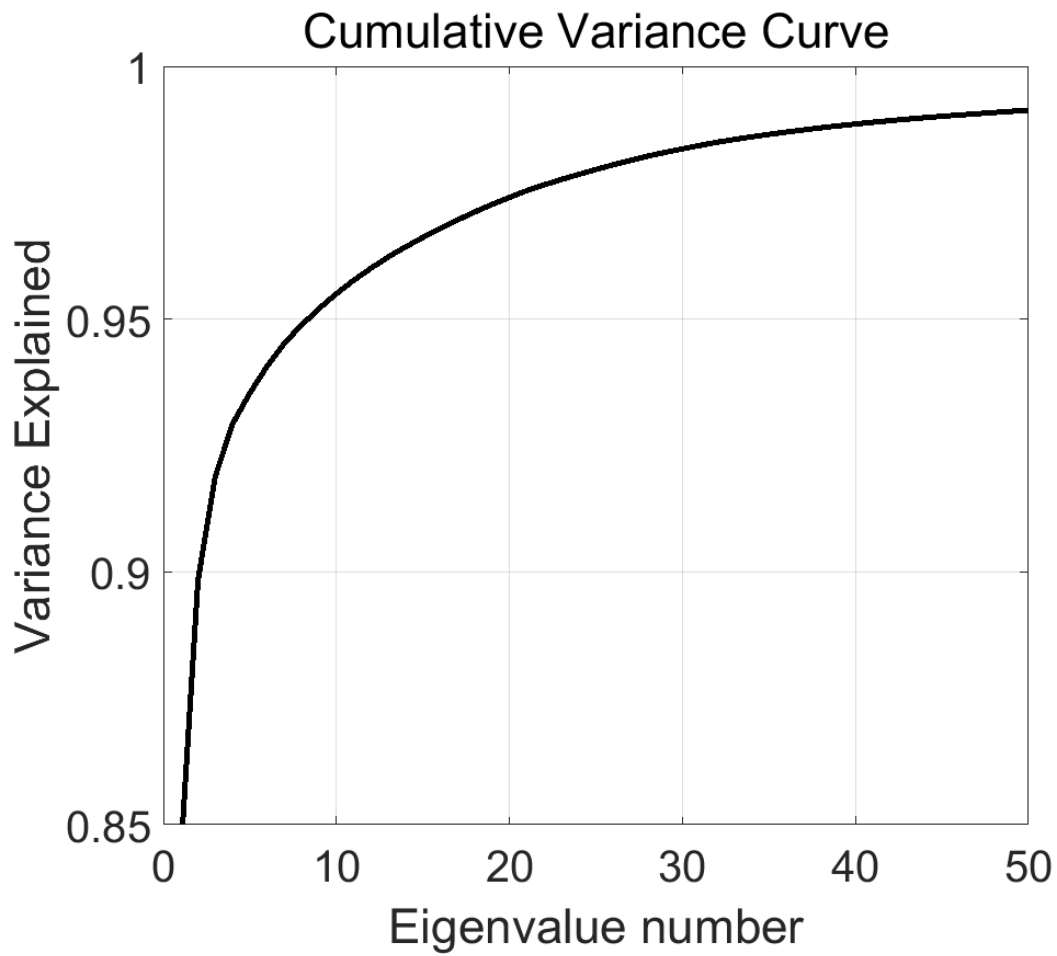


Figure 6.3: Cumulative variance explained by the principal components, based on the associated eigenvalues. Only eigenvalues from 1 to 50 are shown for better visualization.

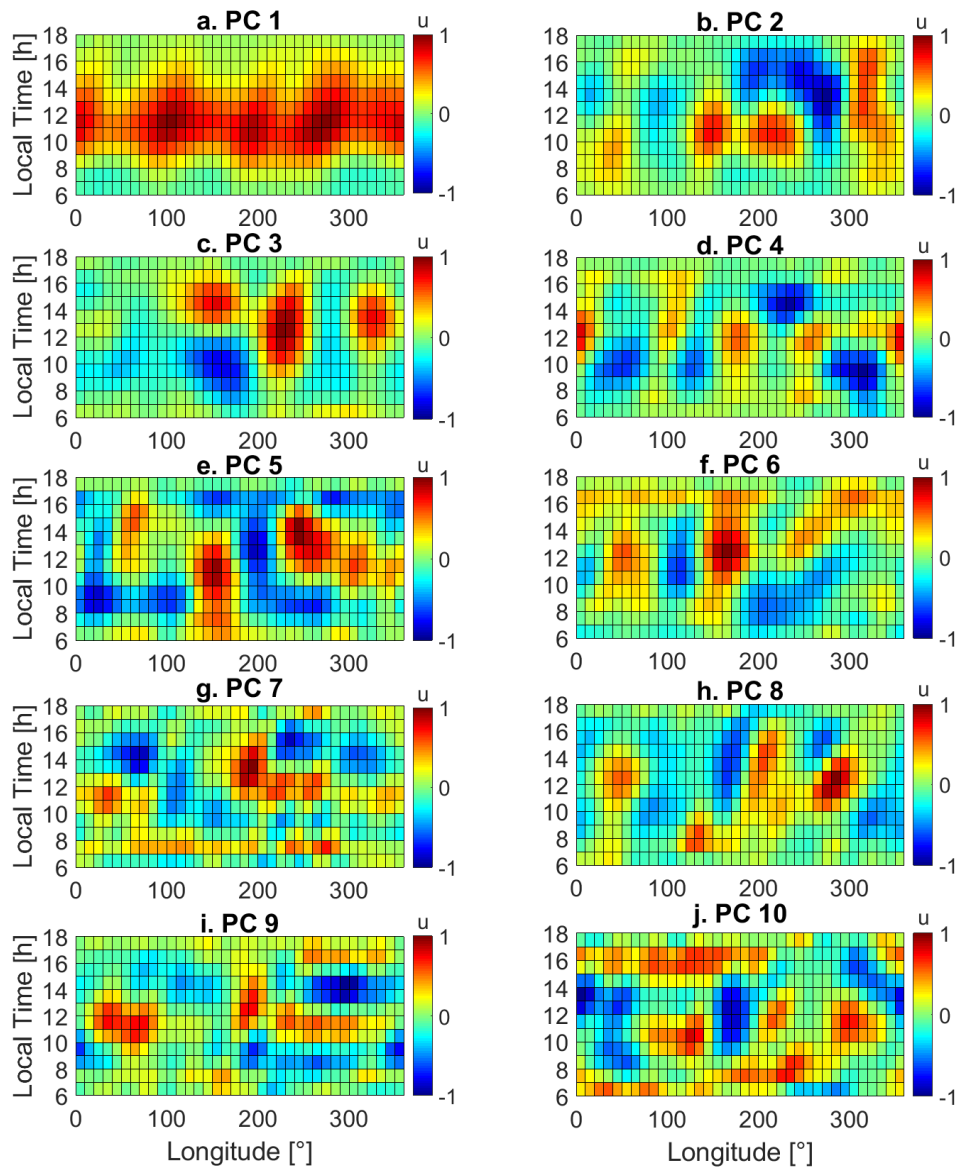


Figure 6.4: Principal components 1 to 10 (panels a to j, respectively), derived from EEJ satellite data. Note that the color bar shows normalized units of variation between -1 and +1. This normalization was done independently for each principal component.

6.2.1 PRINCIPAL COMPONENTS FIT

The PCEEJ was obtained by fitting the PCA basis functions to the hybrid ground-satellite data set. This was done by representing the available data set as a linear combination of the 10 PCA basis functions, as shown in the equation below:

$$\tilde{\mathbf{b}} = \alpha_1 \cdot \mathbf{PC}_1 + \alpha_2 \cdot \mathbf{PC}_2 + \cdots + \alpha_{10} \cdot \mathbf{PC}_{10}, \quad (6.7)$$

where $\tilde{\mathbf{b}}$ stands for the predicted PCEEJ model, α_i stands for the unknown PCs amplitudes that will be estimated and \mathbf{PC}_i are the normalized basis functions shown in Figure 6.4. Equation 6.7 builds up a linear system in which the amplitudes α_i are unknown parameters to be determined. To estimate α_i , we solved a minimization problem based on a least-squares solution, with the following estimator:

$$\hat{\boldsymbol{\alpha}} = \{\mathbf{A}^T \mathbf{A} + \mu \mathbf{L}^T \mathbf{L}\}^{-1} \{\mathbf{A}^T \mathbf{b}\}. \quad (6.8)$$

where $\hat{\boldsymbol{\alpha}}$ represents the parameter vector under estimation (amplitudes of PCs), \mathbf{A} is the linear operator matrix that contains the PCs in its columns, \mathbf{b} is the observed ground-satellite hybrid data set, μ is the regularization parameter and \mathbf{L} is the regularization matrix.

We chose a regularized scheme because the data vector \mathbf{b} is sparse in time and space. This sparsity depends on the length of the time window considered in the analysis. Focusing on the establishment of a new technique, we decided to follow a conservative approach and use a time window of 70 days, which is approximately the period needed by the Swarm satellites to cover all local times. Smaller windows could be used, but this would affect the level of confidence of the results due to reduced data availability. This means that each solved inverse problem contains data from 70 days. A running window approach is used, so the window moves by one consecutive day.

Even when a time window of 70 days is used, data gaps can occur and lead to an ill-posed inverse problem, depending on the available data set. To overcome possible instabilities, our regularized solution incorporates a priori information about the desired solution (Hansen, 2010). This bias is introduced in the problem by the regularization matrix \mathbf{L} , which is a diagonal matrix containing the inverse of the PCA eigenvalues squared-root (following Equations 17-19 of Alken et al., 2017). In other words, we assign more weight to the PCs that explain more of the data variance when modelling the EEJ. The degree of this forcing is then controlled by the μ parameter, defined after examining the predicted data and residuals to the actual observations, an approach analogous to the L-curve logarithmic plot (Hansen, 2010). Thus, we benefit once again from the PCA technique as it provides a priori

information to constrain the inverse problem well.

In addition, when performing the fit of Equation 6.8, we gave more weight to the data that comes from satellite than those that comes from ground. This is done to avoid possible bias arising from the data type in the inversion. On average, the ground data contributes to about 10% to 20% of the 432 data bins. Although it covers less than half of the total number of bins, the ground data provides a very large number of samples for the fitting, as it is always measuring at the same longitude. This unbalanced distribution between ground and satellite data can be seen in Figure 6.5, which shows the number of samples within each grid bin for different epochs of 2017: March (a), June (b), September (c) and December (d). In all panels, it is possible to identify 5 longitudinal sectors with constantly high number of samples (vertical yellow structures) that are caused by the presence of ground data. Thus, we weight the data sets according to their percentage of bin filling related to the total 432 bins.

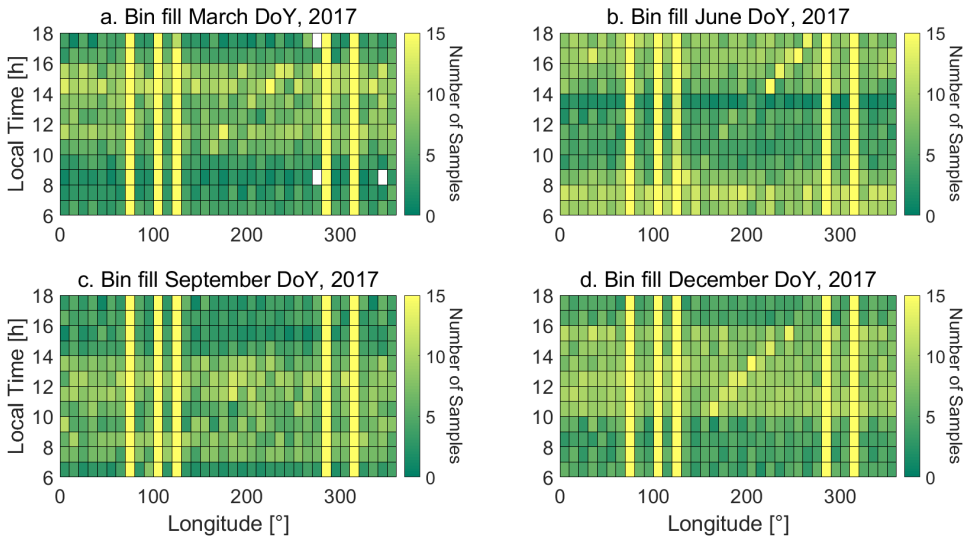


Figure 6.5: Longitude versus local time grid with color indicating the number of samples within each bin for different epochs of 2017: March (a), June (b), September (c) and December (d).

Our final PCEEJ model is available as a data publication (Soares et al., 2022) in GFZ Data Services, where its 10 PCA basis functions and its final model values are provided.

6.3 INVERTING EEJ FOR TIDES AMPLITUDES

We fitted Equation 4.2 to the PCEEJ model in order to determine the time series of solar tides amplitudes that explain the EEJ variation. The tidal modes considered for the fit are those with zonal wavenumber s ranging from -6 to +6 and period n

of 24, 12, 8 and 6 hours (see Equation 4.2). The fit is done in a least-squares sense and the parameters estimator is given by Equation 6.9:

$$\mathbf{p} = \{\mathbf{M}^T \mathbf{M} + \mu_{RR} \mathbf{I}\}^{-1} \{\mathbf{M}^T \tilde{\mathbf{b}}\}, \quad (6.9)$$

where \mathbf{p} is the model parameter containing the tides amplitude and phase information (here, we are interested only in the amplitude parameter), \mathbf{M} is the linear operator containing the trigonometric functions that describe the tidal components propagation (Equation 4.2), $\tilde{\mathbf{b}}$ is the EEJ modeled by PCEEJ, $\mu_{RR} \mathbf{I}$ is a ridge-regression regularization term added to the problem formulation to yield more stable parameters inversion. The ridge-regression regularization term adds a priori information that forces the solution to tend to zero, which in practice just attenuates abnormally large unstable values of solution.

6.4 EEJM-2 MODEL SETTINGS

The EEJM-2 model data was obtained by running the model for each DoY within the years from 2003 until 2018, with a longitude spacing of 1° , local time varying with 1 hour, lunar time calculated based on the solar time and the EUVAC parameter calculated based on daily F10.7 index data (Alken and Maus, 2007). To allow a direct comparison with the observed and the PCEEJ data, the EEJM-2 data was averaged according to the 70-day time window.

6.5 COMPARISON WITH SABER TEMPERATURE DATA

Equation 4.2 was used to fit the SABER temperature data and retrieve solar tides amplitudes, analogously as was done for the geomagnetic EEJ data. Prior to inversion, SABER data pre-processing included the selection of data within the altitude interval from 100 km to 110 km and the geographic latitude interval from -45° to $+45^\circ$. Data points with abnormal values were also discarded. As SABER provides very good spatio-temporal coverage compared to the EEJ data, PCA modeling was not necessary. The parameter estimation from Equation 6.9 was applied for SABER data inversion. Like in the EEJ data analysis, time windows of 70 days were used when performing the fit.

While comparing inversion results obtained from EEJ and temperature data, an emphasis is given to non-migrating tides. This is because migrating tides in the EEJ are mostly due to direct solar radiation effects on the ionospheric conductivity, rather than by migrating tides in the neutral atmosphere. Even if there is no tidal

forcing from the neutral atmosphere, the ionospheric conductivity is high during day and low during night, which would lead to migrating tidal components in the EEJ. On the other hand, non-migrating tidal components of the EEJ are strongly affected by non-migrating tides in the neutral atmosphere (Lühr and Manoj, 2013).

6.6 WORKFLOW FOR RETRIEVING IMPORTANT TIDAL MODES

To summarize, Figure 6.6 shows a flowchart with the proposed workflow for obtaining the PCEEJ model and retrieving the tidal modes that play an important role in the EEJ variability.

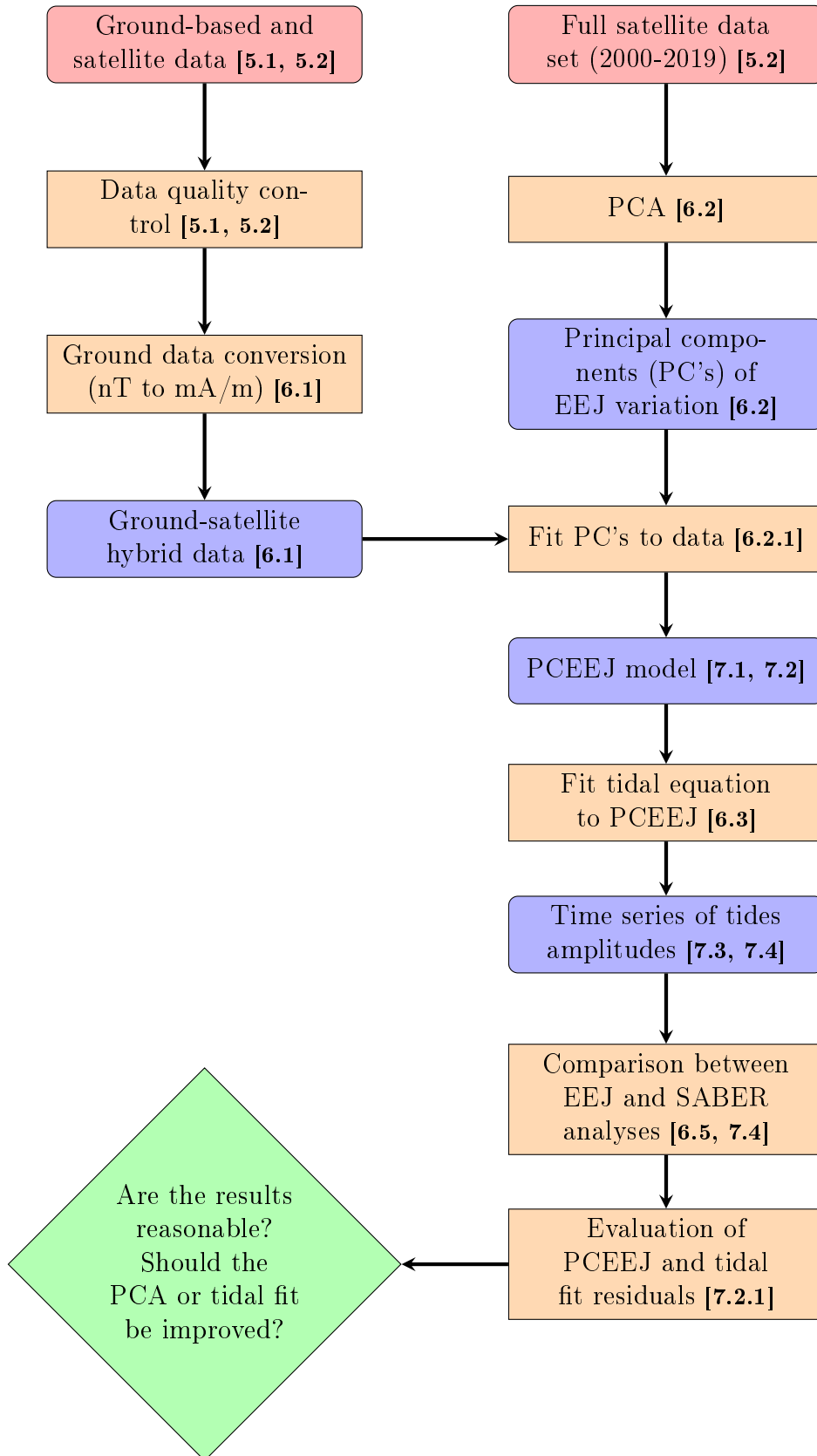


Figure 6.6: Flowchart with the proposed workflow to retrieve the tidal modes that are important in the EEJ short-term variability. The corresponding sections or subsections of the Part II text are shown in bold, between brackets.

CHAPTER 7

RESULTS AND DISCUSSION

7.1 OBSERVED EEJ, PCEEJ, EEJM-2 AND RE-CONSTRUCTION WITH TIDES

Figure 7.1 shows a comparison between the observed EEJ, PCEEJ model, EEJM-2 model and EEJ reconstructed with tides data for the 70-day time window centered at the 15th day from March, June, September and December months from the year of 2017.

The observed EEJ data shown in Figure 7.1 (a, b, c and d) was obtained by calculating the median of the samples found within each bin of the grid. The EEJ spatio-temporal variation and its seasonal variation shown for the observed data is in agreement to the expected average pattern, as the occurrence of the prominent wave-4 longitudinal structure around September (Lühr and Manoj, 2013). For the 2017 period, a very high percentage of the total number of data grid bins is filled. For instance, in Figure 7.1, the occurrence of data gaps can only be identified around March (panel a), which shows 99% of bin filling with only 3 white-coloured bins related to data gaps. However, for other years this percentage can go under 70%. This occurs due to the different data sets available for data analysis but also due to differences in satellite mission sampling. In the case of the Swarm era, the constellation is sampling at very similar local times during the beginning of the mission. But then, in 2017/2018, the Swarm satellites start to sample 6 hours apart, maximizing the spatio-temporal coverage, increasing the available information for PC fit and reducing drastically the occurrence of data gaps. Thus, we take advantage of this convenient property of the Swarm mission and use the period from 2017/2018 as a benchmark since it provides the best data coverage from our data set.

The PCEEJ (panels e, f, g and h) was obtained by the approach described in section 6.2.1. The model results are in agreement with those from the observed data in terms of amplitude and in terms of spatio-temporal behavior for the DoYs shown

as examples. As expected, the PCEEJ model provides dense EEJ intensities that smoothly change with longitude and local time without the noise-like fluctuations seen in the observations.

By comparing the PCEEJ with the EEJM-2 results (panels i, j, k and l), we see that the overall long-wavelength features are in agreement. For the examples shown in Figure 7.1, there are minor differences between PCEEJ and EEJM-2 that can be related on how well each model can explain the observations in time and space.

The EEJ reconstructed as the sum of the tidal components with s from -6 to 6 and n from 1 to 6 are shown in Figure 7.1 (panels m, n, o and p). These results were derived through the inversion process described in section 6.3. If the tidal amplitudes are properly captured and the inversion scheme is robust, the reconstructed EEJ should reproduce to a good extent the input from the PCEEJ model. Indeed, this is noted when comparing the panels from the second and fourth rows of Figure 7.1.

For completeness, Figures 7.2 and 7.3 show the comparison between the observed EEJ, PCEEJ model, EEJM-2 model and EEJ reconstructed with tides data for the years 2018 and 2016, respectively. A consistent EEJ climatology can be observed from year-to-year, for all data sets, when comparing Figures 7.1, 7.2 and 7.3. The results obtained for PCEEJ, EEJM-2 and EEJ reconstruction data for 2017 are comparable to those obtained for 2018 and 2016. Again, there is an overall agreement between PCEEJ and EEJM-2 long-wavelength features and some differences in the shorter wavelength scale.

It is interesting to note that, like 2017, the 2018 observed data indicate a very good data coverage with few data gaps. However, 2016 observed data shows an increase in the data gaps due to the more redundant Swarm satellites coverage. The PCEEJ model is robust enough to deal with such increase in data gaps, as it preserves the well-known EEJ features without creating any artifact or imprint from the data gaps.

In addition, it is possible to identify year-to-year EEJ amplitude changes in the observed and modeled EEJ due to solar activity changes. The 2018 amplitudes are smaller when compared to 2017, while the 2016 amplitudes are the largest.

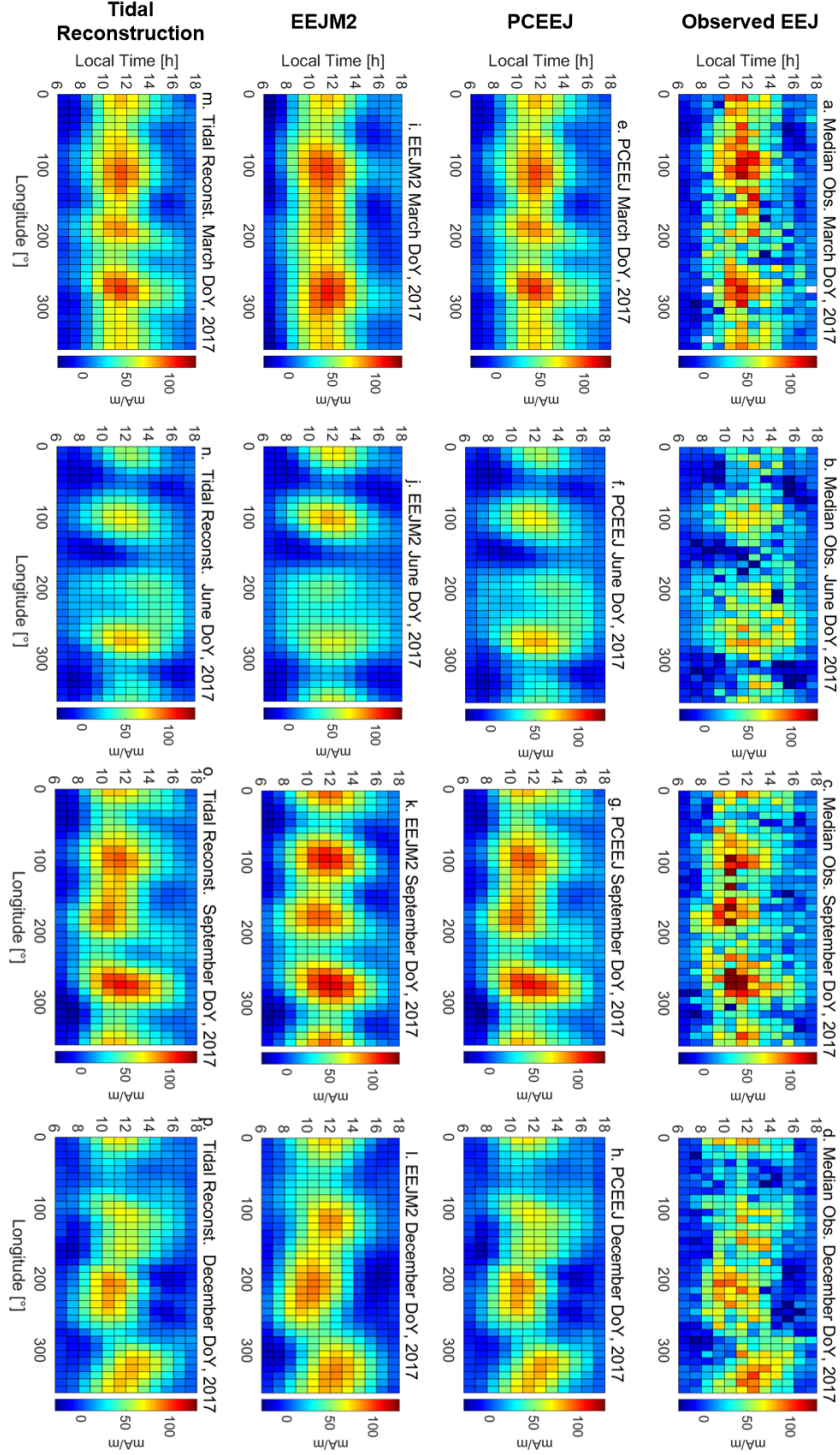


Figure 7.1: Observed EEJ data shown as median value per bin for 70 days centered on March (a), June (b), September (c) and December (d) 2017. Displays from the same selected days of 2017 are shown for the PCEEJ model (e, f, g and h), EEJM-2 (i, j, k and l) and the EEJ data reconstructed as the sum of tidal modes with $|s| \leq 6$ and $n=1-6$ (panels m, n, o and p). The figure is rotated by 90 degrees to facilitate its visualization.

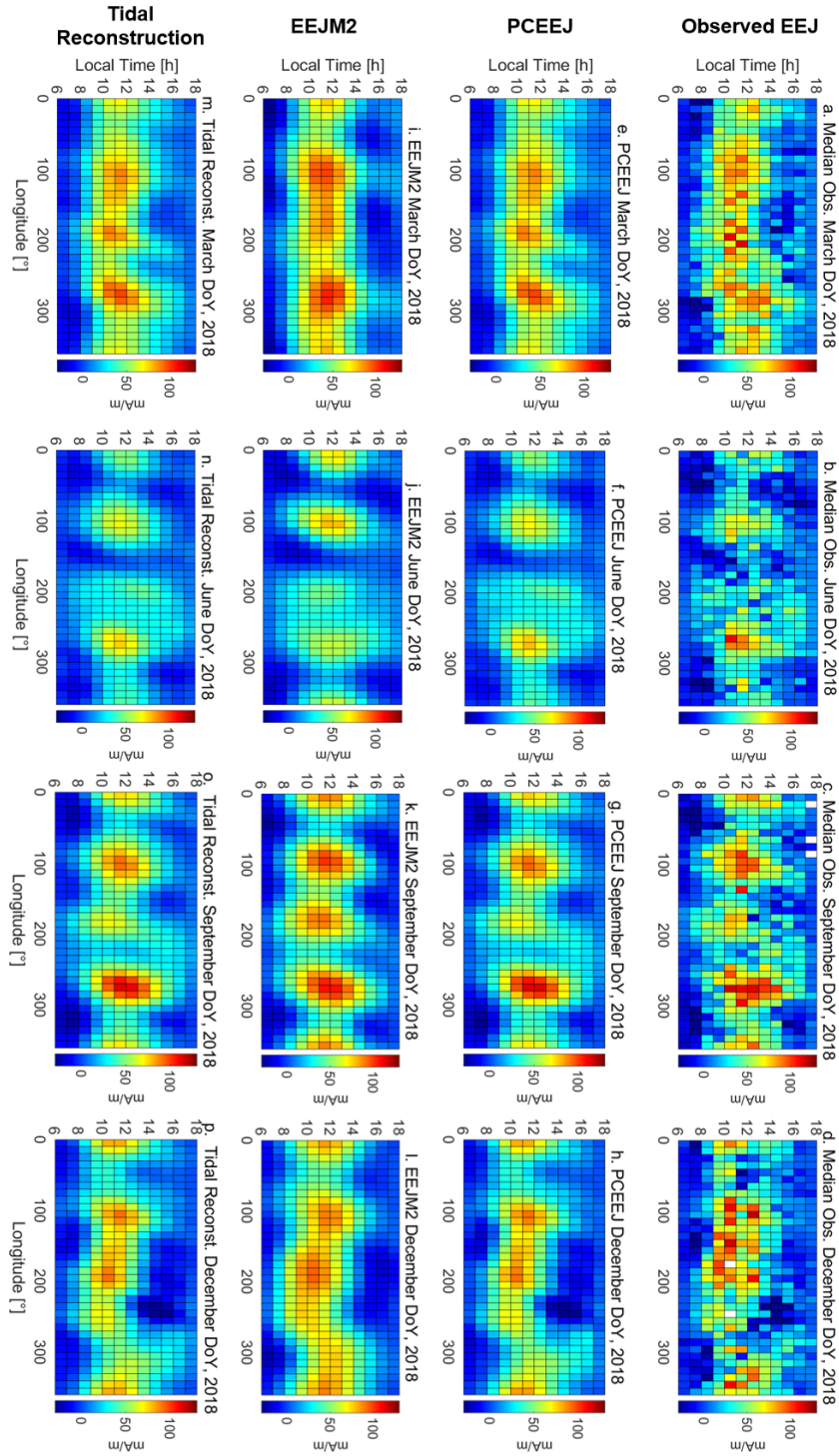


Figure 7.2: The same as Figure 7.1, but for 2018.

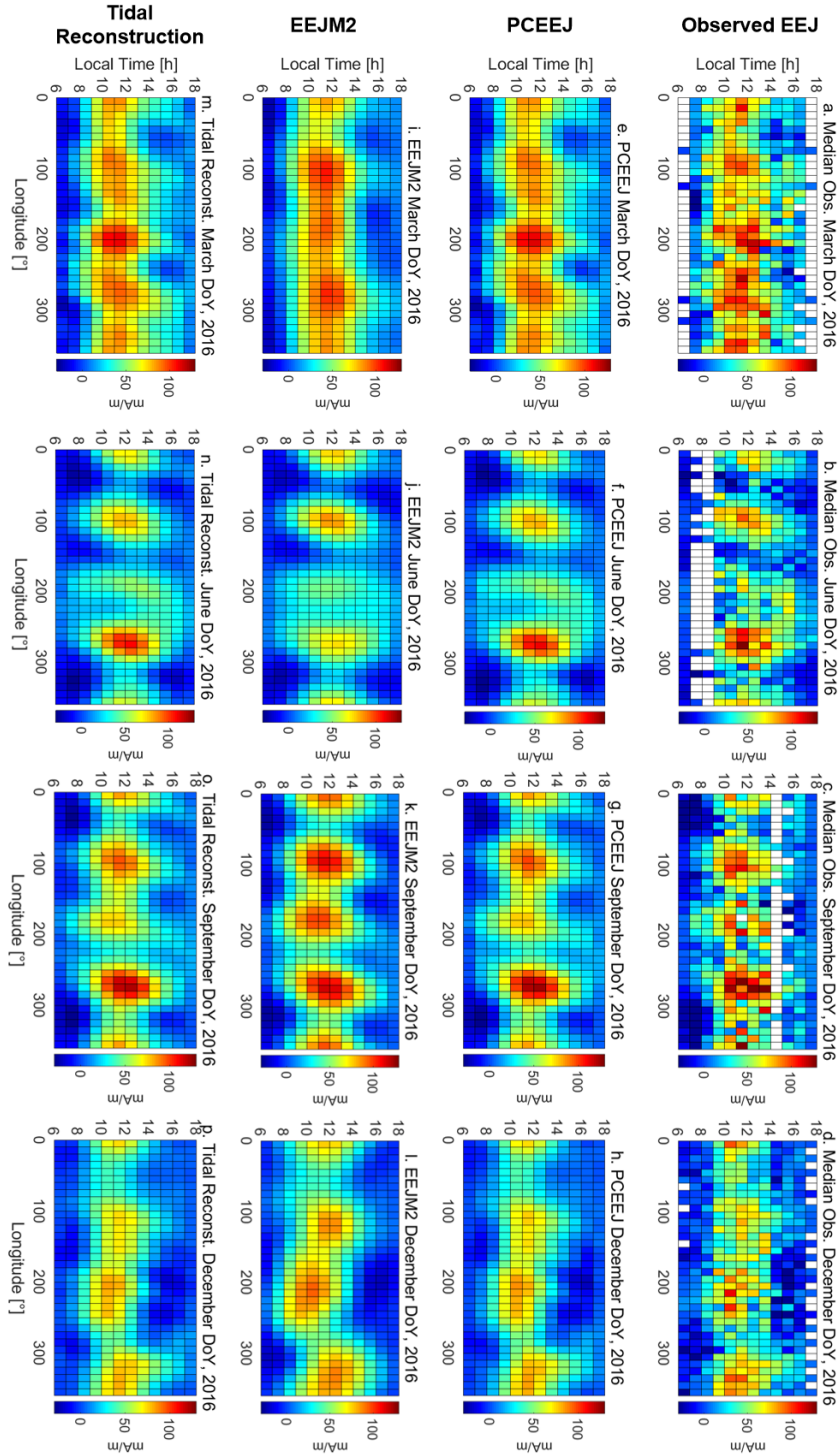


Figure 7.3: The same as Figure 7.1, but for 2016.

7.2 PCEEJ vs EEJM-2

7.2.1 MATCH TO OBSERVED DATA

An important part of assessing the accuracy of the proposed PCA modeling scheme relies on the comparison with the EEJM-2 model. Figure 7.4a shows the distribution of the residuals of the modeled EEJ to the observed data for 2015 (PCEEJ model in red and EEJM-2 in blue). Here, all 432 grid bins from each of the 365 fits per year are considered. The low values of residuals mean and median indicate that both EEJM-2 and PCEEJ can well represent the average EEJ. The standard deviation and the difference between mean and median (as a measure of skewness of the distribution) for the PCEEJ model are smaller. Apart from the aforementioned modelling differences, these statistical differences can also be attributed to the absence of Swarm data during the construction of EEJM-2.

Figure 7.4b is analogous to Figure 7.4a, but for the year of 2017. It shows that (i) as for 2015, the PCEEJ model represents better the observed data than EEJM-2; (ii) the PC fit for 2017 is better than for 2015, as the mean, median and standard deviation sigma values are reduced (-0.21, -0.47 and 8.60 mA/m, respectively). Meanwhile, EEJM-2 shows very similar statistical results for 2015 and 2017. The differences in the PC fit quality between 2015 and 2017 can be attributed to the improved local time coverage of the satellite data as the difference in local time sampling between the Swarm A and B that reached its maximum value of 6h around 2017(Figure 7.4c).

A yearly overview of the residuals between the models and observations is shown in Figure 7.5a. It shows the residuals standard deviation as time series from 2003 until 2018, where red squares are related to the PCEEJ model and blue squares are related to the EEJM-2 model. Each square represents the standard deviation of the residuals between model and observations for a complete year. The standard deviation values related to the PCEEJ model are consistently smaller than those related to EEJM-2. The PCEEJ standard deviation shows a decreasing trend in 2016, 2017 and 2018, with a minimum in 2018, which are years that benefit from the improved Swarm constellation local time coverage. However, the EEJM-2 model standard deviation shows a minimum in 2006 and an increasing trend for 2016, 2017 and 2018. These results indicate that the PCEEJ can indeed better represent the EEJ observations (for both CSØ and Swarm periods).

For completeness, Figure 7.5b shows the percentage of bins from our data grid that are covered through each year. As the data from each day is organized in a grid of 432 bins, each year will correspond to a total of 157680 bins to be filled (432 bins times 365 days). Figure 7.5b shows that the percentage of bins covered

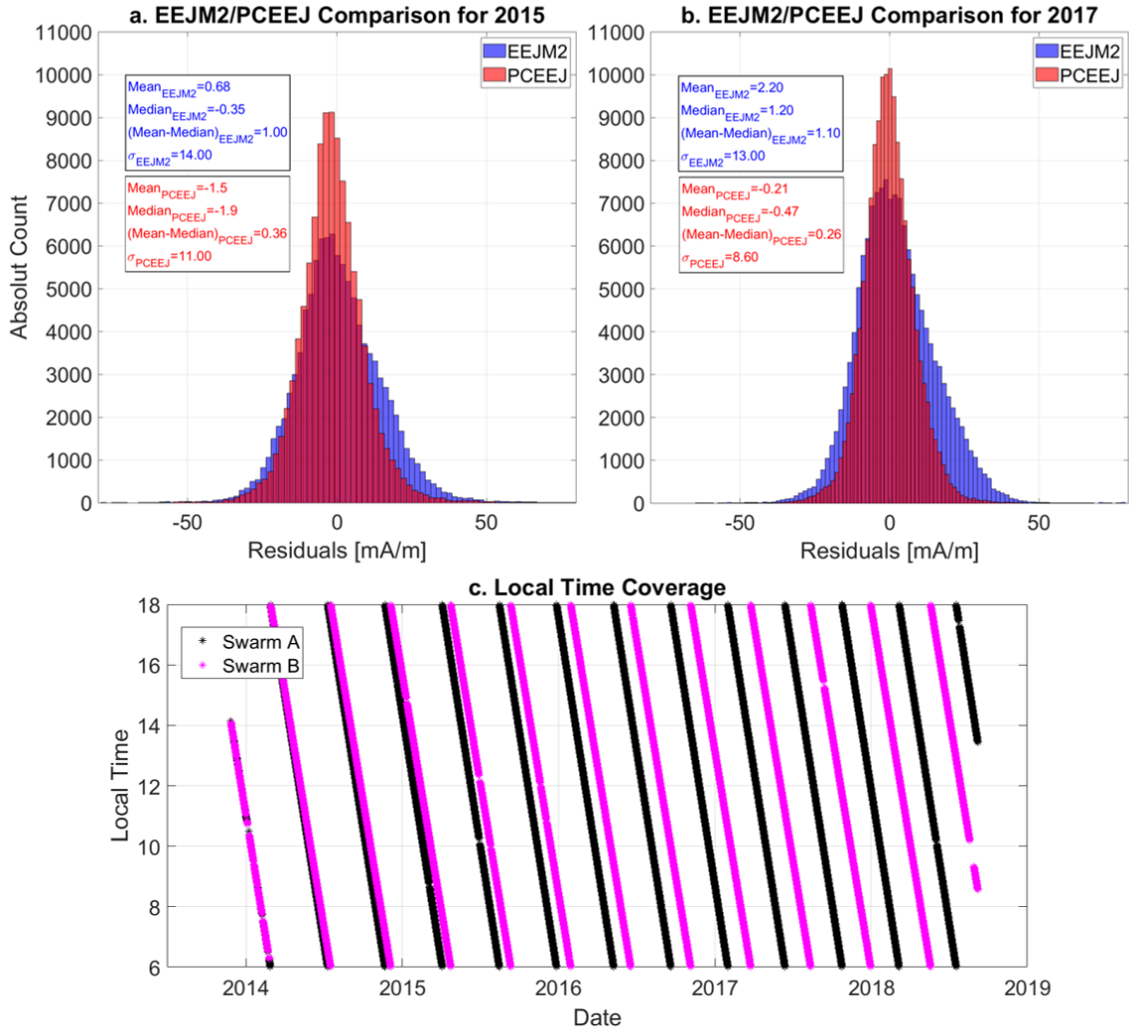


Figure 7.4: Histograms of residuals between observed data and EEJM-2 model (blue) and between observed data and PCEEJ model (red) for 2015 (a) and 2017 (b). Panel c shows the variation of the local time coverage of satellites Swarm A and B from 2013 to 2018.

during the CSØ period remains always at a similar level of around 70% (except in 2010 due to the end of the CHAMP mission). On the other hand, we observe an important increase in the percentage of covered bins during the Swarm period, going from around 70% in 2014 until nearly 100% in 2018. By comparing Figures 7.5a and 7.5b, an anticorrelation between number of covered bins and standard deviation of PCEEJ residuals is visible.

The residuals between the EEJ reconstructed by tidal fits and the PCEEJ model are also addressed in Figure 7.5c, again as time series. The yearly averages of these residuals (not shown here) are rather small, ranging between 0 and 2 mA/m. Here, in Figure 7.5c, the standard deviation of these residuals is shown, always between 1 and 3 mA/m. These results indicate that the tidal fit can reproduce the PCEEJ well throughout the years investigated in this study. Besides the small residuals, it

is important to note that the reconstructed EEJ is in agreement with the expected EEJ variation, as seen in Figure 7.1 and related discussion.

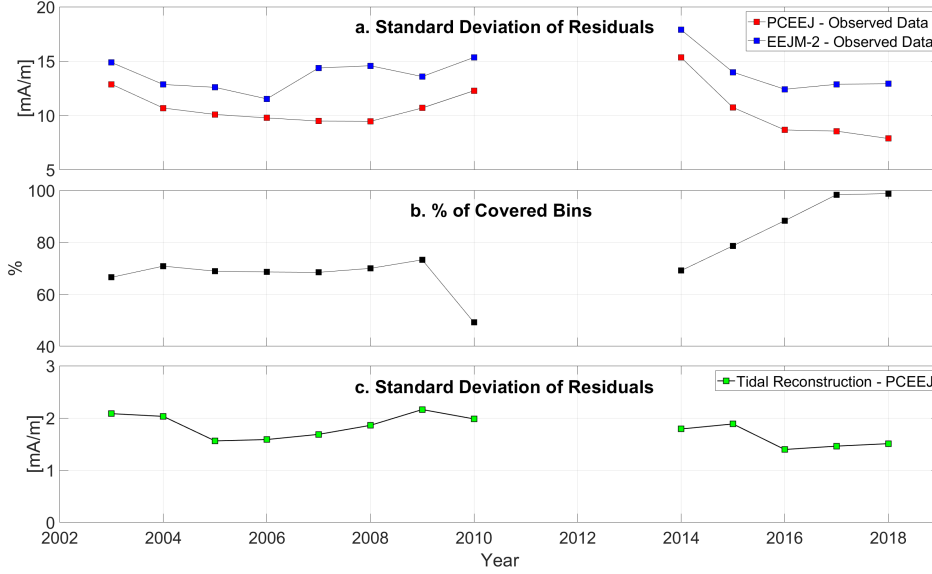


Figure 7.5: (a) Standard deviation of residuals between EEJ models (PCEEJ in red and EEJM-2 in blue) and EEJ observations, shown as time series from 2003 until 2018. (b) Percentage of data grid bins covered for each year. (c) Standard deviation of residuals between EEJ reconstructed by tidal fits and the PCEEJ model.

As an additional quality check, we calculated the correlation coefficient between the modelled EEJ (PCEEJ and EEJM-2) and the observed EEJ for each bin of our 36x12 data grid, using data from 2017. The results are shown in Figure 7.6a for PCEEJ and 7.6b for EEJM-2, respectively, with the correlation coefficient values ranging from -0.5 to +1. Figure 7.6a clearly shows higher values of correlation (towards yellow color) when compared to Figure 7.6b. Figures 7.6c and 7.6d shows a more quantitative analysis by displaying the distribution of the correlation coefficient values and their associated median value, which is greater for the PCEEJ case (0.8269) than for the EEJM-2 case (0.6768). Therefore, the PCEEJ is better correlated to the observed EEJ in space and time when compared to EEJM-2, for the benchmark of 2017.

These results confirm that a better modeling of EEJ variations can be achieved with the PCA technique proposed in this study. However, this depends on the available data set and its spatio-temporal coverage.

7.2.2 AVERAGE TIDAL COMPOSITION PER YEAR

The year-to-year variation of the average amplitude obtained for each tidal component in the EEJ is shown in Figure 7.7, given as $\log(\text{EEJ amplitude})^2$. These average amplitudes are obtained by calculating the average of the 365 values available for

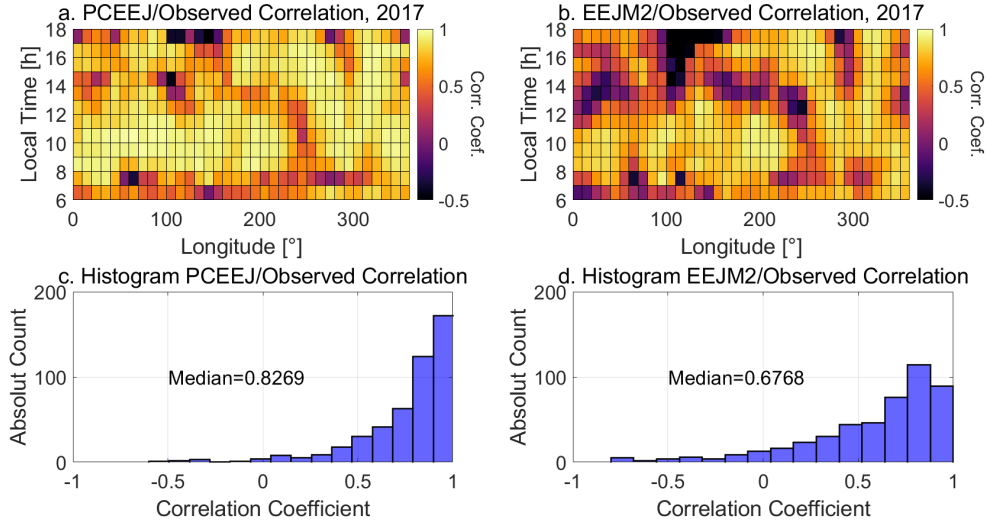


Figure 7.6: Correlation coefficient between observed data and PCEEJ model and between observed data and EEJM-2 model (a and b for distribution on grid and c and d for histogram, respectively).

each year after running the inversion based on the 70-day moving window. The year-to-year variation can be observed by comparing panels a, b, c and d, which show the PCEEJ average tidal composition for the years 2015, 2016, 2017 and 2018, respectively. For comparison purposes, the EEJM-2 average tidal composition, obtained in the same manner of the PCEEJ case, is also shown for the years 2017 and 2018 in panels e and f, respectively. Each panel in Figure 7.7 is formed by 48 bins and each bin represent a different tide, as indicated by the different combinations of period (n , x axis) and zonal wavenumber (s , y axis).

Concerning the PCEEJ results, most of the tidal amplitudes tend to decrease from 2015 to 2018, based on the color-coded label. This trend can be mainly attributed to solar cycle effects, as 2015 is closer to the solar maximum than 2018. This feature was also reported by [Lühr and Manoj \(2013\)](#), who compared the EEJ tides amplitudes from periods of solar maximum and minimum, based on two data subsets of 5-year averages (2000 to 2005 and 2005 to 2010). Here, we are directly comparing the results of independent years. The PCEEJ and EEJM-2 2017 and 2018 spectra show similar amplitude distribution for the main migrating and non-migrating tides. However, the EEJM-2 has many non-migrating tides with negligible amplitudes, as indicated by Figures 7.7e and 7.7f white colored bins with tiny logarithmic values (considered as constantly zeroed time series). The individual case of the non-migrating tide DE4 ($n=1$, $s=-4$) is discussed in section 7.4 as one example of important discrepancy between PCEEJ and EEJM-2 tidal composition.

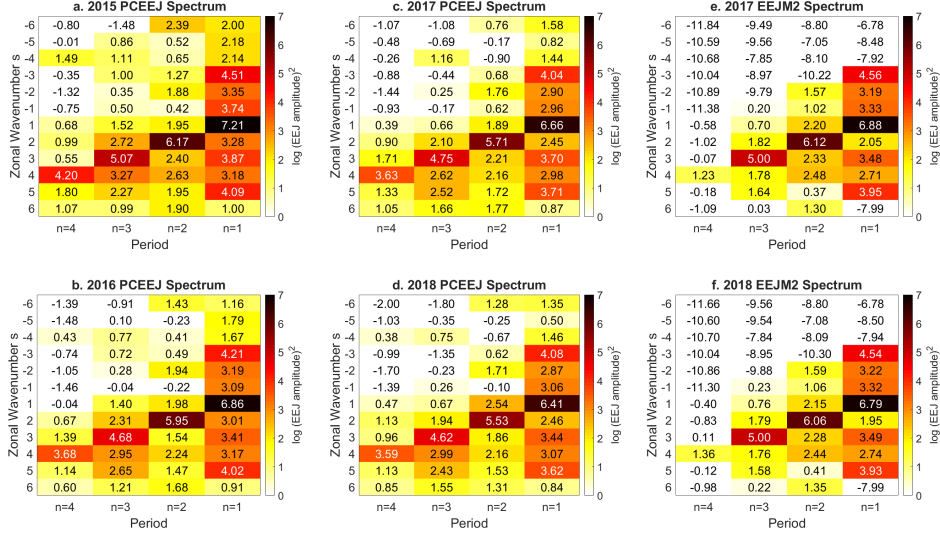


Figure 7.7: Average yearly EEJ tidal spectrum given by $\log(\text{mA/m})^2$ for each combination of n and s , during the years of 2015 (a for PCEEJ), 2016 (b for PCEEJ), 2017 (c for PCEEJ and e for EEJM-2) and 2018 (d for PCEEJ and f for EEJM-2). The color bar indicates the values of $\log(\text{EEJ amplitude})^2$ or, equivalently, $2\log(\text{EEJ amplitude})$.

7.3 MIGRATING TIDES TIME SERIES

Figures 7.8a and 7.9a show the time series obtained after EEJ inversion for the DW1 and SW2 migrating tides, respectively. Both figures show the results for the Swarm period, from 2015 until 2018, with vertical dashed black lines indicating the beginning of a new year, and the color bar in panel a showing the percentage of filled bins for each day (i.e., amount of data available for inversion). By comparing Figures 7.8a and 7.9a, DW1 shows larger amplitudes than SW2 and that both components present a similar seasonal variation with maxima at equinoxes and minima at northern hemisphere summer. These features agree very well with those reported by the average spectra derived by [Lühr and Manoj \(2013\)](#). Both DW1 and SW2 time series present a decreasing trend from 2015 to 2018, related to the solar cycle effect already seen in Figure 7.7. The other migrating tides, as TW3 and QW4 (not shown here), present similar seasonal variations with reduced amplitudes.

The panels b, c, d and e found in Figures 7.8 and 7.9 indicate the contribution of the tidal component to the EEJ in terms of positive and negative perturbations for selected days of year from March, June, September and December 2018. By Figures 7.8b, 7.8c, 7.8d and 7.8e it is possible to see that DW1 acts as the positive background. It adds some negative perturbation in early morning or late afternoon periods. On the other hand, a semi-diurnal pattern can be seen as negative and positive perturbations from the SW2 tide in Figures 7.9b, 7.9c, 7.9d and 7.9e. No

longitudinal variation is observed for both DW1 and SW2 EEJ perturbations because these are migrating tides, which by definition do not depend on longitude.

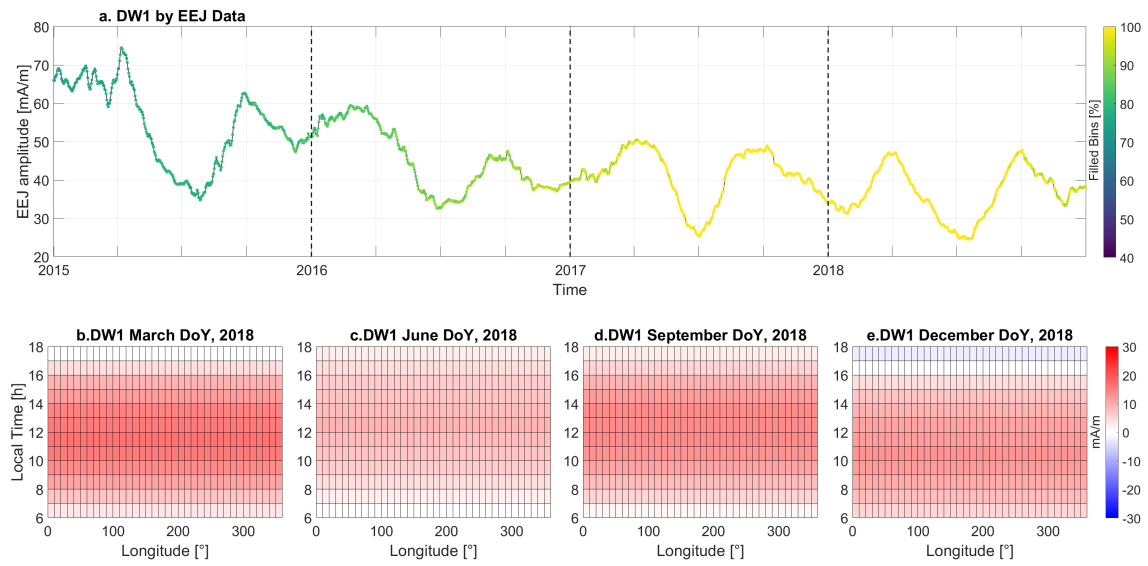


Figure 7.8: (a) Time series of DW1 amplitude obtained from EEJ data during the Swarm period (x axis represent time with the years as labels). Vertical dashed black lines indicate the beginning of a new year. Panels b, c, d and e indicate the contribution of DW1 to the final predicted EEJ in terms of positive and negative perturbations for selected days of year from March, June, September and December 2018, respectively.

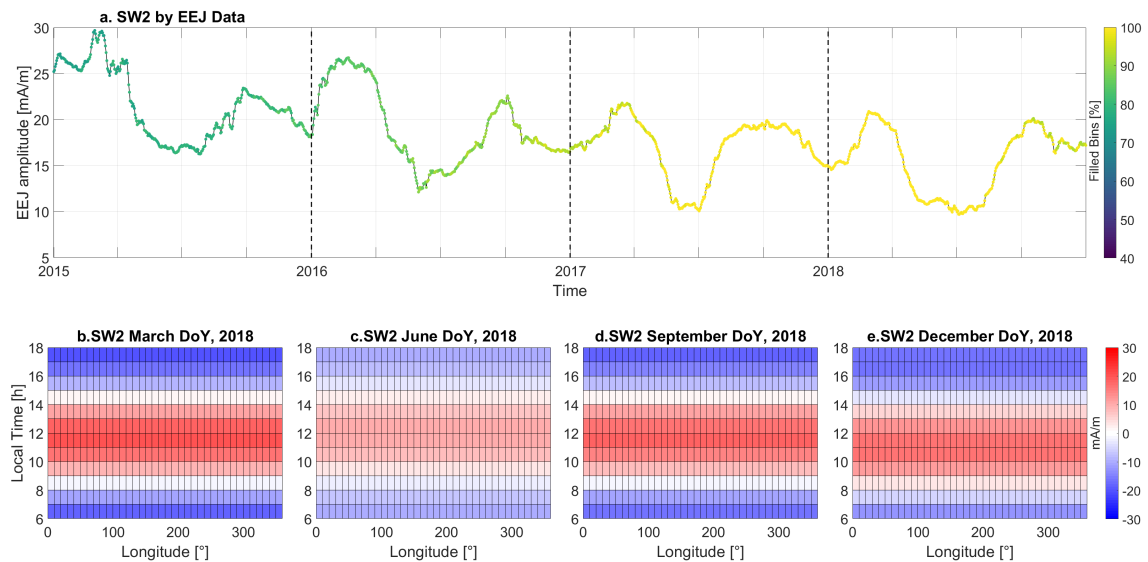


Figure 7.9: The same as Figure 7.8, but for SW2 tide.

7.4 NON-MIGRATING TIDES TIME SERIES

In this section, the time series of selected non-migrating tides obtained after inversion of EEJ geomagnetic data will be presented, discussed and compared to analogous time series obtained after inversion of SABER temperature data. First, examples from the Swarm period will be shown for DE3, DE2, DE4, SW4 and TW1 tides. Then, the results from the CSØ period will also be shown for DE3 and SW4 tides.

Figure 7.10 shows the results for the DE3 tide obtained for the Swarm period, known as one of the most important non-migrating components. With large amplitude and being the primary cause of the so-called wave-4 longitudinal structure in the ionosphere, the DE3 signal has been investigated in a variety of different data sets and studies (England et al., 2006; Kil et al., 2007; Lühr et al., 2008; Singh et al., 2018). Figure 7.10a shows the DE3 time series obtained from EEJ data. Figure 7.10b shows the spatio-temporal variation of DE3 amplitude obtained from SABER temperature data. Vertical dashed lines indicate the beginning of a new year, in black for Figure 7.10a, and in white for Figure 7.10b. A comparison of Figures 7.10a and 7.10b indicates a remarkable correlation between EEJ and temperature data analyses for DE3. In both analyses, the DE3 signal peaks around August, a behavior that is in agreement with previous studies based on EEJ data (Lühr and Manoj, 2013) and on SABER temperature data (Forbes et al., 2008). As in the case of the migrating tides, the DE3 amplitude of the EEJ shows some dependency on solar activity, i.e., the amplitude shows a decreasing trend from the year 2015 to 2018. This trend is not seen in the DE3 amplitude of the SABER temperature. Studies found little solar-activity effect on upward-propagating tides from the lower atmosphere (e.g., Oberheide et al., 2009). Figures 7.10c, 7.10d, 7.10e and 7.10f are the perturbations caused by the DE3 tide to the final EEJ reconstructed by tides during days from March, June, September and December 2018, that indicate a clear wave-4 longitudinal structure.

Figure 7.11 shows the results for the DE2 non-migrating tide time series during the Swarm period. EEJ and temperature data analyses are in very good agreement, indicating two peaks per year: one around June solstice and other around December solstice. This behavior is consistent with the average DE2 pattern by Lühr and Manoj (2013). In our analysis, further sub-year temporal variations are revealed due to the use of the 70-day analysis window. The DE2 perturbation displays in panels c, d, e and f indicate the wave-3 longitudinal structure.

Figure 7.12 shows the results for the DE4 non-migrating tide time series during the Swarm period. Although the DE4 amplitudes are weaker than those from DE3 and DE2, its signatures in the EEJ and temperature data are also in good agreement, with two equinoctial peaks per year (Figures 7.12a and 7.12b). This behavior is

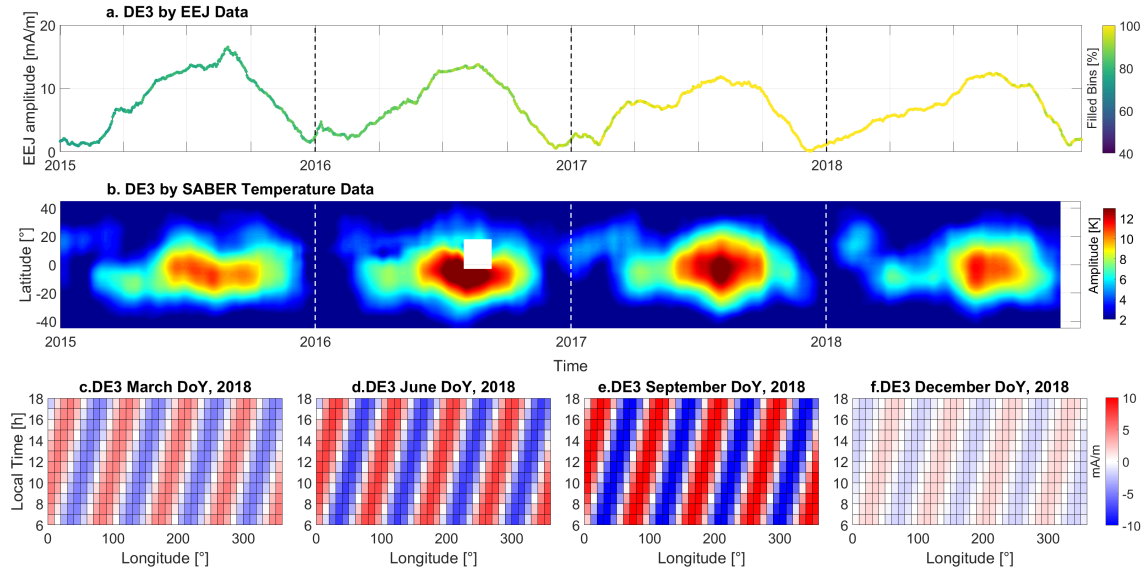


Figure 7.10: Time series of DE3 amplitude obtained from EEJ data (a) and from SABER temperature data (b) during the Swarm period (x axis represent time with the years as labels). SABER temperature observations range from 100 km to 110 km. Vertical dashed lines indicate the beginning of a new year. Panels c, d, e and f indicate the contribution of DE3 to the final predicted EEJ in terms of positive and negative perturbations for selected days of year from March, June, September and December 2018, respectively.

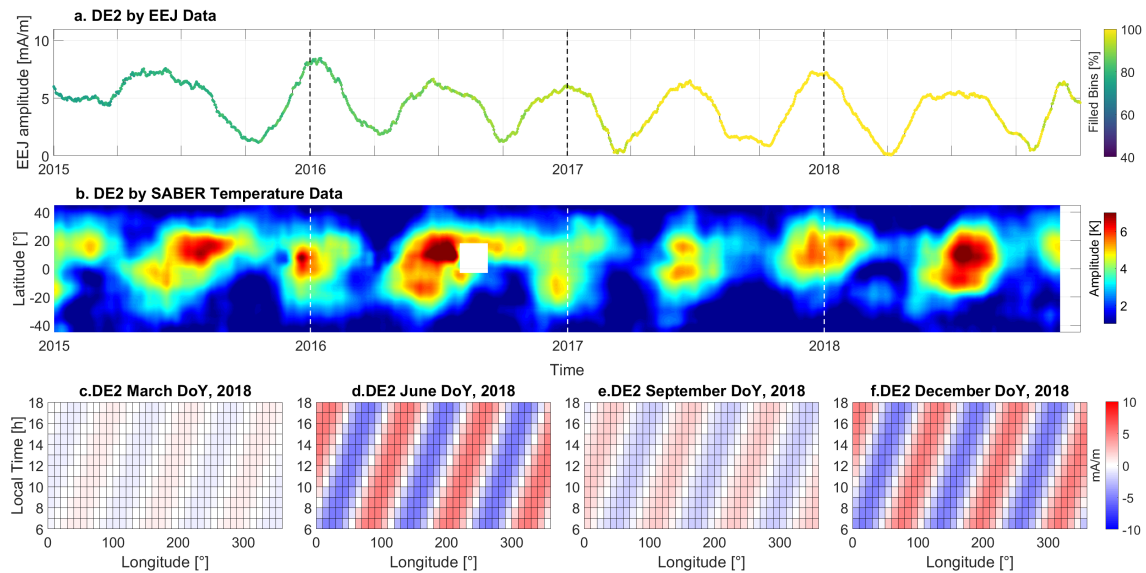


Figure 7.11: The same as Figure 7.10, but for DE2 tide.

consistent with the average DE4 pattern by [Lühr and Manoj \(2013\)](#). The DE4 is one example of tide which has significant amplitudes in PCEEJ data and negligible tiny amplitudes in EEJM-2 data, as seen in Figure 7.7. The PCEEJ DE4 amplitudes and its good match to the temperature data suggests that the model is able to represent realistically even those non-migrating tides with smaller amplitudes. The

DE4 perturbation displays in panels c, d, e and f indicate a wave-5 longitudinal structure.

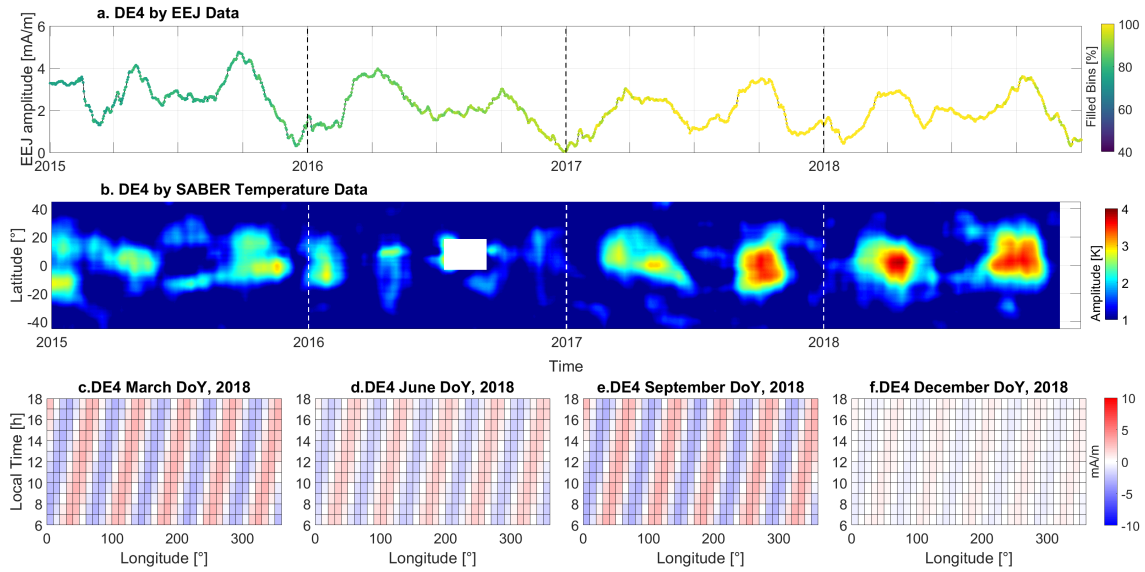


Figure 7.12: The same as Figure 7.10, but for DE4 tide.

Figure 7.13 shows another example of good correlation between EEJ and temperature tides, but now for the SW4 non-migrating tide during the Swarm period. Both Figures 7.13a and 7.13b indicate a major peak around December, which is in agreement with the average SW4 pattern obtained by Lühr and Manoj (2013). In our analysis, some year-to-year variation in SW4 can be observed, which cannot be attributed solely to solar activity, e.g., the high values observed for December 2017 near solar minimum. It is known that the SW4 tide is generated by the nonlinear interaction between the stationary planetary wave SPW2 and the migrating semidiurnal tide SW2 (Forbes et al., 2008; Teitelbaum and Vial, 1991). This means that the year-to-year variation of SW4 may be contributed by other mechanisms than solar activity. Planetary or Rossby waves are mainly caused by airflow over large-scale topographic features (Holton, 2004). If the planetary waves amplitude is large enough in the ionospheric dynamo region, they will affect current systems such as the EEJ. The relative contribution of planetary wave activity and solar activity to the year-to-year variation of SW4 needs more investigation. The SW4 perturbation displays in panels c, d, e and f indicates its wave-2 longitudinal structure.

So far, we have presented examples with very good agreement between the results obtained from EEJ and temperature data analyses. One fact in common between DE3, DE2, DE4 and SW4 is that these are tides with relatively strong signal and/or a simple spatio-temporal distribution. Other components, however, present small amplitudes and/or more complex temporal variation without a clear seasonal pattern, making it difficult to compare EEJ and SABER temperature results. The

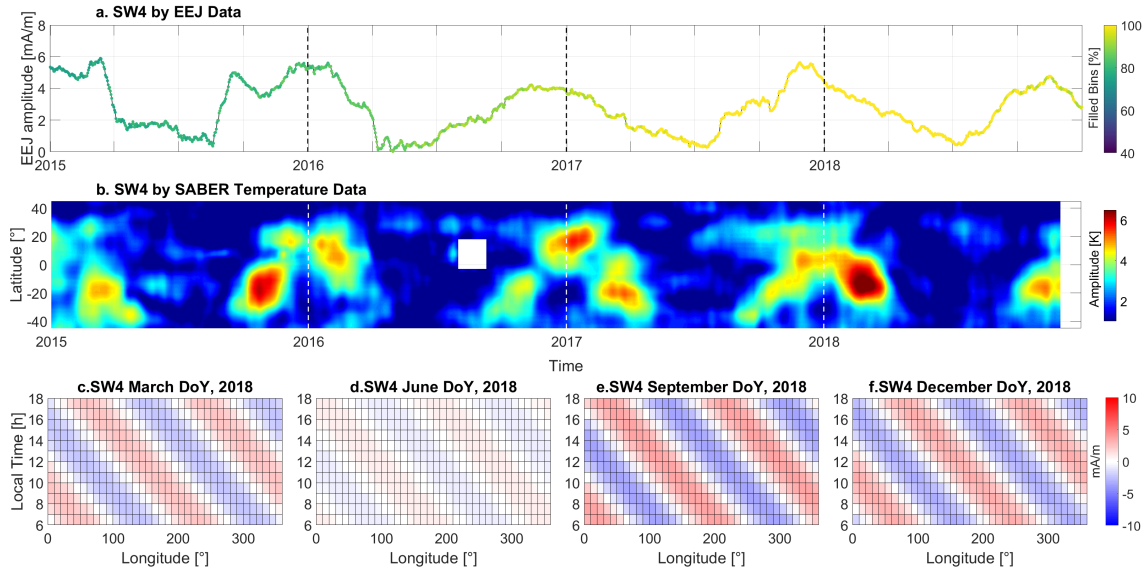


Figure 7.13: The same as Figure 7.10, but for SW4 tide.

TW1 non-migrating tide in Figure 7.14 is one of these examples. The comparison between the time series obtained with EEJ and temperature data sets, does not indicate a very clear correlation as seen for DE3, DE2, DE4 and SW4. In this case, the spatio-temporal variation of the TW1 amplitude in the SABER analysis is more heterogeneous, and the agreement with the temporal variation of the TW1 amplitude in the EEJ is limited. Although there is no striking correlation between EEJ and SABER temperature results for TW1, it is important to note that the seasonal variation of the TW1 amplitude in the EEJ shown in Figure 7.14a is in very good agreement with the seasonal variation presented in Lühr and Manoj (2013), with a peak around June solstice. The TW1 perturbation displays in panels c, d, e and f indicate the wave-2 longitudinal structure.

Figures 7.15 and 7.16 show results for the non-migrating tides DE3 and SW4 for the CSØ period, respectively. The amplitudes are comparable with those obtained for the Swarm period (Figures 7.10 and 7.13). Again, there is a good match between the time series of the amplitudes derived from EEJ and SABER temperature data. For example, the amplitude of the DE3 in both EEJ and SABER temperature shows an annual variation with the maximum in August-September. Both EEJ and SABER temperature DE3 amplitudes show relatively short-term variations with a local maximum in December, especially in the years 2007 and 2008. The significant decrease in the amount of filled bins in 2010, represented by the panel a color bar, is due to the end of the CHAMP satellite mission. As shown and discussed for the Swarm period, the amplitudes of DE3 and SW4 do not show strong dependence on solar cycle activity.

The tides signatures obtained from SABER and EEJ analyses show an obvious

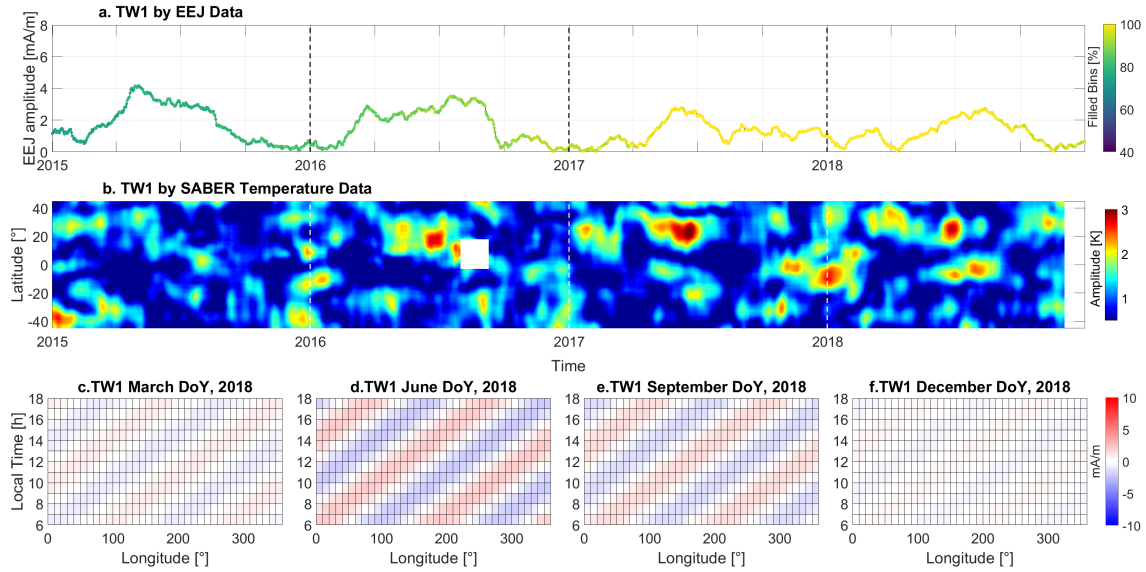


Figure 7.14: The same as Figure 7.10, but for TW1 tide.

correlation, but they result from different processes. In SABER analysis, the obtained tides signatures demonstrate the tides themselves in the atmosphere. In EEJ analysis, the obtained tides signatures represent a secondary effect, namely the influence of the tides in the ionosphere.

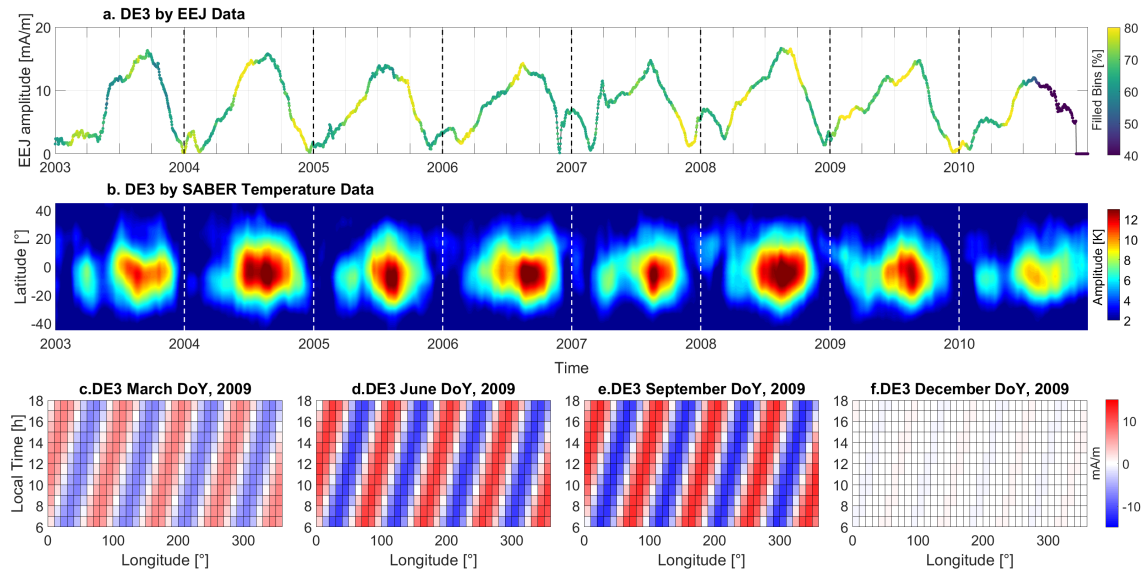


Figure 7.15: Time series of DE3 amplitude obtained from EEJ data (a) and from SABER temperature data (b) during the CSØ period (x axis represent time with the years as labels). SABER temperature observations range from 100 km to 110 km. Vertical dashed lines indicate the beginning of a new year. Panels c, d, e and f indicate the contribution of DE3 to the final predicted EEJ in terms of positive and negative perturbations for selected days of year from March, June, September and December 2009, respectively.

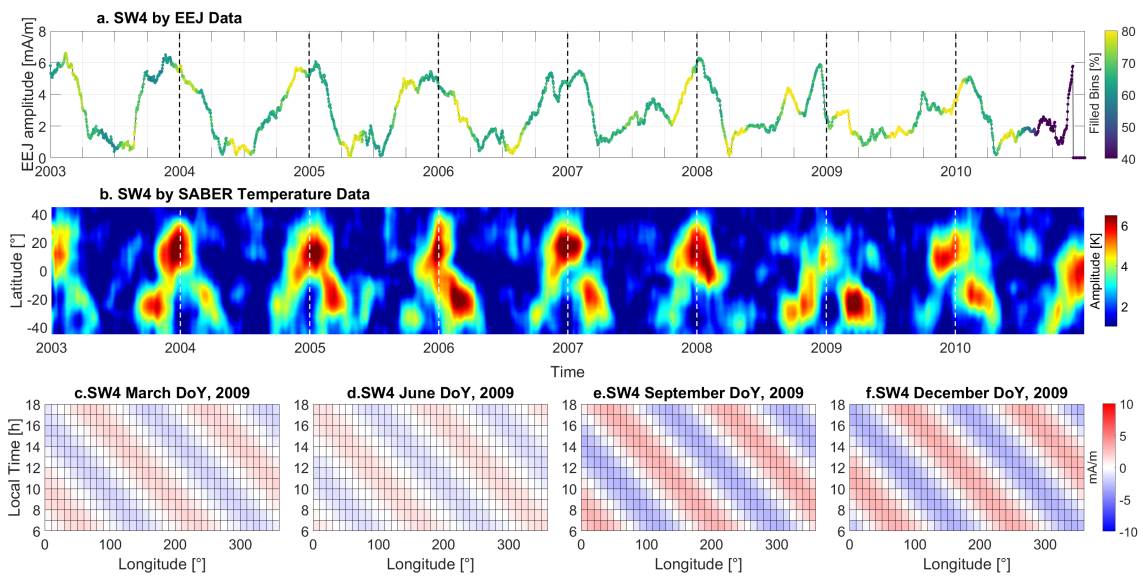


Figure 7.16: The same as Figure 19, but for 7.15 tide.

CHAPTER 8

CONCLUSIONS

A novel technique to model the intensity of the equatorial electrojet (EEJ) is proposed. The method involves principal component analysis (PCA) of EEJ intensities observed by Swarm, CHAMP and Ørsted satellites from 2000 to 2019, and fitting of the obtained principal components (PCs) to hybrid ground-satellite data over a given period of 70 days. Our statistical analysis shows that the new EEJ model can reproduce observations better than the climatological model EEJM-2. This is because the EEJM-2 was designed to represent primarily the EEJ climatology, while our PCEEJ model was designed to reproduce the EEJ for a specific period of individual years. In contrast, the performance of the PCEEJ depends on the local-time and longitudinal coverage of the EEJ data from satellites and ground stations.

The PCEEJ is used to examine tidal signatures in the EEJ, and their relations to tides in atmospheric temperature as observed by TIMED/SABER. On average, the tidal composition of the EEJ derived from our new model is consistent with the 5-year climatology presented by [Lühr and Manoj \(2013\)](#). Our method can provide the amplitude time series of various tidal modes in the EEJ for individual years. It is found that seasonal variations of major non-migrating tidal modes such as DE3, DE2, and SW4 are consistent with those in SABER temperature. Due to its construction aspects, the PCEEJ can provide realistic EEJ tidal composition and corresponding temporal variation, even for those components with reduced amplitude, as seen for the DE4 and TW1 examples. Thus, our model can be used to monitor the ionospheric effect of non-migrating tides that propagate from the middle atmosphere. In addition, the EEJ tidal composition derived from the PCEEJ model can be used as a more realistic atmospheric tidal variation input for other models, such as the first-principles model TIEGCM.

The present study used a 70-day time window for PCA modeling of the EEJ. The application of a shorter time window, down to time scales as short as days, would be possible if more EEJ data with a suitable spatio-temporal distribution is available.

Part III

EVOLUTION OF THE GEOMAGNETIC DAILY VARIATION AT TATUOCA, BRAZIL, FROM 1957 TO 2019

Part III was published in the Journal of Geophysical Research – Space Physics.

CHAPTER 9

SUMMARY AND INTRODUCTION

9.1 SUMMARY

The magnetic equator in the Brazilian region has moved over 1100 km northwards since 1957, passing the geomagnetic observatory Tatuoca (TTB), in northern Brazil, around 2013. We recovered and processed TTB hourly mean values of the geomagnetic field horizontal (H) component from 1957 until 2019, allowing the investigation of long-term changes in the daily variation due to the influence of secular variation, solar activity, season and lunar phase. The H day-to-day variability and the occurrence of the counter electrojet at TTB were also investigated. Until the 1990s, ionospheric solar quiet currents dominated the quiet-time daily variation at TTB. After 2000, the magnitude of the daily variation became appreciably greater due to the equatorial electrojet (EEJ) contribution. The H seasonal and day-to-day variability increased as the magnetic equator approached, but their amplitudes normalized to the average daily variation remained at similar levels. Meanwhile, the amplitude of the lunar variation, normalized in the same way, increased from 5% to 12%. Within the EEJ region, the occurrence rate of the morning counter electrojet (MCEJ) increased with proximity to the magnetic equator, while the afternoon counter electrojet (ACEJ) did not. EEJ currents derived from CHAMP and Swarm satellite data revealed that the MCEJ rate varies with magnetic latitude within the EEJ region while the ACEJ rate is largely constant. Simulations with the Thermosphere-Ionosphere-Electrodynamics General Circulation Model based on different geomagnetic main field configurations suggest that long-term changes in the geomagnetic daily variation at TTB can be attributed to the main field secular variation.

9.2 EVOLUTION OF THE GEOMAGNETIC DAILY VARIATION AT TATUOCA, BRAZIL

The South Atlantic Anomaly is a region characterized by comparatively weak geomagnetic field strength with strong westerly declination and a strong bending of the magnetic equator. The Tatuoca geomagnetic observatory in Brazil (TTB, 1.2°S, 48.5°W) is located within this region and experiences a change of geomagnetic inclination of 0.4° per year (Thébault et al., 2015). Since the ionospheric dynamo currents are theoretically predicted to change with the Earth's main field, the behaviour of the geomagnetic daily variation in Brazil may also change over time due to the influence of the secular variation.

At low latitudes and in equatorial regions, the regular geomagnetic daily variation is mainly driven by the ionospheric solar quiet (Sq) and equatorial electrojet (EEJ) currents (Forbes, 1981; Yamazaki and Maute, 2017). Both Sq and EEJ currents are controlled by ionospheric conductivities, which depend on the plasma density and on the intensity of the geomagnetic main field (Takeda, 1996; Cnossen, 2017). The current density of the EEJ is on the order of 10⁻⁶ A/m², which is typically one order of magnitude greater than the low-latitude Sq currents (Onwumechili, 1997). The EEJ usually flows eastward within ±3° latitude around the magnetic equator, where a strong zonal Hall current results from the horizontal geomagnetic field. It is accompanied by return currents, which flow at low latitudes (3-9° away from the magnetic equator) in the opposite direction and with lower strength compared to the EEJ (Onwumechili, 1992; Zhou et al., 2018a). The eastward flow of the EEJ is sometimes observed to reverse westwards, giving rise to the so-called equatorial counter electrojet (CEJ), a phenomenon that mainly depends on the variability of the atmospheric tides and its effects on the global wind system (Gouin, 1962; Mayaud, 1977; Marriott et al., 1979; Hanuise et al., 1983; Gurubaran, 2002; Zhou et al., 2018b; Soares et al., 2019a).

Geomagnetic records from Brazil can provide valuable insight into the main field influence on the ionospheric currents, as it is a region of strong secular variation (Hartmann and Pacca, 2009). The first attempt to measure the EEJ magnetic field in the Brazilian sector dates back to March 1952, when a 13-day field campaign at the Island of Fernando de Noronha (3.9°S, 32.4°W, northeast Brazil, QD latitude was -0.6°) gave an average H-component daily range of 127 nT (Gama, 1953). Later, Gama (1972) described the average daily variation in Brazil from low-latitude and equatorial stations. Hesse (1982) focused on the investigation of the EEJ in the Brazilian sector, using a dedicated chain of 9 temporary stations and the geomagnetic observatories Vassouras (22.4°S, 43.6°W) and Paramaribo (5.8°N, 55.2°W).

Rigoti et al. (1999) used data from 16 selected quiet days from a temporary array of 29 vector magnetometers to model the EEJ in N-NE Brazil, inverting parameters such as current intensity, width and center.

More recent studies on the daily variation in the Brazilian sector were mostly based on relatively short data sets (Bolzan et al., 2018; Rastogi and Yumoto, 2007; Rastogi and Trivedi, 2009; Rastogi et al., 2010; Shume et al., 2010; Yizengaw et al., 2014). Moro et al. (2016) studied E-region electric field variability at the dip equator from 2001 to 2010 over Brazil and Peru by means of backscatter radar data. They indicated that the geomagnetic field secular variation significantly affects the measurements from the Brazilian sector. Recently, a 10-year long data set from TTB was used for the first time in a study on the occurrence of CEJ events (Soares et al., 2018a). Here, we further extend the TTB data back to the 1950s to investigate long-term changes in the geomagnetic daily variation associated with Sq and EEJ.

At a given longitude sector, Sq and EEJ magnetic signals are usually separated using measurements from a meridional (north-south) chain of stations crossing the magnetic equator (e.g., Yamazaki et al., 2010). Such a chain can measure equatorial and low-latitude ionospheric currents at the same time and allows for the investigation of individual geomagnetic events. With a single station like TTB, only a statistical analysis is possible, for instance by comparing annual means for years when the distance to the magnetic equator was large with annual means for years when this distance was small. On the other hand, using a single station with a long time series offers additional advantages: it allows the investigation of the field dependence on the magnetic equator distance at high resolution in geomagnetic latitude (as opposed to a sparse magnetometer chain) and with full local time and seasonal coverage (as opposed to satellites, which would need several years to reach full local time and seasonal coverage).

In this work, we show how and when the characteristics of the geomagnetic daily variation at TTB changed from the low-latitude “Sq type” to the equatorial “EEJ type”. For this purpose, we use TTB horizontal (H) component records and examine long-term changes in its daily range, solar flux dependence, seasonal variation, day-to-day variability, lunar variation and CEJ occurrence rate. The H component was chosen because it contains most of the signal that we are interested in (low-latitude Sq and EEJ) when compared to other geomagnetic components. We also analyze geomagnetic data from CHAMP and Swarm satellites to better understand the effects of the EEJ currents on TTB data. Lastly, we investigate the link between long-term changes in the daily variation at TTB and the secular variation of the main field using simulations with the Thermosphere-Ionosphere-Electrodynamics General Circulation Model (TIEGCM). The simulations allow us to isolate the effects of magnetic field changes from other potential sources of long-term change that are not taken

into account in our simulations, such as variations in solar activity, which affects Sq and EEJ variations primarily via its effect on ionospheric conductivity (e.g., [Rastogi and Iyer, 1976](#); [Yamazaki et al., 2011](#); [Takeda, 2013](#)), or whole-atmosphere anthropogenic climate change (e.g., [Marsh et al., 2013](#)), which could potentially affect ionospheric current systems via changes in upwardly propagating tides ([Yamazaki and Kosch, 2014](#)). Comparisons between modelled and observed long-term changes in the daily variation at TTB are used to check whether the secular variation in the main field is primarily responsible for the observed long-term changes or if other sources have played a role as well.

CHAPTER 10

DATA AND MODEL

10.1 TATUOCA GEOMAGNETIC OBSERVATORY

TTB observatory was installed in 1957 by Observatório Nacional on the Tatuoca Island (in the Amazon River, close to Belém, Brazil) and has been operating since then (Gama, 1958). Since 2015, TTB is operated in cooperation with the GFZ German Research Centre for Geosciences (Morschhauser et al., 2017). During the Second International Polar Year, a temporary magnetic station was established and operated on Tatuoca Island from September 1933 to January 1934 (Olsen, 1951). Figure 10.1a shows the average H component daily variation of 1933, 1964 and 2017 (solar minimum years) for September to January periods in Tatuoca, considering only the five quietest days of each month. A typical low-latitude H-component daily variation (i.e., H variation with nighttime values subtracted) is observed for 1933 (black dots) and 1964 (red line), with peak values of about 40 nT. The daily variation in 2017 (blue line) is significantly different and its noon-time range is almost two times larger.

The different patterns of the H-component daily variation observed for 1933, 1964 and 2017 may be explained by the changing geomagnetic latitudes of TTB due to the fast northward movement of the magnetic equator (an average of about 19 km per year since 1957, according to the International Geomagnetic Reference Field, IGRF-12, Thébault et al., 2015). Figure 10.1b shows the location of TTB (black triangle) and other low-latitude geomagnetic observatories with long time series (black circles) as well as the position of the magnetic equator for 1957 and 2017, which distinctively changed in the Brazilian sector. Indeed, Figure 10.1c shows that TTB is placed in the area of maximum difference in inclination values from 1957 to 2017 (nearly 25°, according to IGRF). Significant inclination changes can also be observed for the low-latitude stations KOU, VSS and MBO, but not for the other equatorial geomagnetic observatories HUA (see, e.g. Matzka et al., 2010), AAE

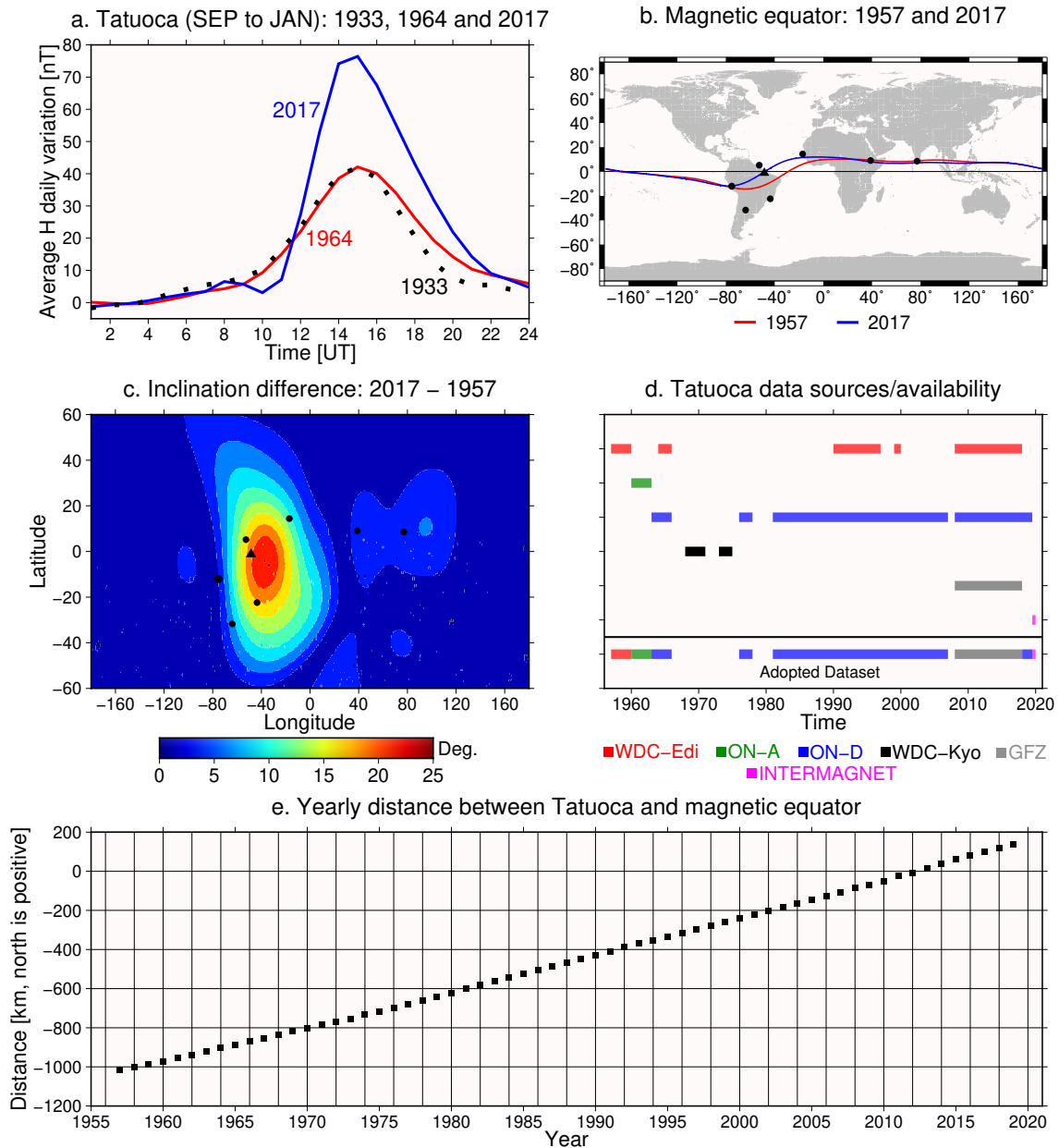


Figure 10.1: (a) Average H-component daily variation at Tatuoca for quiet days in the period from September to January for 1933 (black dots), 1964 (red line), and 2017 (blue line). (b) Map of selected equatorial and South American geomagnetic observatories with long time series. From west to east: HUA, PIL, KOU, TTB (highlighted as a black triangle), VSS, MBO, AAE, and TRD. The magnetic equator for 1957 (red) and 2017 (blue) is also shown. (c) Inclination change from 1957 to 2017 and observatories as in panel (b). (d) TTB H-component data availability versus time and its sources: WDC-Edi (WDC Edinburgh, digital), ON-A (Observatório Nacional, analogue), ON-D (Observatório Nacional, digital), WDC-Kyo (WDC Kyoto, analogue, not used here), GFZ (GFZ Data Services, digital), and INTERMAGNET (digital). (e) Yearly distance between TTB and the magnetic equator from 1957 to 2019.

and TRD. Details on the impact of long-term changes of the geomagnetic core field

strength and geometry on external fields are discussed in the review by [Cnossen \(2017\)](#).

In this work, we used hourly mean values of the geomagnetic field H-component measured at TTB from 1957 to 2019. Figure 10.1d shows the availability of TTB data and the corresponding data sources: WDC-Edi (WDC Edinburgh, digital data available at <http://www.wdc.bgs.ac.uk/>), ON-A (Observatório Nacional analogue data in [Gama, 1964](#)), ON-D (Observatório Nacional, previously unpublished digital data from the observatory archives), GFZ (GFZ Data Services, [Soares et al., 2018b](#)) and INTERMAGNET (International Real-time Magnetic Observatory Network, www.intermagnet.org). This leads to a combined data set of 49 years, while 14 years are still missing, mostly in the 1960s and 1970s, but also in 2007. A further potential source of TTB data to fill in these gaps, but still requiring digitalisation, are the magnetogram images available from WDC Kyoto at <http://wdc.kugi.kyoto-u.ac.jp/film/index.html> (labeled WDC-Kyo in Figure 10.1d) and from the Observatório Nacional analogue archives. The final data set, adopted in this work, is shown in the lower portion of Figure 10.1d. Additionally, Figure 10.1e shows the yearly distance between TTB and the magnetic equator from 1957 to 2019, according to IGRF-12. The magnetic equator moved 1155 km in 62 years with a nearly constant rate of change of 19km per year, crossing TTB around 2013.

The combined data set was processed before data analysis. A total of 237 spikes that could not be explained by geomagnetic field variations were deleted from the data set, 36 obvious typographic errors and 14 periods with unrealistic offsets were corrected. Time stamps had to be converted from local time to universal time in the TTB records until 1999. In addition, ON-D data from 2004 to 2006 were available only as raw variation data in units of millimeters as measured from photographic paper, which was used as the recording medium in a classical variometer system. In this case, data were calibrated by converting from millimeter to nanotesla (by using available scale value tables) and adding baseline values to the variation data in order to obtain absolute values of the field. These variation data were available with 1-minute resolution, which is unusual (often only hourly mean values are derived from photographic recordings in geomagnetic observatories). Then, hourly mean values were calculated according to the INTERMAGNET rule: an hourly mean value is computed only when 54 or more 1-minute values are available for the hour ([St-Louis, 2011](#); [Love, 2009](#)). For details on geomagnetic observatories and data processing, we refer to [Wienert \(1970\)](#), [Jankowsky and Sucksdorff \(1996\)](#), and [Matzka et al. \(2010\)](#). Our final processed TTB data set is available as a data publication ([Soares et al., 2020](#)) in GFZ Data Services.

The TTB H-component daily ranges (hereinafter referred to as H_A ranges) were computed from the hourly mean values by these three steps: Dst field correction as

explained in section 11.1; main field removal by subtracting a linearly interpolated baseline constructed from nighttime (22LT to 02LT, with LT = local time) averages; and finally, selection of the maximum value between 10LT and 14LT for each day.

10.2 ADDITIONAL GROUND-BASED DATA

Additional hourly mean values from the geomagnetic observatories Kourou (KOU, 5.2°N, 52.7°W) and Paramaribo (PAB, 5.8°N, 55.2°W) were used as low-latitude reference stations in the investigation of CEJ occurrence at TTB. Their data were downloaded from INTERMAGNET (www.intermagnet.org, data from 1996 to 2019) and WDC Kyoto (<http://wdc.kugi.kyoto-u.ac.jp/>, data from 1964 and 1965), respectively. Unlike TTB, the geomagnetic observatory Huancayo (HUA, 12.0°S, 75.3°W) remained close to the magnetic equator since its establishment in 1922 and, for this reason, its data from 1957 to 2019 (Soares et al., 2020) were used for comparison.

10.3 SATELLITE DATA

High-precision geomagnetic data from the Challenging Minisatellite Payload (CHAMP) and Swarm satellite missions were used. CHAMP is a German satellite that operated from July 2000 to September 2010 (Reigber et al., 2002). Swarm is a constellation of three satellites launched in November 2013 (Friis-Christensen et al., 2006, 2008).

In this work we used quiet time (K_p index ≤ 3) electric current intensity profiles for a quasi-dipole (QD) latitude range of -20° to $+20^\circ$ derived from both CHAMP (2000 to 2010) and Swarm (spacecraft A and B, 2013 to 2018) magnetic field data. Here, we used CHAMP and Swarm current profiles with latitudinal resolutions of 0.25° and 0.5° , respectively. They were obtained after removing the core (by the CHAOS-6 model, Finlay et al., 2016), lithospheric (by the MF7 model, Maus et al., 2008), magnetospheric (by the POMME-6 model, Maus and Lühr, 2005) and Sq (by fitting a low-degree spherical harmonic field model to the higher-latitude data) magnetic fields from the original magnetic field data and subsequently inverting the residual magnetic field for electric currents at an E-region height of 110 km (Alken et al., 2015, 2013).

10.4 GEOPHYSICAL INDICES

As this work targets geomagnetically quiet periods only, different geophysical indices were used either to attenuate the geomagnetic disturbances signal found in TTB data or to constrain the data set to periods of acceptable disturbance levels.

The Dst index (<http://wdc.kugi.kyoto-u.ac.jp/dstdir/index.html>) was used to correct for the disturbance field in the H-component. In addition, as a measure of geomagnetic activity level, we used the Kp index (<https://www.gfz-potsdam.de/en/kp-index/>) and the catalogue of international quiet days (IQDs) and disturbed days (IDDs). The IQDs and IDD are sub-products from the Kp index. The sunspot number (<http://www.sidc.be/silso/>) and the observed F10.7 solar radio flux (Tapping, 2013) were used as proxies of the solar activity.

Section 11.1 describes how each geophysical index mentioned above was used during data processing.

10.5 TIEGCM MODEL SETUP

The TIEGCM (version 2.0) was used to evaluate the effect of the change in the geomagnetic main field on the daily variation. The TIEGCM is a global three-dimensional, time-dependent model of Earth's upper atmosphere (97 to 600 km), developed at the National Center for Atmospheric Research (Qian et al., 2014; Richmond et al., 1992). The model configuration used here has a horizontal resolution of 2.5° in latitude and longitude and a vertical resolution of four grid points per scale height. The model uses the F10.7 index to calculate energetic solar radiation flux, which is a determining factor for heating in the thermosphere and ionization in the ionosphere. Solar wind data (including solar wind speed, density, and interplanetary magnetic field) are used to specify the ion convection pattern at high latitudes based on the empirical model by Weimer (2005). The model lower boundary is constrained by migrating solar diurnal and semidiurnal tides from the Global Scale Wave Model (Hagan and Forbes, 2002, 2003), which mimics tidal forcing effects on the ionosphere/thermosphere system.

CHAPTER 11

METHODS FOR DATA ANALYSIS

11.1 GEOMAGNETIC ACTIVITY

The Dst index was used to correct for the disturbance field in the H-component according to the approach described in (Yamazaki and Maute, 2017), here represented by the equation below:

$$\tilde{H} = H - (Dst \cdot \cos \theta), \quad (11.1)$$

where \tilde{H} is the corrected H-component, H is the original H-component and θ is the time-dependent geomagnetic latitude of the station.

Two methods were used to constrain the analysis to geomagnetically quiet periods. For those analyses based on monthly average values, we used only the ten quietest days of each month and, if more than 5 of these days correspond to data gaps, the month was excluded from the analysis (here, referred to as IQD constraint). For those analyses based on data of higher temporal resolution, we excluded only the 5 most disturbed days from each month (here, referred to as IDD constraint).

The Dst field correction, IQD and IDD constraints were not applied for the CEJ analysis. Instead, magnetic disturbance effects were mitigated by limiting the analysis to quiet days as selected by a Kp index criterion ($Kp \leq 3$). This allows for comparison with previous studies (for example, Marriott et al., 1979; Rastogi, 1974; Soares et al., 2018a, 2019a). The sunspot number data was also used for the CEJ analysis in order to account for CEJ solar cycle modulation.

The monthly mean values of the observed F10.7 solar radio flux were used to evaluate the influence of solar activity on the range of the H-component geomagnetic daily variation and remove the related variability from the data. For the day-to-day variability analysis, daily values of F10.7 were used to normalize the H-component data.

11.2 SOLAR FLUX DEPENDENCE

The magnitudes of geomagnetic daily variations associated with Sq and EEJ are correlated with the level of solar activity (e.g., Briggs, 1984; Matzka et al., 2017). This is because both Sq and EEJ currents are controlled by ionospheric conductivities, which linearly vary with the electron density. Under photochemical equilibrium conditions, the electron density is proportional to the square root of the EUV flux and, hence, to its proxy F10.7 index (Yamazaki and Kosch, 2014). In this sense, the daily H range is also expected to be proportional to the square root of F10.7, since the former is proportional to the ionosphere electron density (Stolle et al., 2008).

One of our aims is to isolate the effect of secular variation on the daily H_A ranges and, to achieve it, it is necessary to remove the solar flux influence from the data. To this end, we firstly grouped TTB data in 15 subsets according to years and seasons. Next, a linear fit was computed for each data subset through an iteratively reweighted least squares algorithm (Farquharson and Oldenburg, 1998), aiming for a robust fit. The linear fits were used to normalize the H_A data to a common reference of solar flux level. This was done by arbitrarily choosing a mid solar flux level of 100 sfu, according to:

$$H_N = H_A \cdot \frac{s(p) \cdot \sqrt{100} + i(p)}{s(p) \cdot \sqrt{F10.7} + i(p)}, \quad (11.2)$$

where H_N is the normalized H_A range, s and i are the linear regression coefficients (slope and intercept, respectively), p stands for corresponding subsets, F10.7 is the F10.7 value for the corresponding month (or day, in the case of day-to-day variability analysis), and 100 is used as the common reference solar flux level. The H_N is used in the analyses of transition from Sq to EEJ, seasonal dependence and day-to-day variability.

11.3 TRANSITION FROM SQ TO EEJ

The transition from Sq to EEJ was evaluated by the year-to-year variation of the average yearly values of the Dst-corrected, IQD-constrained and F10.7-normalized H_N range at TTB.

11.4 SEASONAL DEPENDENCE

The seasonal modulation of the geomagnetic daily variation was determined based on the Dst-corrected, IQD-constrained and F10.7-normalized H_N range data. To

represent the seasonal modulation, the H_N range data was binned per month. Afterwards, to take into account the change related to the Sq and EEJ periods, the data was averaged in five-year epochs (i.e., 1957 to 1961, 1962 to 1966, ..., 2010 to 2014, 2015 to 2019). This approach allows us to identify how the seasonal variation of the H_N range data changed between the Sq and EEJ periods in TTb.

11.5 DAY-TO-DAY VARIABILITY

The quiet time geomagnetic daily variation is subject to day-to-day changes in its amplitude and shape. A large part of the day-to-day variability is not yet fully understood (Yamazaki and Maute, 2017). Simultaneous measurements at equatorial and low-latitude stations indicate that the H range day-to-day variability differs significantly between the Sq and EEJ (Hamid et al., 2014; Yamazaki et al., 2014a). With the long-term data from TTb, it is possible to investigate how the day-to-day variability gradually changed from the Sq to the EEJ period. The day-to-day variability is computed as the H_N range differences between consecutive days (i.e., nT/day), after Dst correction, IDD-constraint and F10.7 normalization.

11.6 LUNAR VARIATION

In order to isolate the lunar variation (L), the TTb H-component hourly data was first Dst corrected and IDD-constrained. Then, the average solar variation was evaluated at each local time of each day as the average over ± 14 days at the same local time and then removed from the data, following the approach of Yamazaki and Maute (2017). The resulting hourly data were grouped according to solar cycle (SC) periods. The L amplitudes were determined by fitting the following equation independently to data from each SC period:

$$L(t, \nu) = \sum_{n=1}^4 a_n \cdot \sqrt{(F10.7)} \cdot \sin \left(n \frac{2\pi}{24} t - 2 \frac{2\pi}{24} \nu + \epsilon_n \right). \quad (11.3)$$

Equation 11.3 is based on Chapman's phase law (Chapman and Dyson, 1919), where t and ν are the local time and lunar age (phase) in hours, and a_n and ϵ_n are amplitude and phase parameters determined through ordinary least squares inversion (Çelik et al., 2012; Malin, 1970; Malin and Chapman, 1970). The F10.7 term included in equation 11.3 acts as a weighting factor and a solar flux of 100 sfu is used for normalization when calculating predicted L variations. All fits are based on more than 2200 days for each SC.

11.7 COUNTER-ELECTROJET OCCURRENCE

Upon entering the EEJ region, the H-component magnetic daily variation at TTB started to show, occasionally, depressions of the field below the nighttime base line, which is likely due to CEJ events. To investigate the CEJ occurrence at TTB, we used the same method as [Soares et al. \(2019a\)](#), based on the difference between the H hourly values from a pair of stations (one in the equatorial region and the other at low-latitude). We used the TTB-KOU pair for investigating CEJ occurrences since the year 1996, when the KOU time series started. In addition, as a sanity test, we used the TTB-PAB pair for the years 1964 and 1965 (when TTB was outside the EEJ influence). For the CEJ analysis, we do not correct the TTB data for the Dst field, as it is largely removed when the difference is taken for H observed at two closely located stations. To allow direct comparison with earlier studies, we do not normalize the data with F10.7. Only geomagnetically quiet days, selected based on the Kp index, were used.

11.8 TIEGCM SIMULATION

We performed TIEGCM simulations for 1961 and 2015. These years were selected because they have similar solar flux and geomagnetic activity conditions. The yearly average of the F10.7 index was 105.4 and 118.0 sfu (solar flux unit) for 1961 and 2015, respectively. The yearly average of the Ap index was 14.4 and 12.3 nT for 1961 and 2015, respectively. Both simulations were run with identical parameters except for the geomagnetic main field which was altered according to the IGRF. The F10.7 and solar wind inputs used for these runs correspond to conditions in 2015. The final TIEGCM outputs used in this work are hourly values of ground-level magnetic perturbations (i.e., variations) averaged for each month, which were calculated as described by [Doubria et al. \(2007\)](#) and [Richmond and Maute \(2014\)](#). These hourly values can be directly compared with observatory data.

CHAPTER 12

RESULTS AND DISCUSSION

12.1 SOLAR FLUX DEPENDENCE

Figure 12.1 shows the relationship between the H_A range and the square root of F10.7, where the top row shows data for a reference Sq period (1957 to 1996) and the bottom row for a reference EEJ period (1997-2019). These periods were based on the fact that, in 1996/1997, TTB was 3° away from the magnetic equator. Each column of Figure 12.1 stands for one of the three Lloyd seasons of the year: D (December solstice: November to February), E (equinox: March-April and September-October) and J (June solstice: May to August) months. Each circle in Figure 12.1 represents a monthly average (after IQD constraint) of H_A ranges and $\sqrt{F10.7}$, color-coded according to the year of observation. Circles with a black square in Figure 12.1 correspond to the months for which TTB data had to be converted from millimeter to nanotesla. On average, these data match well with the overall trend, confirming the validity of our data conversion technique. Regression lines were fit for the reference Sq and EEJ periods (black lines). It is noted that these regression lines depend on seasons.

The obtained slopes (s) and intercepts (i), as well as the RMS error of the fits are listed in Table 12.1. The RMS error is greater for the EEJ period, as expected from its higher variability observed in Figure 12.1.

These linear regression parameters were used in Equation 11.2, in order to obtain the normalized H_A range data (H_N).

12.2 TRANSITION FROM SQ TO EEJ

Figure 12.2a shows the year-to-year variation of the Dst-corrected, IQD-constrained and F10.7-normalized H_N range at TTB. The average yearly values of H_N are shown as dark blue squares and will be the metric used for discussion hereinafter. For

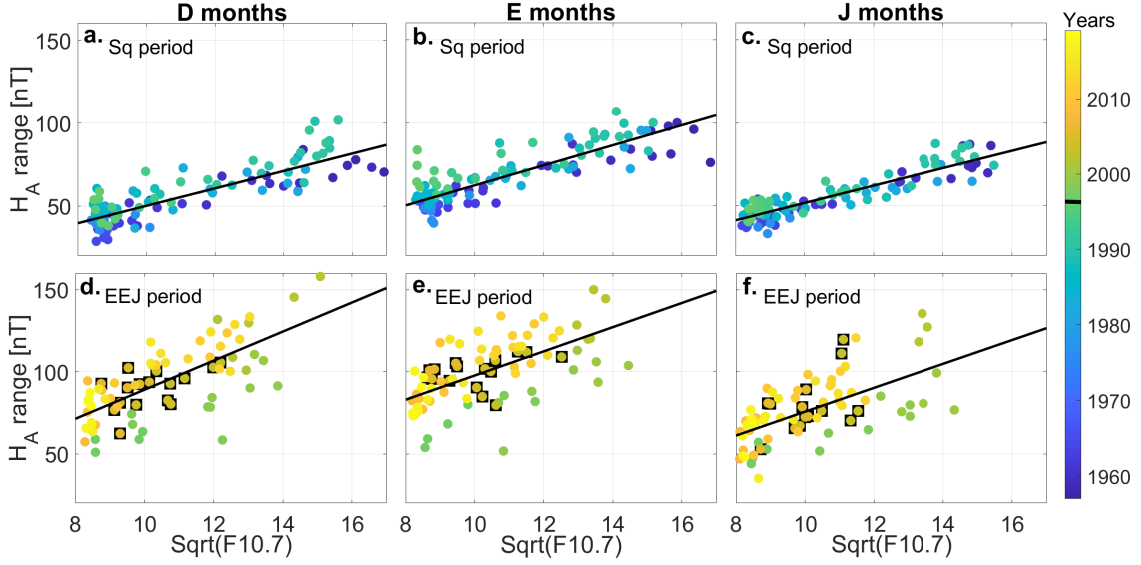


Figure 12.1: Monthly averages of TTB H_A range versus $\sqrt{F10.7}$ for D (Sq in panel (a) and EEJ in panel (d)), E (Sq in panel (b) and EEJ in panel (e)), and J (Sq in panel (c) and EEJ in panel (f)) months. The color code indicates the year (from 1957 to 2019). The black lines are linear fits to the data points during the Sq (1957–1996) and EEJ (1997–2019) periods. The horizontal black line in the color bar represents 1996/1997. Data that had to be converted from millimeter to nanotesla are indicated by black squares.

Table 12.1: Slope (s , in nT/\sqrt{sfu}) and intercept (i , in nT) of the linear fits between H_A range and $\sqrt{F10.7}$ for 15 subsets used to normalize H_A data. The corresponding RMS error (in nT) of the fit to the observed data is also shown. Data from 1966 to 1975 are not included in the table due to its unavailability.

PERIOD	D MONTHS	E MONTHS	J MONTHS
1957-1965	$s=5.00$ $i=-5.91$ RMS=6.11	$s=5.88$ $i=-0.51$ RMS=6.51	$s=5.53$ $i=-5.64$ RMS=4.93
1976-1986	$s=4.26$ $i=7.33$ RMS=7.47	$s=6.06$ $i=0.49$ RMS=6.53	$s=3.87$ $i=12.04$ RMS=4.92
1987-1996	$s=5.82$ $i=-3.33$ RMS=7.54	$s=5.29$ $i=16.70$ RMS=7.94	$s=5.49$ $i=-0.73$ RMS=5.30
1997-2008	$s=9.80$ $i=-18.06$ RMS=16.81	$s=6.69$ $i=24.15$ RMS=16.95	$s=7.01$ $i=-0.02$ RMS=17.64
2009-2019	$s=10.62$ $i=-9.69$ RMS=9.22	$s=10.81$ $i=-5.54$ RMS=11.06	$s=10.66$ $i=-25.04$ RMS=11.50

completeness, the data used to calculate these averages are also shown as circles for each year (in light blue for those found within the standard deviation σ interval and in light grey for those found beyond σ interval). The QD latitude decreases

almost linearly with time at TTB (Soares et al., 2018a) and the upper x axis in Figure 12.2a indicates corresponding QD latitude values. A gradual enhancement of H_N happens from 1981 to 1999 (about 11 nT change in 18 years), and a steeper gradient is observed from 1999 to 2001 (about 25 nT change in 3 years). Around 2013, when TTB QD latitude is zero, H_N reaches twice its initial value from 1957. The large increase in the H_N range can be explained by the transition of the daily variation from the Sq type to the EEJ type. For a comparison, Figure 12.2b shows an analogous plot using HUA H_N range data (average yearly values shown as dark red squares). HUA H_N range values are greater than those observed for TTB but are rather constant with time at around 115 nT. This is because HUA has been always inside the EEJ region, with QD latitudes varying non-linearly from -0.6° to 1.0° .

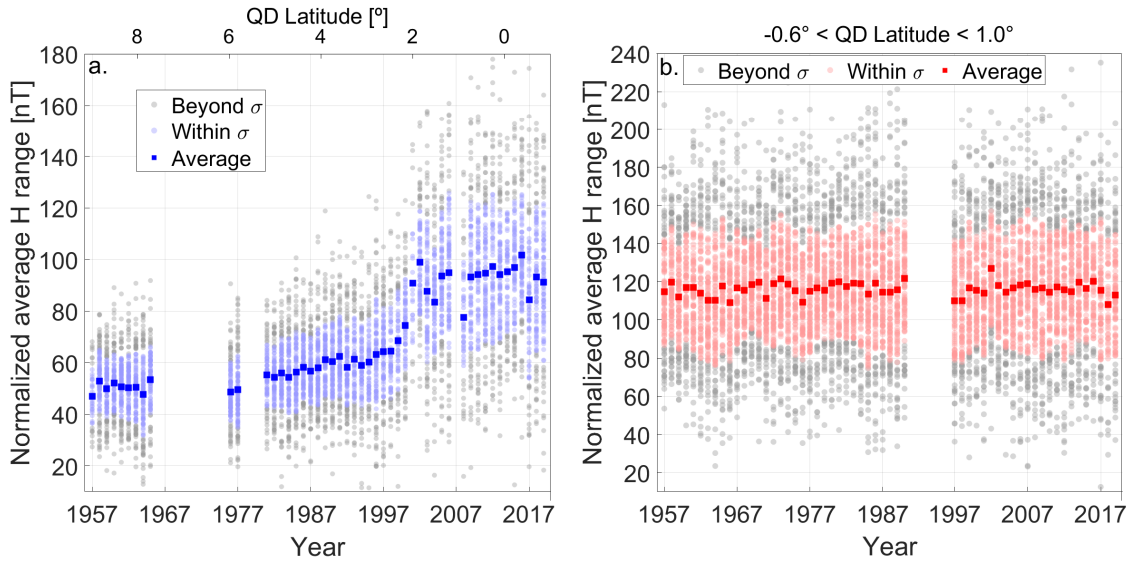


Figure 12.2: (a) Average yearly values of H_N range at TTB (dark blue squares). Light blue circles show data found within the standard deviation σ interval. Light gray circles show data found beyond σ interval. (b) Same as panel (a), but for HUA (red color is used instead of blue). The corresponding QD latitudes are shown in the upper abscissa.

To further characterize the EEJ magnetic signals at TTB, we use the combined CHAMP and Swarm satellite data set. Figure 12.3 shows the noon-time (10LT to 14LT) current intensity data (gray dots) along a QD latitudinal profile over the Brazilian sector (between 43.5°W and 53.5°W , centered at TTB longitude). Only quiet ($K_p \leq 3$) data are used. The average height integrated current intensity was calculated by a moving average of 0.5° in length and is shown by the magenta line. Since the large-scale Sq field is removed from the data in preprocessing, the peaks in the magenta line represent the EEJ and its return currents. We also calculated the magnetic field on the ground from this current intensity profile by using discrete line

currents at 108 km height and mirror currents at a depth of 200 km. This approach is based on Lühr et al. (2004) and Onwumechili and Ezema (1992) and yields the sum of the EEJ external and induced magnetic field components, which is shown by the purple line in Figure 12.3. The zero references for both x axis and y axes are shown by green lines.

The circles in Figure 12.3 indicate the EEJ peak, which occurs at 0.0° for the current intensity and 0.2° for the magnetic field. Given the usage of a moving average of 0.5° , there is an uncertainty of $\pm 0.25^\circ$ in the QD latitude of the current intensity values. A correspondent uncertainty of $\pm 0.24^\circ$ was estimated for the magnetic field profile on ground by taking the current intensity QD latitude error margin into account during its calculation. This is in reasonable agreement with the results of Lühr et al. (2004), who used CHAMP data from 2000 to 2003 and indicated that the EEJ peak occurs between -0.2° to 0.2° (within the ± 1 sigma uncertainty interval) for the Brazilian sector. Rastogi et al. (2008) estimated the EEJ centre position by using data from 1994 recorded by three magnetometer stations in Central Brazil (found within $\pm 2^\circ$ of dip latitude). They determined the EEJ centre by identifying where the vertical component daily range was zero after interpolating its values over the three stations. For noon-time, they found that the EEJ peak occurs between approximately -0.4° and -0.8° (with an error of $\pm 0.25^\circ$), which slightly deviates from the magnetic field result presented here ($0.2 \pm 0.25^\circ$ magnetic latitude). The discrepancy could be due to the fact that Rastogi et al. (2008) did not separate large-scale (Sq) and local-scale (EEJ) fields.

From southern to northern QD latitudes, the satellite-based current intensity profile shows that the normal EEJ region (magenta line positive values in Figure 12.3) extends from -3.2° to 3.5° QD latitude. In the ground magnetic field profile, this region extends from -4.3° to 5.0° . Therefore, both current intensity and magnetic field indicate some south-north asymmetry in the EEJ. Still inside the normal EEJ region, we could precisely find the QD latitudes of maximum EEJ rate of enhancement by applying the first derivative (not shown here) to the current intensity and magnetic field profiles. These are 2.0° for the current intensity and 2.7° for the magnetic field. This agrees with the steep H_N range increase at TTB around the year 2000, which occurred in a coincident QD latitude (Figure 12.2a).

The QD latitude of 5.0° corresponds to the beginning of the EEJ enhancement at TTB, in the 1980 decade (Figure 12.2a). This indicates that the EEJ contributed to the observed H_N gradual enhancement at TTB during the 1980s and 1990s. However, the Sq field also played a role in this H_N gradual enhancement, either by its temporal or spatial variations. Using south hemisphere magnetic ground data from 1964 to 2007, Torta et al. (2010) showed that no systematic drift occurred in the Sq focus latitudinal position. Thus, with a Sq system that largely maintained its

shape throughout the years, the main Sq-related variation is its spatial variation in H , which is smaller near the Sq focus and larger at lower latitudes (Takeda, 1999). Therefore, spatial changes of both EEJ and Sq contributed to the H_N variation observed at TTB during 1980s and 1990s.

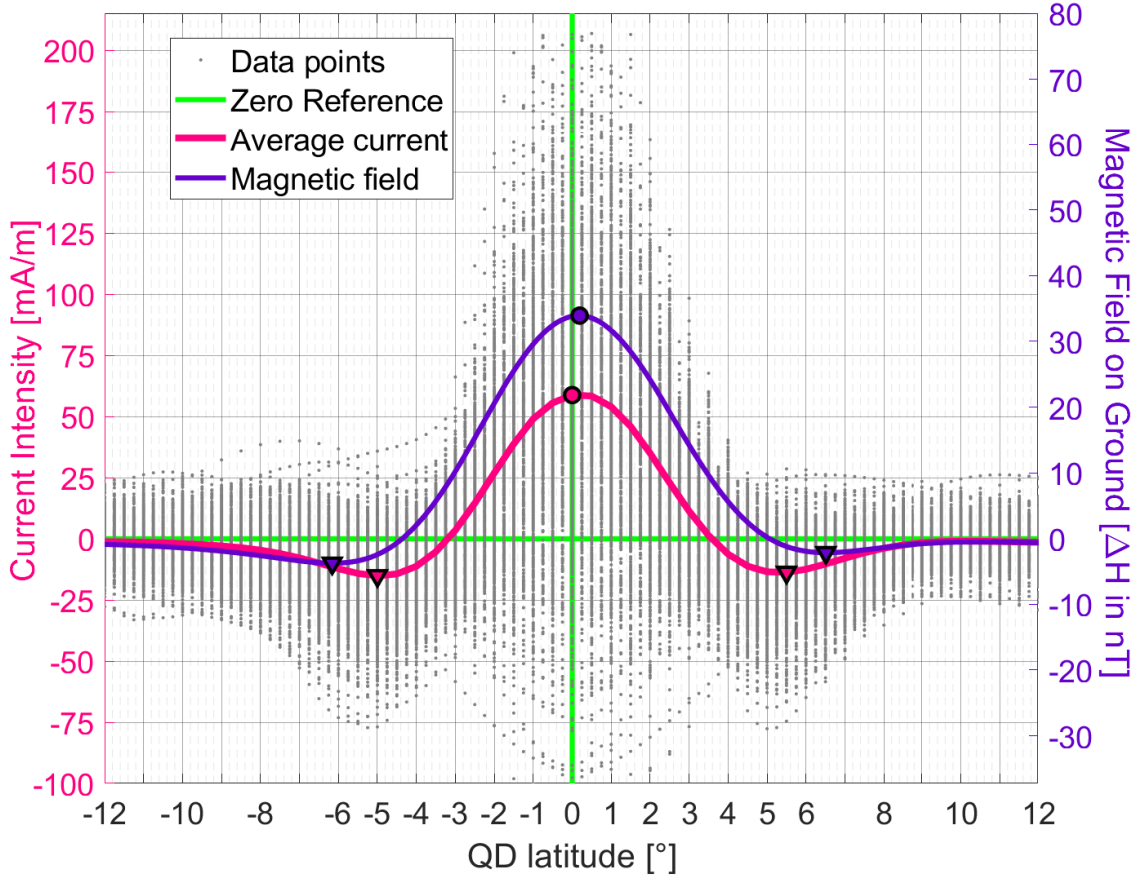


Figure 12.3: Quasi-dipole (QD) latitudinal profile of satellite-derived (CHAMP and Swarm) height-integrated current intensity (gray dots) and its average (magenta line) in the Brazilian sector (43.5°W to 53.5°W). Associated magnetic field at ground level is calculated by a line current model and shown by the purple line. Only quiet ($K_p \leq 3$) noon-time (from 10 to 14 LT) data from 2000 to 2018 are used. The EEJ maximum and return current minima values are shown by a circle and triangles in both current and magnetic field curves.

Asymmetries between the southern and northern return currents are observed in Figure 12.3. Their peaks (indicated by triangles) are located at -5° and 5.5° for current intensity and -6.2° and 6.5° for magnetic field. The return currents also differ in their peak amplitudes, from south to north: -15.1 to -13.7 mA/m for current intensity and -3.7 to -2.1 nT for magnetic field. Zhou et al. (2018a) also indicated that the northern return current is weaker when compared to its southern correspondent in the longitude sector that TTB is found. It is difficult to analyze return current effects with the available TTB data set because it is a weak signal (2.1 nT) that peaks at 6.5° QD latitude, during the major data gap in TTB (Figure

10.1d).

12.3 SEASONAL DEPENDENCE

Figure 12.4 shows the seasonal variation of the Dst-corrected, IQD-constrained and F10.7-normalized H_N range. Each solid line corresponds to a five-year average within the Sq and EEJ periods (i.e., 1957 to 1961, 1962 to 1966, ..., 2010 to 2014, 2015 to 2019). These lines are color-coded according to the period that they represent. The averaged patterns for the Sq (1957 to 1994) and EEJ (2000 to 2019) periods are shown as the dashed and dotted black lines, respectively, excluding the 1995 to 1999 transition data. A characteristic seasonal pattern is observed: the Sq period shows equinoctial maxima with solstitial minima (peak-to-peak amplitude of about 18 nT), while the EEJ period shows equinoctial maxima with a more prominent minimum during June-July (peak-to-peak amplitude of about 34 nT).

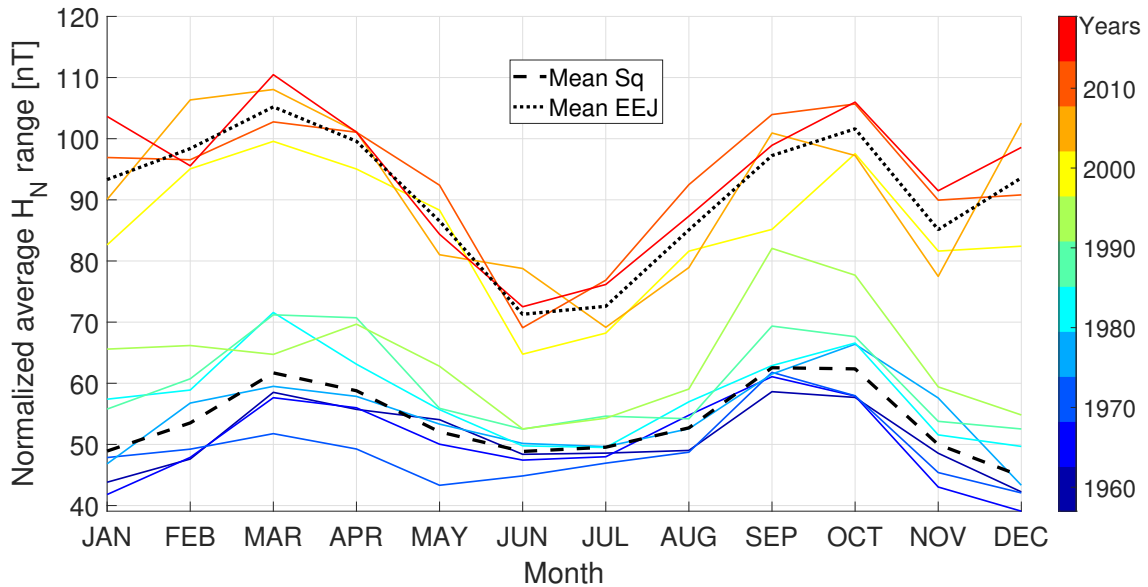


Figure 12.4: Seasonal variation of the normalized H_N range at TTB. Each solid line represents a 5-year period (color-coded according to the corresponding epoch). The Sq and EEJ averages are represented by dashed and dotted black lines, respectively.

The semiannual variation in the H_N range at low and equatorial latitudes is known from previous studies (Chapman and Rao, 1965; Campbell, 1982; Stening, 1995). Yamazaki et al. (2014b) numerically showed that neutral wind variability due to tidal waves from the lower atmosphere is the primary driver of the semiannual variation of the EEJ. Tidal waves from the lower atmosphere also play a dominant role in the semiannual variation of Sq as shown in Yamazaki and Maute (2017). The observed differences between Sq and EEJ can arise from their different generation mechanisms: the EEJ currents are primarily electric-field-driven, while low-latitude

Sq currents are partly electric-field-driven and partly local-wind-driven (Richmond and Roble, 1987).

Although the absolute values of seasonal variation amplitude increased by a factor of 2 from the Sq to the EEJ period, their relative contribution to the average daily variation stayed the same. Both Sq and EEJ average seasonal variation amplitudes (18 and 34 nT) correspond to about 35-40% of the average H_N range (50 and 95 nT, from Figure 12.2a). The main features of Sq and EEJ seasonal variations in TTB are in agreement with those obtained by Yamazaki et al. (2010) for the 120° to 130° longitude sector. The average EEJ seasonal variation in TTB also agrees with results obtained from ground-based magnetic data for other longitudes (Tarpley, 1973; Rastogi et al., 1994; Shume et al., 2010) and with satellite measurements over Brazil (Alken and Maus, 2007; Soares et al., 2018a).

12.4 DAY-TO-DAY VARIABILITY

Figure 12.5a shows the observed H_N range differences between consecutive days for TTB (in nT/day, blue dots) as a measure of day-to-day variability, after Dst correction, IDD-constraint and F10.7 normalization. Annual values of day-to-day variability standard deviation are shown by the green line.

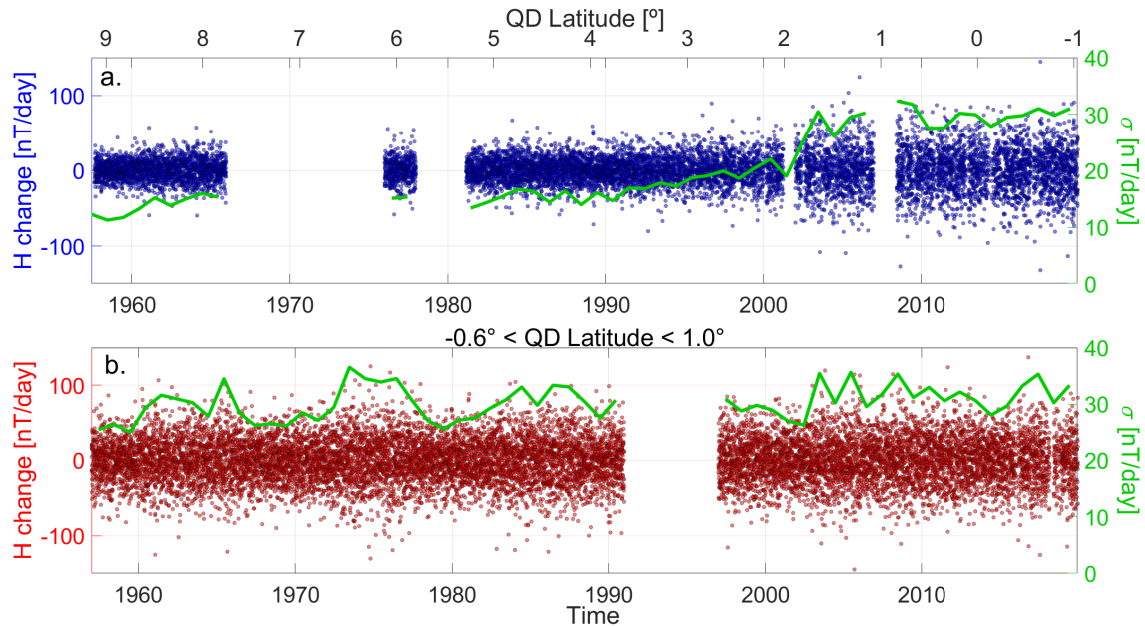


Figure 12.5: (a) Day-to-day variability at TTB, from 1957 to 2019 given by the difference in H range between consecutive days (in nT/day, blue dots). (b) Same as panel a, but for HUA (red dots). Annual values of day-to-day variability standard deviation (σ) are shown by the green line in both panels. TTB and HUA QD latitudes are shown on the upper abscissa.

The day-to-day variability shown in Figure 12.5a indicates periods of lower vari-

ability from 1957 to the early 1990s (Sq type), gradual variability enhancement during the 1990s and higher variability from 2000 to 2019 (EEJ type). This behavior can be easily identified by the annual values of day-to-day variability standard deviation. Such a long-term change is not observed at HUA (Figure 12.5b), where the change in the location of the magnetic equator is small.

Figure 12.6 shows histograms of day-to-day variability values for TTB (panels a and b) and HUA (panels c and d), during the periods of 1957 to 1984 and 2004 to 2019. These periods were chosen in a manner that they correspond to Sq and EEJ periods at TTB, respectively, and to a similar amount of data, what is convenient for a statistical comparison. Table 12.2 summarizes some statistical measures of each distribution shown in Figure 12.6: sample mean (\bar{x}), sample standard deviation (s) and sample size (n).

Visually, the histogram distributions for HUA and for the EEJ period in TTB are similar (Figures 12.6b, 12.6c and 12.6d), while the Sq period in TTB (Figure 12.6a) differs significantly. In addition, all distributions have similar sample means, but a distinctly different standard deviation of 14.4nT for TTB (1957 to 1984) as compared to 29.57, 29.58 and 31.92 nT for the other cases. This implies an enhancement of the day-to-day variability by a factor of 2 at TTB for the EEJ period, which does not occur at HUA.

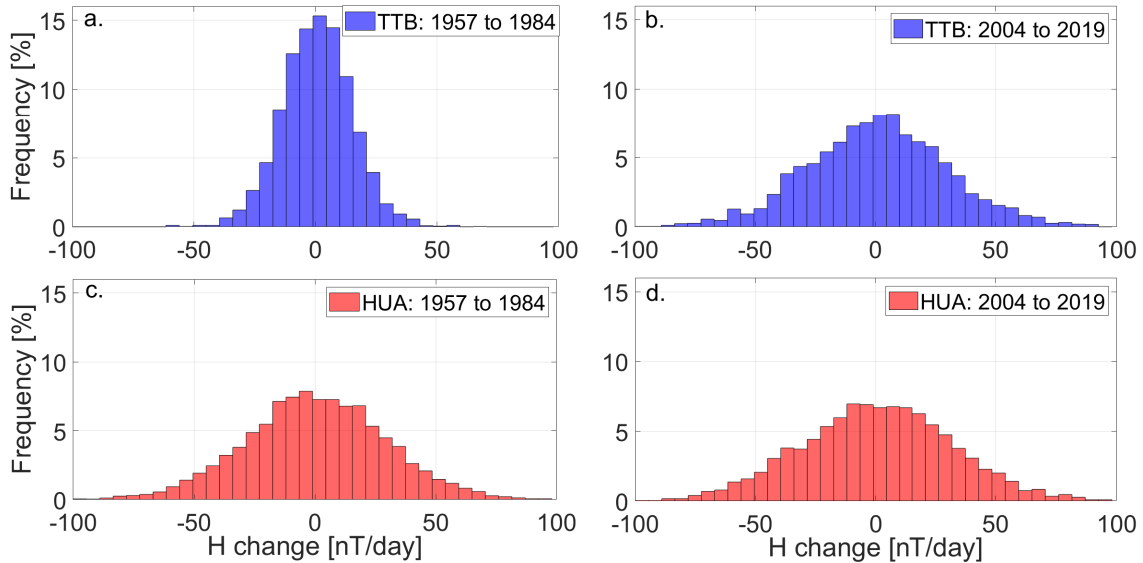


Figure 12.6: (a) Histogram of day-to-day variability values observed at TTB from 1957 to 1984 (Sq period). (b) Same of panel (a), but from 2004 to 2019 (EEJ period). (c) Same of panel (a), but for HUA. (d) Same of panel (b), but for HUA.

This comparison suggests that the change in the distance to the magnetic equator is the likely cause for the increased day-to-day variability observed at TTB, while long-term changes in the variability of magnetospheric and atmospheric forcing, which would affect both TTB and HUA data similarly, play only minor roles. It is

interesting to note that the magnitude of the day-to-day variability relative to the average H_N range (50 and 95 nT, from Figure 12.4a) is approximately 30% for both Sq and EEJ periods.

As known from previous studies, upward propagating tides and other large-scale waves from the lower atmosphere cause the day-to-day variation of the ionospheric wind dynamo, which therefore leads to the Sq and EEJ day-to-day variability (Miyahara and Oishi, 1997; Fang et al., 2013; Yamazaki et al., 2014a). Zonal and meridional wind components of those waves produce currents $\Delta \mathbf{J}_w = \sigma(\Delta \mathbf{U} \times \mathbf{B})$, where $\Delta \mathbf{J}_w$ and $\Delta \mathbf{U}$ are perturbations in the current density and winds, respectively, σ is the ionospheric conductivity tensor, and \mathbf{B} is the ambient magnetic field. Subsequently, electric field perturbations $\Delta \mathbf{E}$ arise in such a manner that total perturbation currents $\Delta \mathbf{J}_t$ satisfy the divergence-free condition. That is, $\nabla \cdot \Delta \mathbf{J}_t = \nabla \cdot [\sigma(\Delta \mathbf{E} + \Delta \mathbf{U} \times \mathbf{B})] = 0$. For the EEJ, σ is replaced by the Cowling conductivity σ_c , as the presence of the vertical electric field over the magnetic equator leads to an increase in the effective zonal conductivity (Richmond and Roble, 1987). Therefore, for both Sq and EEJ, the ratio of the perturbation currents to the background currents can be expressed in the form $(\Delta \mathbf{E} + \Delta \mathbf{U} \times \mathbf{B})/(\mathbf{E}_0 + \mathbf{U}_0 \times \mathbf{B})$, where \mathbf{E}_0 and \mathbf{U}_0 are the components of the electric field and winds that do not vary from day to day. Our results suggest that the magnitude of the day-to-day variability is significantly greater for the EEJ than Sq, which can be understood as $\sigma_c > \sigma$. Meanwhile, the relative magnitude of the day-to-day variation to the mean value is comparable for the EEJ and Sq because the relative magnitude is not sensitive to the ionospheric conductivity as shown above.

Table 12.2: Summary of statistical measures of each distribution of TTB and HUA day-to-day variability, including sample mean (\bar{x}), sample standard deviation (s) and sample size (n).

SAMPLE	\bar{x}	s (NT)	N
TTB (1957 to 1984)	0.73	14.44	3527
TTB (2004 to 2019)	0.89	29.57	3411
HUA (1957 to 1984)	0.38	29.58	7321
HUA (2004 to 2019)	0.59	31.92	4021

12.5 LUNAR VARIATION

Figure 12.7 (panels a, b, c, d and e) shows the predicted L variations at TTB as a function of local time and lunar age for each SC period. Note that SC 20 is not shown due to lack of data. SCs 19 and 21 show a consistently smooth semi-monthly L variation reaching amplitudes between 2.5 and 4 nT (Figures 12.7a and 12.7b). From SC 22 to SC 24, the L amplitude gradually increases (Figures 12.7c, 12.7d and 12.7e). The SC 22, already under the influence of the EEJ, presents an amplitude of 5.5 nT. SC 23 corresponds to the period of highest H range rate of change due to the increasing EEJ at TTB, and the L amplitude reaches 8 nT. In SC 24, epoch of minimum magnetic equator distance to TTB, the L amplitude is largest with 11 nT. Interestingly, the amplitude of L divided by the average H_N increased from $\sim 5\%$ (2.5 nT divided by 50 nT for SC 19) to $\sim 12\%$ (11 nT divided by 95 nT for SC 24) at TTB. This indicates that, for the Brazilian sector, the EEJ is more sensitive to lunar tides than Sq is.

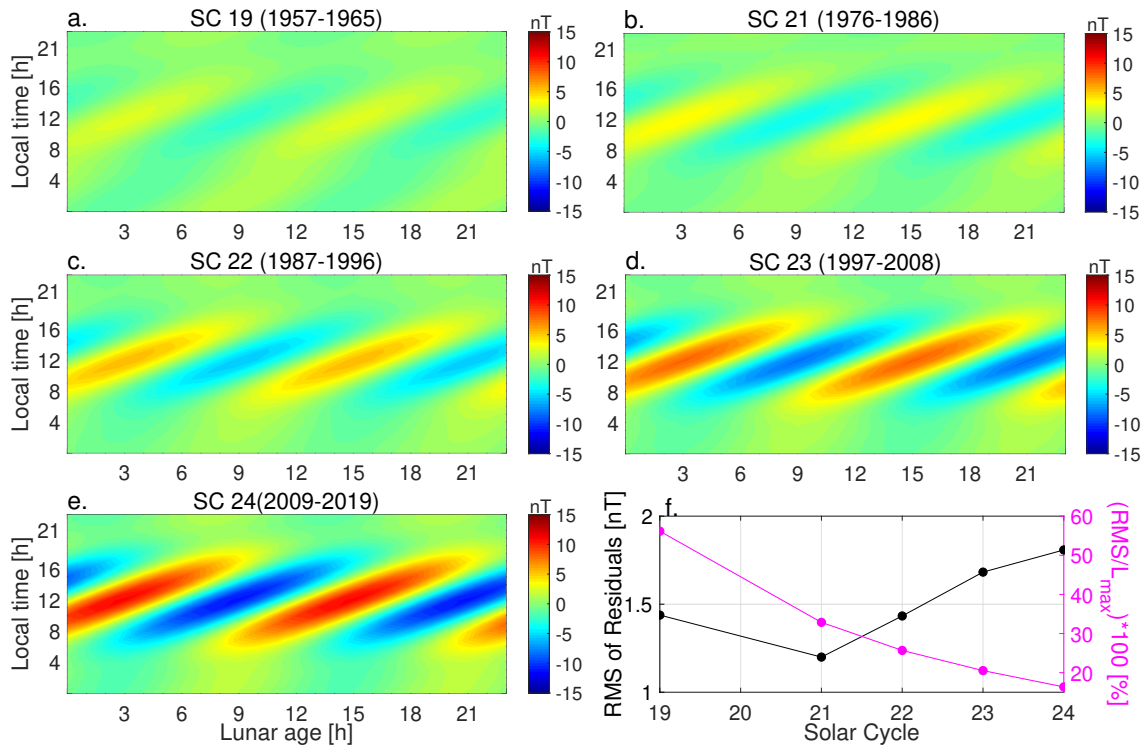


Figure 12.7: Predicted average amplitude of the lunar variation L (in nT) in TTB H-component, as a function of local time and lunar age, during solar cycles (SC) 19 (a), 21 (b), 22 (c), 23 (d), and 24 (e). The RMS values of the residuals (error in nT, black circles) and their relation to the maximum L variation amplitudes (in %, magenta circles) are shown in (f).

RMS values of the residuals (differences between predicted and observed L amplitudes, black circles in Figure 12.7f) are between 1 and 2 nT, which corresponds to

less than 35% of the maximum L variation amplitudes (magenta circles in Figure 12.7f), except for SC 19 with 56% due to its weak L signal. As expected, the RMS increases with the increasing L amplitude due to larger EEJ signal, but its relative importance (i.e., associated error) diminishes.

The amplitude of the L variation at TTB was also determined by Malin (1973), who used data from 1957.5 to 1960.5 (a total of 706 days, Sq period in TTB). An amplitude of about 3.2 nT was obtained, which agrees with the result presented here for SC 19. For the same epoch, Malin (1973) computed L variations of about 16.2 nT at HUA, over the equator. There is no solar flux normalization in Malin’s analysis.

For a comparison, we performed the same analysis with HUA data from SCs 19 and 24 (Figures 12.8a and 12.8b). Unlike at TTB, nearly identical results were obtained for both solar cycles with maximum amplitudes of 12.2 and 13.3 nT, respectively. These results are comparable to those of Malin (1973) and Yamazaki and Maute (2017). Thus, the L amplitudes at HUA (Figure 12.8) and TTB (mainly during SC 24, Figure 12.7e) are similar, as both are under EEJ conditions. The relative amplitude of L at HUA was rather constant over time: $\sim 11\%$ (12.2 nT of 115 nT) and $\sim 12\%$ (13.3 nT of 115 nT) for SCs 19 and 24, respectively.

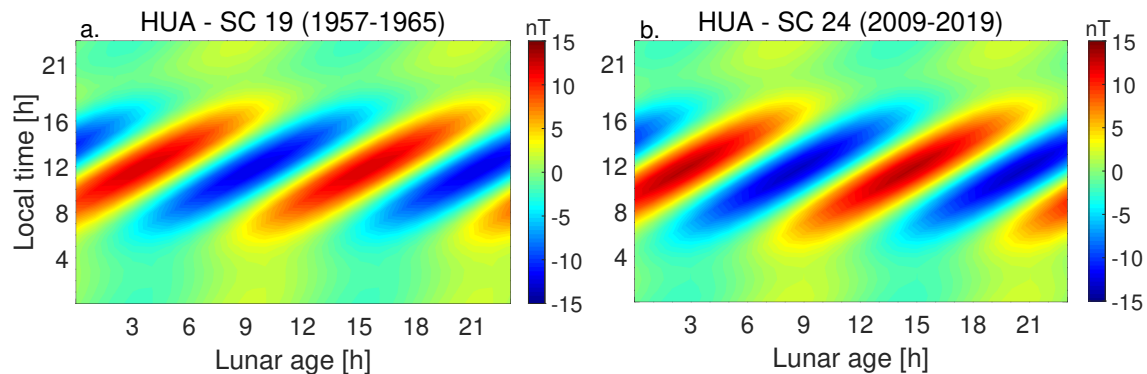


Figure 12.8: Predicted average amplitude of the lunar variation L (in nT) in HUA H-component, as a function of local time and lunar age, during solar cycles (SC) 19 (a) and 24 (b).

12.6 COUNTER-ELECTROJET OCCURRENCE

The annual rates of morning (MCEJ, 6 to 10 LT) and afternoon (ACEJ, 14 to 18 LT) counter electrojet events at TTB are shown in Figure 12.9a together with the annual values of sunspot number given by the gray area. The corresponding QD latitude of TTB is shown on the upper abscissa. The results from SC 24 (2009-2019) indicate a predominance of MCEJ and an anti-correlation of ACEJ with the solar cycle, which is consistent with previous results for the years 2008 to 2018 (Soares

et al., 2018a, 2019a). For SC 23 (1996-2008), we find very low MCEJ rates of around 15% from 1996 until 2001. A jump in MCEJ rates occurs from 2001 to 2002, which is the period of highest increase of EEJ signal, as indicated in Figures 12.2 and 12.3. During the SC 24, an average rate of 50% was observed for MCEJ. On the other hand, the ACEJ rates show very similar values and behavior during both SCs 23 and 24.

For a comparison, Figure 12.9b shows the same analysis using the pair TTB-PAB for the years 1964 and 1965. In this case, both TTB (1965 QD latitude: 8.1°) and PAB (1965 QD latitude: 17.1°) were located outside the EEJ influence. As expected, very low rates are observed in both cases (less than 5%). This indicates that the rates observed from 1996 to 2001 at TTB (between 10 and 40%) actually refer to CEJ events, which in addition, preserve the solar cycle modulation of ACEJs. Another MCEJ and ACEJ feature that is preserved from SC 23 to 24 is their seasonal variation (not shown here but similar to the results presented by Soares et al., 2018a).

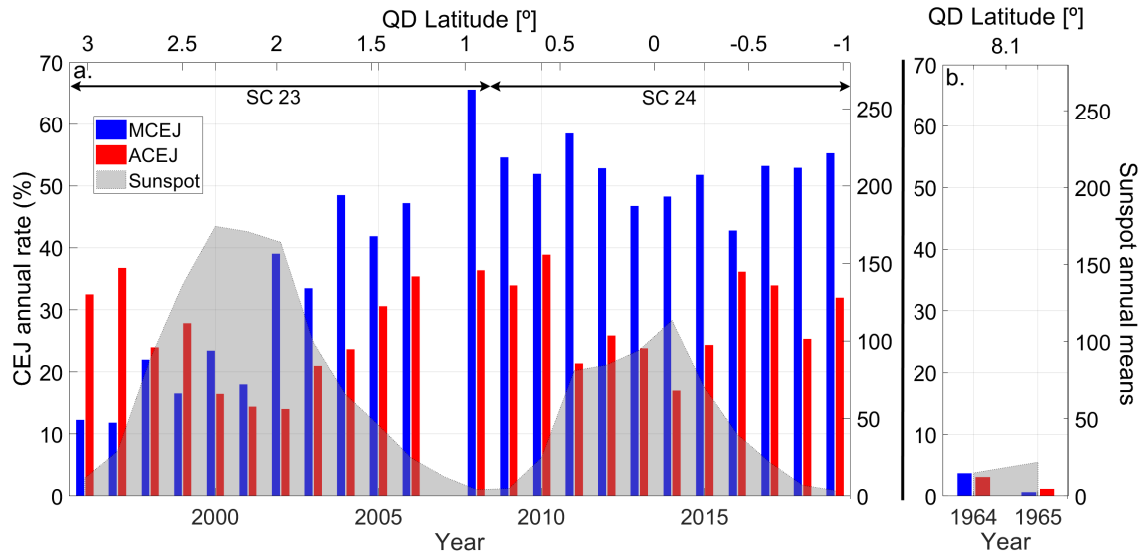


Figure 12.9: (a) Annual occurrence rates of morning (MCEJ, blue bars) and afternoon (ACEJ, red bars) counter electrojet events at TTB derived from the TTB-KOU pair during 1996-2019. (b) Same as panel a but for the TTB-PAB pair during 1964-1965. Annual means of sunspot number are shown as a gray area in both panels. TTB QD latitude is shown in the upper abscissa. Solar cycles 23 and 24 are indicated by black arrows.

With these observations, one question arises: why does the MCEJ behave differently during 1996-2001 and 2002-2019 while the ACEJ does not? To answer this question, we analyzed the combined CHAMP and Swarm satellite current intensity data. Figure 12.10 shows the occurrence rate of westward currents for both morning (blue) and afternoon (red) periods, as a function of QD latitude for the Brazilian sector (between 43.5°W and 53.5°W, centered at TTB longitude). Each rate value was calculated by a moving window of 1° of QD latitude, which was moved in steps

of 0.5° . Thus, each rate represents the percentage of negative current intensity values in relation to the total data points found in the QD latitude window. Two different thresholds were used to detect negative current densities: -5 mA/m (shown in Figure 12.10) and -10 mA/m (similar results, not shown here). We will focus on the area between the two vertical black dashed lines in Figure 12.10, which represents the EEJ region ($\pm 3.5^\circ$ QD latitude, according to the latitudinal profile shown in Figure 12.3), where westward current rates indicate CEJ occurrence rates. The peaks in the westward current rates outside the EEJ region (near 5°) indicate the return currents flow, which are not discussed in this section.

In the EEJ region indicated in Figure 12.10, MCEJ rates have a prominent central peak at 0.5° QD latitude (EEJ central axis) and greatly exceed ACEJ rates. Indeed, the latitudinal variation of MCEJ and ACEJ rates shown in Figure 12.10 are quite different. This latitudinal dependence can explain the abrupt change in MCEJ rates at TTB from the years 1996 to 2001 (QD latitudes $+3.1^\circ$ to $+2.2^\circ$) to the years 2002 to 2019 (QD latitudes $+2.1^\circ$ to -1.0°), and the apparent continuity of ACEJ rates at TTB, being modulated by the solar activity.

The results suggest that there is a significant latitudinal variation in the CEJ occurrence rate within $\pm 3^\circ$ magnetic latitudes, which has not been previously reported. It means that the latitudinal variation of the CEJ occurrence rates needs to be taken into account when comparing MCEJ and ACEJ rates obtained from ground stations at different epochs or longitude sectors. Thus, we highlight the importance of using equatorial stations as close to the EEJ center as possible to keep tracking the EEJ and associated CEJ events with enough precision.

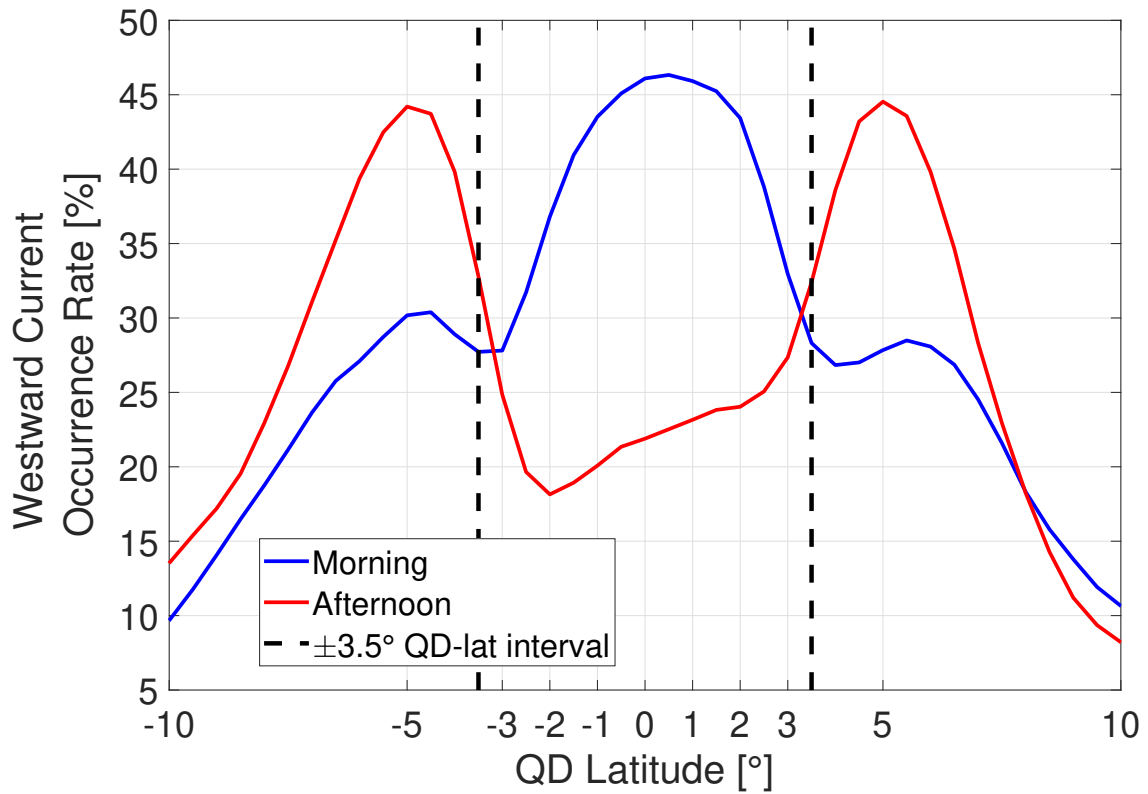


Figure 12.10: (a) QD latitudinal profile (-10° to $+10^{\circ}$) of westward current occurrence rate at the Brazilian sector, derived from CHAMP and Swarm satellite data, considering only current intensity values below -5 mA/m. Morning (6 to 10 LT) and afternoon (14 to 18 LT) occurrence rates are shown as blue and red lines, respectively. The $\pm 3.5^{\circ}$ QD latitude interval (EEJ region) is shown between the two vertical black dashed lines.

12.7 TIEGCM SIMULATION

The average H-component geomagnetic daily variations at TTB and HUA, for 1961 and 2015, are shown in Figures 12.11a and 12.11b, respectively. In this analysis, we corrected the H-component data for the Dst field, as the TIEGCM simulation does not include the magnetospheric ring current contribution. For TTB, two distinct patterns of daily variation can be seen in 1961 (solid line) and 2015 (dashed line). On the other hand, the daily variations at HUA are nearly identical in 1961 and 2015. The indicated error bars represent the 95% confidence intervals and were calculated by the bootstrap technique (Efron, 1981).

The ground magnetic perturbations on the H-component obtained from the TIEGCM model are shown in Figures 12.11c and 12.11d. Due to the model resolution, we used the geographical coordinates that are nearest to TTB and HUA, which are 1.9°S/49.5°W and 11.2°S/76.5°W, respectively (interpolating the model results for TTB and HUA coordinates yields equivalent values). It is known that the model underestimates the ionospheric E-region conductivities and, hence, the amplitudes of the ground magnetic perturbations (Doubmbia et al., 2007). This explains, at least in part, the different absolute values obtained for the observations and model predictions. Thus, in what follows, a comparison between data and model is made only in a relative sense.

For TTB noon-time, considering the error margins, data and model indicate an increase from 1961 to 2015 within the intervals of 89 to 120% and 73 to 139%, respectively. For HUA noon-time, data indicates an increase from 2 to 18%, while the model indicates a result between a decrease of 13% until an increase of 10%. Therefore, considering the error margin, data and model represent the same relative change in the noon-time daily variation. Data and model also agree that large changes occurred at TTB and small changes occurred at HUA from 1961 to 2015. This means that the differences in the geomagnetic main field due to secular variation can explain the change in the H-component daily variation observed at TTB, since the only difference between the two simulations is the geomagnetic main field, based on the IGRF.

Previous studies also performed numerical simulations to investigate long-term changes in geomagnetic daily variations. Cnossen and Richmond (2013) used the Coupled Magnetosphere-Ionosphere-Thermosphere (CMIT) model to simulate the effects of the geomagnetic main field variations over a century and found that the secular variation is the dominant cause of slowly varying changes in the ionosphere over the Atlantic region. They predicted that, in this region, strong changes would occur in the amplitude of the Sq variation, which we confirmed using TTB long-term observations. By using CMIT simulations and ground-based geomagnetic data from

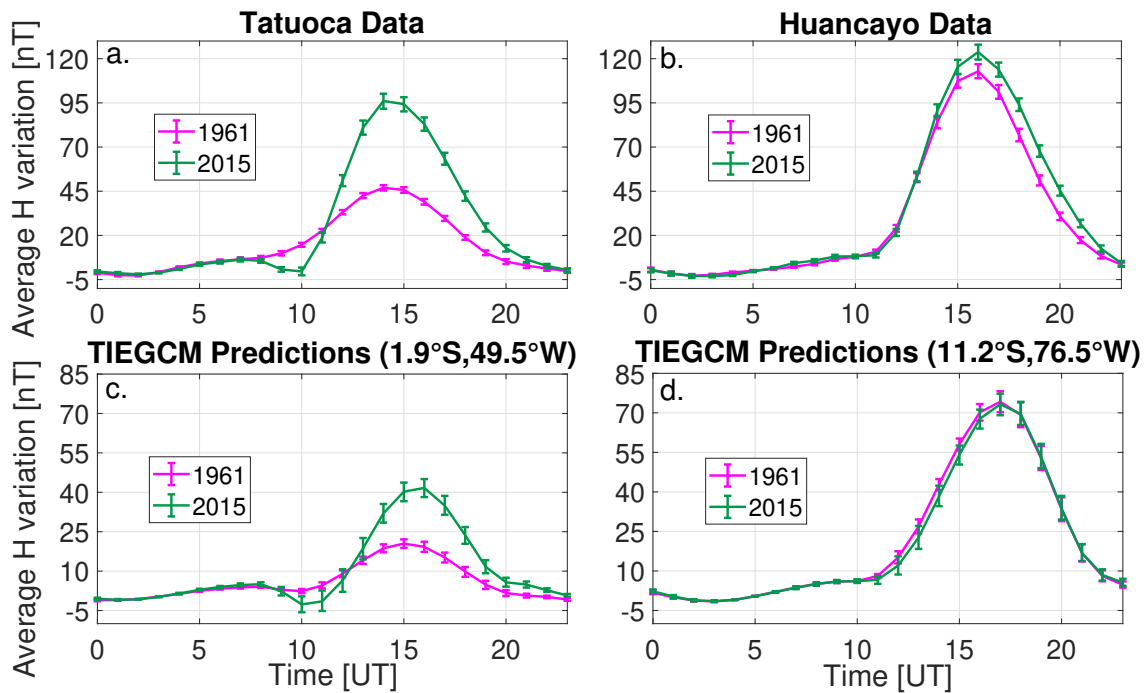


Figure 12.11: (a) Yearly mean geomagnetic H daily variation observed at TTB in 1961 (green line) and 2015 (magenta line). (b) Same as panel (a), but for HUA. (c) Yearly mean ground magnetic perturbations of the H-component, derived from the TIEGCM for the region of Tatuoca using the geomagnetic main field of 1961 (green line) and 2015 (magenta line). (d) Same as panel (c), but for the region of Huancayo. Error bars represent the 95% confidence interval.

1960-2000, [de Haro Barbas et al. \(2013\)](#) concluded that the secular variation is the main cause of the long-term changes in the Sq amplitude. They suggested a future study involving stations that experienced a large shift in their position with respect to the magnetic equator, which is accomplished in this work with TTB data and TIEGCM simulations.

Besides the field geometry, the field intensity also plays a role on the geomagnetic daily variation, as it controls the ionospheric conductivities ([Takeda, 1996](#); [Cnossen, 2017](#)). Studies have found small increases in Sq and EEJ strengths during the last decades, which can be attributed, at least in part, to the overall reduction of the main field intensity ([Elias et al., 2010](#); [Matzka et al., 2017](#)). It is beyond the scope of this work to separate the effect of the field intensity and the effect of the field geometry on the daily variation recorded at TTB.

CHAPTER 13

CONCLUSIONS

13.1 EVOLUTION OF THE GEOMAGNETIC DAILY VARIATION AT TATUOCA, BRAZIL

A new ground-based geomagnetic data set from Tatuoca observatory (TTB, 1.2°S, 48.5°W) in Brazil has been recovered, processed and analysed. It provides information on the daily variations at both low and equatorial latitudes. TTB geomagnetic observatory has been operating for more than 60 years in an area where the magnetic equator moves at its fastest rate, with an average of 19 km per year since 1957.

This unique condition allows us to examine long-term changes due to geomagnetic secular variation on the daily variation of the measured H-component, using data from 1957 until 2019. This period includes the transition of the daily variation from the low-latitude Sq type to the equatorial EEJ type. In particular, long-term trends in the H range day-to-day variability were investigated for the first time in the Brazilian sector. In addition, we separated the effect of other important variables that influence the daily variation, such as solar activity, seasonal variation and lunar variation. To facilitate the interpretation of our results, we use satellite derived current intensity profiles and two TIEGCM simulations with different configurations of the geomagnetic main field. The main findings of this work include:

- A comparison of ground observations at TTB and magnetic field at ground level calculated from satellite derived current profiles provided the latitudinal extent of the EEJ in the Brazilian sector. We found that the EEJ region extends from -4.3° to 5.0° QD latitude and peaks at 0.2° QD latitude. The northern EEJ return current as seen in the ground magnetic field peaks at 6.5° , while the southern return current peaks at -6.2° . The northern return current magnetic field amplitude is 1.8 times weaker than the southern.
- The daily H range at TTB has increased over time (1957 to 2019) by a factor

of 2, reflecting the transition of the daily variation from the Sq type to the EEJ type.

- The relation between the H daily variation range and the square-root of the solar flux has changed over time, and different linear relations were obtained for the Sq and EEJ periods.
- The H range seasonal variation at TTB shows larger amplitudes during the EEJ period. However, the Sq and EEJ seasonal variation amplitudes relative to the average daily range remained at a similar level (35-40%).
- The day-to-day variability at TTB during the EEJ period was found to be higher than during the Sq period by a factor of 2. The magnitudes of the day-to-day variability relative to the average daily range remained at 30% during both Sq and EEJ periods.
- The amplitude of the lunar variation L in TTB H-component increased from solar cycle 19 to 24. The L amplitude relative to the average daily range increased from 5% to 12%. This indicates that the EEJ in the Brazilian sector is more sensitive to lunar tides than Sq is.
- At TTB, the MCEJ occurrence rate changed from 15% to 50% within the QD latitude interval from $+3^\circ$ to 0° , whereas the ACEJ remained at similar levels and maintained the well-known solar cycle modulation. This result agrees with the latitudinal gradients of MCEJ and ACEJ occurrence rates in the Brazilian sector, as revealed by satellite data. It is suggested that the latitudinal dependence of the CEJ occurrence rates should be taken into account in CEJ studies, even for QD latitudes smaller than 3° .
- Two TIEGCM simulations were performed: one with the geomagnetic main field of 1961 and the other with the main field of 2015. The model was able to reproduce the different patterns of the geomagnetic daily variations observed at TTB in 1961 and 2015. The results indicate that the geomagnetic main field plays the dominant role in causing the long-term changes in the daily variation observed at TTB.

Part IV

PUBLICATIONS

CHAPTER 14

PUBLICATIONS

14.1 RELATED TO THIS THESIS

The manuscript related to the Part II of this thesis, entitled “Using Principal Component Analysis of Satellite and Ground Magnetic Data to Model the Equatorial Electrojet and Derive Its Tidal Composition”, was published in September 2022 in the Journal of Geophysical Research – Space Physics (<https://doi.org/10.1029/2022JA030691>).

The manuscript related to the Part III of this thesis, entitled “Evolution of the geomagnetic daily variation at Tatuoca, Brazil, from 1957 to 2019: a transition from Sq to EEJ”, was published in August 2020 in the Journal of Geophysical Research – Space Physics (<https://doi.org/10.1029/2020JA028109>).

14.2 ADDITIONAL PUBLICATIONS

A manuscript entitled “Whole atmosphere model simulations of ultra-fast Kelvin wave effects in the ionosphere and thermosphere”, which I am a co-author, was published in the Journal of Geophysical Research – Space Physics in June 2020 (<https://doi.org/10.1029/2020JA027939>). This is an extra research topic, independent of the PhD project, in which I contributed with the preparation of geomagnetic ground-based data and with text revision.

A manuscript entitled “Geomagnetic detection of the atmospheric acoustic resonance at 3.8 mHz during the Hunga Tonga eruption event on January 15, 2022”, which I am a co-author, was published in the Journal of Geophysical Research – Space Physics in July 2022 (<https://doi.org/10.1029/2022JA030540>). The article describes the geomagnetic effects of the Hunga Tonga eruption occurred in January 15, 2022 as measured by geomagnetic observatories. This is an extra research topic, independent of the PhD project, in which I actively contributed with the

observational analysis (detection of the eruption-related geomagnetic disturbance) and with the manuscript text.

Part V

BIBLIOGRAPHY

BIBLIOGRAPHY

- Alken, P., Maus, S., 2007. Spatio-temporal characterization of the equatorial electrojet from champ, ørsted, and sac-c satellite magnetic measurements. *J. Geophys. Res* 112.
- Alken, P., Maus, S., Chulliat, A., Vigneron, P., Sirol, O., Hulot, G., 2015. Swarm equatorial electric field chain: first results. *Geophys. Res. Lett.* 42, 673.
- Alken, P., Maus, S., Vigneron, P., Sirol, O., Hulot, G., 2013. Swarm l2ps equatorial electric field inversion chain. *Earth Planets and Space* 65 (11), 1309–1317.
- Alken, P., Maute, A., Richmond, A. D., Vanhamäki, H., Egbert, G. D., 2017. An application of principal component analysis to the interpretation of ionospheric current systems. *Journal of Geophysical Research: Space Physics* 122 (5), 5687–5708.
URL <https://agupubs.onlinelibrary.wiley.com/doi/abs/10.1002/2017JA024051>
- Alken, P., Thébaud, E., Beggan, C. D., Amit, H., Aubert, J., Baerenzung, J., Bondar, T. N., Brown, W. J., Califf, S., Chambodut, A., Chulliat, A., Cox, G. A., Finlay, C. C., Fournier, A., Gillet, N., Grayver, A., Hammer, M. D., Holschneider, M., Huder, L., Hulot, G., Jager, T., Kloss, C., Korthe, M., Kuang, W., Kuvshinov, A., Langlais, B., Léger, J.-M., Lesur, V., Livermore, P. W., Lowes, F. J., Macmillan, S., Magnes, W., Manda, M., Marsal, S., Matzka, J., Metman, M. C., Minami, T., Morschhauser, A., Mound, J. E., Nair, M., Nakano, S., Olsen, N., Pavón-Carrasco, F. J., Petrov, V. G., Ropp, G., Rother, M., Sabaka, T. J., Sanchez, S., Saturnino, D., Schnepf, N. R., Shen, X., Stolle, C., Tangborn, A., Tøffner-Clausen, L., Toh, H., Torta, J. M., Varner, J., Vervelidou, F., Vigneron, P., Wardinski, I., Wicht, J., Woods, A., Yang, Y., Zeren, Z., Zhou, B., Feb 2021. International geomagnetic reference field: the thirteenth generation. *Earth, Planets and Space* 73 (1), 49.
URL <https://doi.org/10.1186/s40623-020-01288-x>

- Anandarao, B. G., Raghavarao, R., 1987. Structural changes in the currents and fields of the equatorial electrojet due to zonal and meridional winds. *Journal of Geophysical Research: Space Physics* 92 (A3), 2514–2526.
URL <https://agupubs.onlinelibrary.wiley.com/doi/abs/10.1029/JA092iA03p02514>
- Blanc, M., Richmond, A. D., 1980. The ionospheric disturbance dynamo. *J. Geophys. Res.* 85, 1669–1686, doi:10.1029/JA085iA04p01669.
- Bolzan, M. J. A., Denardini, C. M., Tardelli, A., 2018. Comparison of *h* component geomagnetic field time series obtained at different sites over south america. *Annales Geophysicae* 36 (3), 937–943.
URL <https://angeo.copernicus.org/articles/36/937/2018/>
- Briggs, B., 1984. The variability of ionospheric dynamo currents. *Journal of Atmospheric and Terrestrial Physics* 46 (5), 419 – 429.
URL <http://www.sciencedirect.com/science/article/pii/0021916984900862>
- Campbell, W. H., 1982. Annual and semiannual changes of the quiet daily variations (sq) in the geomagnetic field at north american locations. *Journal of Geophysical Research: Space Physics* 87 (A2), 785–796.
URL <https://agupubs.onlinelibrary.wiley.com/doi/abs/10.1029/JA087iA02p00785>
- Campbell, W. H., 1997. *Introduction to Geomagnetic Fields*, 1st Edition. Vol. 1. Cambridge University Press, The Edinburgh Building, Cambridge, CB2 2RU, United Kingdom.
- Chapman, S., 1951. The equatorial electrojet as detected from the abnormal electric current distribution above huancayo, peru, and elsewhere. *Arch. Met. Geoph. Biokl. A*, 368–390.
- Chapman, S., Bartels, J., 1940. *Geomagnetism*. Vol. 1 and 2. Oxford University Press, Amen House, London E.C.4.
- Chapman, S., Dyson, F. W., 1919. I. the solar and lunar diurnal variations of terrestrial magnetism. *Philosophical Transactions of the Royal Society of London. Series A, Containing Papers of a Mathematical or Physical Character* 218 (561-569), 1–118.
URL <https://royalsocietypublishing.org/doi/abs/10.1098/rsta.1919.0001>

- Chapman, S., Rao, K., 1965. The h and z variations along and near the equatorial electrojet in india, africa and the pacific. *Journal of Atmospheric and Terrestrial Physics* 27 (4), 559 – 581.
URL <http://www.sciencedirect.com/science/article/pii/0021916965900206>
- Cnossen, I., 2017. The impact of century-scale changes in the core magnetic field on external magnetic field contributions. *Space Science Reviews*.
- Cnossen, I., Richmond, A. D., 2013. Changes in the earth's magnetic field over the past century: Effects on the ionosphere-thermosphere system and solar quiet (sq) magnetic variation. *Journal of Geophysical Research: Space Physics* 118 (2), 849–858.
URL <https://agupubs.onlinelibrary.wiley.com/doi/abs/10.1029/2012JA018447>
- Colomb, F., Alonso, C., Hofmann, C., Nollmann, I., 2004. Sac-c mission, an example of international cooperation. *Advances in Space Research* 34 (10), 2194–2199, *space Science Education and Promoting North-South Partnership in Space Research*.
URL <https://www.sciencedirect.com/science/article/pii/S0273117704000468>
- de Haro Barbas, B. F., Elias, A. G., Cnossen, I., Zossi de Artigas, M., 2013. Long-term changes in solar quiet (sq) geomagnetic variations related to earth's magnetic field secular variation. *Journal of Geophysical Research: Space Physics* 118 (6), 3712–3718.
URL <https://agupubs.onlinelibrary.wiley.com/doi/abs/10.1002/jgra.50352>
- Dieminger, W., Hartmann, G. K., Leitinger, R., 1996. *The Upper Atmosphere*. Springer Berlin, Heidelberg.
- Doumbia, V., Maute, A., Richmond, A. D., 2007. Simulation of equatorial electrojet magnetic effects with the thermosphere-ionosphere-electrodynamics general circulation model. *J. Geophys. Res.* 112, doi:10.1029/2007JA012308.
- Doumouya, V., Cohen, Y., Arora, B., Yumoto, K., 2003. Local time and longitude dependence of the equatorial electrojet magnetic effects. *Journal of Atmospheric and Solar-Terrestrial Physics* 65 (14), 1265–1282, *equatorial Electrojet Studies from Ground and Space*.
URL <https://www.sciencedirect.com/science/article/pii/S1364682603001834>

- Doumouya, V., Vassal, J., Cohen, Y., Fambitakoye, O., Menvielle, M., 1998. Equatorial electrojet at african longitudes: first results from magnetic measurements. *Annales Geophysicae* 16 (6), 658–666.
URL <https://angeo.copernicus.org/articles/16/658/1998/>
- Efron, B., 1981. Nonparametric estimates of standard error: The jackknife, the bootstrap, and other methods. *Biometrika* 68, 589–599.
- Elias, A. G., de Artigas, M. Z., de Haro Barbas, B. F., 2010. Trends in the solar quiet geomagnetic field variation linked to the earth’s magnetic field secular variation and increasing concentrations of greenhouse gases. *Journal of Geophysical Research: Space Physics* 115 (A8).
URL <https://agupubs.onlinelibrary.wiley.com/doi/abs/10.1029/2009JA015136>
- England, S. L., Maus, S., Immel, T. J., Mende, S. B., 2006. Longitudinal variation of the E-region electric fields caused by atmospheric tides. *Geophys. Res. Lett* 33, doi:10.1029/2006GL027465.
- Fambitakoye, O., Mayaud, P., 1976. Equatorial electrojet and regular daily variation sr—i. a determination of the equatorial electrojet parameters. *Journal of Atmospheric and Terrestrial Physics* 38 (1), 1–17.
URL <https://www.sciencedirect.com/science/article/pii/0021916976901884>
- Fang, T.-w., Akmaev, R., Fuller-Rowell, T., Wu, F., Maruyama, N., Millward, G., 2013. Longitudinal and day-to-day variability in the ionosphere from lower atmosphere tidal forcing. *Geophys. Res. Lett.* 40, 2523–2528.
- Farquharson, C. G., Oldenburg, D. W., 07 1998. Non-linear inversion using general measures of data misfit and model structure. *Geophysical Journal International* 134 (1), 213–227.
URL <https://doi.org/10.1046/j.1365-246x.1998.00555.x>
- Finlay, C. C., Olsen, N., Kotsiaros, S., Gillet, N., Tøffner-Clausen, L., 2016. Recent geomagnetic secular variation from swarm and ground observatories as estimated in the chaos-6 geomagnetic field model. *Earth, Planets and Space* 68.
- Forbes, J., 1981. The Equatorial Electrojet. *Rev. Geophys.* 19, 469–504.
- Forbes, J. M., Zhang, X., Palo, S., Russel, J., Mertens, C. J., Mlynczak, M., 2008. Tidal variability in the ionospheric dynamo region. *J. Geophys. Res.* 113, doi:10.1029/2007JA012737.

- Friis-Christensen, E., Luhr, H., Hulot, G., 2006. Swarm: A constellation to study the earth's magnetic field. *Earth, Planets and Space* 58.
- Friis-Christensen, E., Luhr, H., Knudsen, D., Haagmans, R., 2008. Swarm—an earth observation mission investigating geospace. *Advances in Space Research* 41.
- Gama, L. I., 1953. Observações da amplitude diurna da componente horizontal do campo magnética na ilha de fernando de noronha. Publicações do Observatório Magnético de Vassouras, Ministério da Educação e Cultura, Observatório Nacional, Rio de Janeiro, Brasil 2.
- Gama, L. I., 1958. Installation of the tatuoca magnetic observatory. Publicações do Serviço Magnético, Ministério da Educação e Cultura, Observatório Nacional, Rio de Janeiro, Brasil 6.
- Gama, L. I., 1964. Resultados magnéticos – tatuoca 1959-62. Publicações do Serviço Magnético, Ministério da Educação e Cultura, Observatório Nacional, Rio de Janeiro, Brasil 12.
- Gama, L. I., 1972. Sobre a variação diurna do campo magnético no brasil. Publicações de Geomagnetismo, Ministério da Educação e Cultura, Observatório Nacional, Rio de Janeiro, Brasil 15.
- Gonzalez, W. D., Joselyn, J. A., Kamide, Y., Kroehl, H. W., Rostoker, G., Tsurutani, B. T., Vasyliunas, V. M., 1994. What is a geomagnetic storm? *Journal of Geophysical Research: Space Physics* 99 (A4), 5771–5792.
URL <https://agupubs.onlinelibrary.wiley.com/doi/abs/10.1029/93JA02867>
- Gouin, P., 1962. Reversal of the magnetic daily variation at addis ababa. *Nature* 193.
- Gurubaran, S., 2002. The equatorial counter electrojet: Part of a worldwide current system? *Geophysical Research Letters* 29.
- Hagan, M. E., Burrage, M., Forbes, J. M., Hackney, J., Randel, W. J., Zhang, X., 1999. GSWM-98: Results for migrating solar tides. *J. Geophys. Res.* 104, 6813–6827.
- Hagan, M. E., Forbes, J. M., 2002. Migrating and nonmigrating diurnal tides in the middle and upper atmosphere excited by tropospheric latent heat release. *J. Geophys. Res* 107.

- Hagan, M. E., Forbes, J. M., 2003. Migrating and nonmigrating semidiurnal tides in the upper atmosphere excited by tropospheric latent heat release. *J. Geophys. Res.* 108.
- Hamid, N., Liu, H., Uozumi, T., Yoshikawa, A., 2015. Empirical model of equatorial electrojet based on ground-based magnetometer data during solar minimum in fall. *Earth Planets Space* 67.
- Hamid, N., Liu, H., Uozumi, T., Yumoto, K., Veenadhari, B., Yoshikawa, A., Sanchez, J. A., 2014. Relationship between the equatorial electrojet and global sq currents at the dip equator region. *Earth Planets Space* 66.
- Hansen, P. C., 2010. *Discrete Inverse Problems*. SIAM Society for Industrial and Applied Mathematics, Philadelphia.
- Hanuise, C., Mazaudier, C., Vila, P., Blanc, M., Crochet, M., 1983. Global dynamo simulation of ionospheric currents and their connection with the equatorial electrojet and counter electrojet: A case study. *Journal of Geophysical Research* 88.
- Hartmann, G. A., Pacca, I. G., 2009. Time evolution of the south atlantic magnetic anomaly. *An. Acad. Bras. Ciênc.* 81.
- Heelis, R., 2004. Electrodynamics in the low and middle latitude ionosphere: a tutorial. *Journal of Atmospheric and Solar-Terrestrial Physics* 66 (10), 825–838, upper Atmosphere Tutorials from the 2001 Joint CEDAR SCOSTEP Meeting.
URL <https://www.sciencedirect.com/science/article/pii/S1364682604000525>
- Hesse, D., 1982. An investigation of the equatorial electrojet by means of ground based magnetic measurements in brazil. *Annales Geophysicae* 38, 315–320.
- Holton, J. R., 2004. *An Introduction to Dynamic Meteorology*, 4th Edition. Vol. 88. Elsevier Academic Press, 200 Wheeler Road, Burlington, MA 01803, USA.
- Jankowsky, J., Sucksdorff, C., 1996. *Guide for magnetic measurements and observatory practice*. Vol. 1. IAGA, iISBN: 0-9650686-2-5.
- Jones, C., 2007. *Geodynamo*. Springer Netherlands, Dordrecht, pp. 287–296.
URL https://doi.org/10.1007/978-1-4020-4423-6_108
- Kamide, Y., Chian, A., 2007. *Handbook of the Solar-Terrestrial Environment*. Springer Berlin Heidelberg.
URL <https://books.google.com.br/books?id=gCqLlEs2fHoC>

- Kelley, M. C., 2009. *The Earth's Ionosphere Plasma Physics and Electrodynamics*, 2nd Edition. Elsevier Academic Press, 30 Corporate Drive, Suite 400, Burlington, MA 01803, USA.
- Kil, H., Oh, S.-J., Kelley, M. C., Paxton, L. J., England, S. L., Talaat, E., Min, K.-W., Su, S.-Y., 2007. Longitudinal structure of the vertical $e \times b$ drift and ion density seen from rocsat-1. *Geophysical Research Letters* 34 (14). URL <https://agupubs.onlinelibrary.wiley.com/doi/abs/10.1029/2007GL030018>
- Kivelson, M. G., Russell, C. T., 1995. *Introduction to Space Physics*, 1st Edition. Cambridge University Press, The Edinburgh Building, Cambridge, CB2 2RU, United Kingdom.
- Kusnierkiewicz, D. Y., 2003. *An Overview of the TIMED Spacecraft*. Tech. rep., JHU/APL Technical Digest.
- Liu, H.-L., 2016. Variability and predictability of the space environment as related to lower atmosphere forcing. *Space Weather* 14 (9), 634–658. URL <https://agupubs.onlinelibrary.wiley.com/doi/abs/10.1002/2016SW001450>
- Love, J. J., 2009. Missing data and the accuracy of magnetic-observatory hour means. *Ann. Geophys.* 27, 3601–3610.
- Lühr, H., Manoj, C., 2013. The complete spectrum of the equatorial electrojet related to solar tides: Champ observations. *Ann. Geophys.* 31, 1315–1331.
- Lühr, H., Maus, S., Rother, M., 2004. Noon-time equatorial electrojet: Its spatial features as determined by the champ satellite. *J. Geophys. Res* 109.
- Lühr, H., Rother, M., Häusler, K., Alken, P., Maus, S., 2008. The influence of non-migrating tides on the longitudinal variation of the equatorial electrojet. *J. Geophys. Res* 113.
- Malin, S. R. C., 1970. Separation of Lunar Daily Geomagnetic Variations into Parts of Ionospheric and Oceanic Origin. *Geophysical Journal International* 21 (5), 447–455. URL <https://doi.org/10.1111/j.1365-246X.1970.tb01781.x>
- Malin, S. R. C., 1973. Worldwide distribution of geomagnetic tides. *Philosophical Transactions of the Royal Society of London. Series A, Mathematical and Physical Sciences* 274 (1243), 551–594.

URL <https://royalsocietypublishing.org/doi/abs/10.1098/rsta.1973.0076>

- Malin, S. R. C., Chapman, S., 01 1970. The Determination of Lunar Daily Geophysical Variations by the Chapman-Miller Method. *Geophysical Journal International* 19 (1), 15–35.
URL <https://doi.org/10.1111/j.1365-246X.1970.tb06738.x>
- Manoj, C., Lühr, H., Maus, S., Nagarajan, N., 2006. Evidence for short spatial correlation lengths of the noon-time equatorial electrojet - inferred from a comparison of satellite and ground magnetic data. *J. Geophys. Res* 111.
- Marriott, R. T., Richmond, A. D., Venkateswaran, S. V., 1979. The quiet-time equatorial electrojet and counter-electrojet. *J. Geomag. Geoelectr.* 31, 1979.
- Marsh, D., Mills, M., Kinnison, D., Lamarque, J.-F., 2013. Climate change from 1850 to 2005 simulated in cesm1(waccm). *Journal of Climate* 26.
- Matzka, J., Chulliat, A., Manda, M., Finlay, C. C., Qamili, E., 2010. Geomagnetic observations for main field studies: From ground to space. *Space. Sci. Rev.* 155, 29–64.
- Matzka, J., Siddiqui, T., Lilienkamp, H., Stolle, C., Veliz, O., 2017. Quantifying solar flux and geomagnetic main field influence on the equatorial ionospheric current system at the geo-magnetic observatory huancayo.
- Matzka, J., Stolle, C., Yamazaki, Y., Bronkalla, O., Morschhauser, A., 2021. The geomagnetic kp index and derived indices of geomagnetic activity. *Space Weather* 19 (5), e2020SW002641, e2020SW002641 2020SW002641.
URL <https://agupubs.onlinelibrary.wiley.com/doi/abs/10.1029/2020SW002641>
- Maus, S., Lühr, H., 2005. Signature of the quiet-time magnetospheric magnetic field and its electromagnetic induction in the rotating earth. *Geophysical Journal International*.
- Maus, S., Yin, F., Lühr, H., Manoj, C., Rother, M., Rauberg, J., Michaelis, I., Stolle, C., Müller, R. D., 2008. Resolution of direction of oceanic magnetic lineations by the sixth-generation lithospheric magnetic field model from champ satellite magnetic measurements. *Geochemistry, Geophysics, Geosystems*.

- Mayaud, P. N., 1977. The equatorial counter-electrojet - a review of its geomagnetic aspects. *Journal of Atmospheric and Solar-Terrestrial Physics* 39.
- Miyahara, S., Ooishi, M., 1997. Variation of sq induced by atmospheric tides simulated by a middle atmosphere general circulation model. *J. Geomagn. Geoelectr.* 49, 77–87.
- Miyoshi, Y., Pancheva, D., Mukhtarov, P., Jin, H., Fujiwara, H., Shinagawa, H., 2017. Excitation mechanism of non-migrating tides. *J. Atmos. Sol. Terr. Phys.* 156, 24–36.
- Morschhauser, A., Soares, G. B., Haseloff, J., Bronkalla, O., Protásio, J., Pinheiro, K., Matzka, J., 2017. The geomagnetic observatory on tatuoca island, brazil: History and recent developments. *Geoscientific Instrumentation, Methods and Data Systems* 6.
- Neubert, T., Manda, M., Hulot, G., von Frese, R., Primdahl, F., Jørgensen, J. L., Friis-Christensen, E., Stauning, P., Olsen, N., Risbo, T., 2001. Ørsted satellite captures high-precision geomagnetic field data. *Eos, Transactions American Geophysical Union* 82 (7), 81–88.
 URL <https://agupubs.onlinelibrary.wiley.com/doi/abs/10.1029/2001E000043>
- Oberheide, J., Forbes, J. M., Häusler, K., Wu, Q., Bruinsma, S. L., 2009. Tropospheric tides from 80 to 400 km: Propagation, interannual variability, and solar cycle effects. *Journal of Geophysical Research: Atmospheres* 114 (D1).
 URL <https://agupubs.onlinelibrary.wiley.com/doi/abs/10.1029/2009JD012388>
- Oberheide, J., Forbes, J. M., Zhang, X., Bruinsma, S. L., 2011. Climatology of upward propagating diurnal and semidiurnal tides in the thermosphere. *Journal of Geophysical Research: Space Physics* 116 (A11).
 URL <https://agupubs.onlinelibrary.wiley.com/doi/abs/10.1029/2011JA016784>
- Olsen, J., 1951. Results of magnetic observations made at tatuoca (brazil) september 1933-january 1934. Temporary Commission on the Liquidation of the Polar Year 1932-33, International Meteorological Organization, Copenhagen.

- Olsen, N., Glassmeier, K.-H., Jia, X., May 2010. Separation of the magnetic field into external and internal parts. *Space Science Reviews* 152 (1), 135–157.
URL <https://doi.org/10.1007/s11214-009-9563-0>
- Olsen, N., Stolle, C., 2012. Satellite geomagnetism. *Annu. Rev. Earth Planet. Sci.* 40, 441–65.
- Onwumechili, C., 1997. *The Equatorial Electrojet*. Gordon and Breach, Newark.
- Onwumechili, C., Ezema, P., 1992. Latitudinal and vertical parameters of the equatorial electrojet from an autonomous data set. *Journal of Atmospheric and Terrestrial Physics* 54 (11), 1535–1544.
URL <https://www.sciencedirect.com/science/article/pii/002191699290161D>
- Onwumechili, C. A., 1992. Study of the return current of the equatorial electrojet. *Journal of Geomagnetism and Geoelectricity* 44.
- Picone, J. M., Hedin, A. E., Drob, D. P., Aikin, A. C., 2002. Nrlmsise-00 empirical model of the atmosphere: Statistical comparisons and scientific issues. *Journal of Geophysical Research: Space Physics* 107 (A12), SIA 15–1–SIA 15–16.
URL <https://agupubs.onlinelibrary.wiley.com/doi/abs/10.1029/2002JA009430>
- Qian, L., Burns, A. G., Emery, B. A., Foster, B., Lu, G., Maute, A., Richmond, A. D., Roble, R. G., Solomon, S. C., Wang, W., 2014. The near tie-gcm. In: Huba, J., Schunk, R., Khazanov, G. (Eds.), *Modeling the Ionosphere-Thermosphere System*. Wiley, Chichester, U. K.
- Rastogi, R., Chandra, H., James, M. a. e. a., 2008. Characteristics of the equatorial electrojet current in the central region of south america. *Earth Planets Space* 60.
- Rastogi, R. G., 1974. Westward equatorial electrojet during daytime hours. *J. Geophys. Res.* 379, 1503–1512.
- Rastogi, R. G., Alex, S., Patil, A., 1994. Seasonal variations of geomagnetic d, h and z fields at low latitudes. *Journal of geomagnetism and geoelectricity* 46 (2), 115–126.
- Rastogi, R. G., Chandra, H., Yumoto, K., 2010. Equatorial electrojet in east Brazil longitudes. *Journal of Earth System Science* 119.

- Rastogi, R. G., Iyer, K. N., 1976. Quiet day variation of geomagnetic H-field at low latitudes. *Journal of Geomagnetism and Geoelectricity* 28, 461–479.
- Rastogi, R. G., Trivedi, N. B., 2009. Asymmetries in the equatorial electrojet around n-e brazil sector. *Annales Geophysicae* 27 (3), 1233–1249.
URL <https://angeo.copernicus.org/articles/27/1233/2009/>
- Rastogi, R. G., Yumoto, K., 2007. Equatorial electrojet in the East Brazil anomaly region. *Earth Planets Space* 59.
- Reigber, C., Lühr, H., Schwintzer, P., 2002. Champ mission status. *Adv. Space Res.* 30 (2), 129–134.
- Richmond, A., 1973. Equatorial electrojet—i. development of a model including winds and instabilities. *Journal of Atmospheric and Terrestrial Physics* 35 (6), 1083–1103.
URL <https://www.sciencedirect.com/science/article/pii/002191697390007X>
- Richmond, A. D., 1995. *Ionospheric electrodynamics*. CRC Press, Boca Raton, pp. 249–290.
URL <https://doi.org/10.1201/9780203713297>
- Richmond, A. D., 2011. *Electrodynamics of Ionosphere–Thermosphere Coupling*. Springer Netherlands, Dordrecht, pp. 191–201.
URL https://doi.org/10.1007/978-94-007-0326-1_13
- Richmond, A. D., Maute, A., 2014. *Ionospheric Electrodynamics Modeling*. American Geophysical Union (AGU), Ch. 6, pp. 57–71.
URL <https://agupubs.onlinelibrary.wiley.com/doi/abs/10.1002/9781118704417.ch6>
- Richmond, A. D., Ridley, E. C., Roble, R. G., 1992. A thermosphere/ionosphere general circulation model with coupled electrodynamics. *Geophys. Res. Lett.* 19, 601–604.
- Richmond, A. D., Roble, R. G., 1987. Electrodynamic effects of thermospheric winds from the near thermospheric general circulation model. *Journal of Geophysical Research: Space Physics* 92 (A11), 12365–12376.
URL <https://agupubs.onlinelibrary.wiley.com/doi/abs/10.1029/JA092iA11p12365>

- Rigoti, A., Chamalaun, F. H., Trivedi, N. B., Padilha, A., 1999. Characteristics of the equatorial electrojet determined from an array of magnetometers in n-ne brazil. *Earth Planets Space* 51.
- Roble, R., 1992. The polar lower thermosphere. *Planetary and Space Science* 40 (2), 271–297.
URL <https://www.sciencedirect.com/science/article/pii/003206339290065V>
- Russell III, J. M., Mlynczak, M. G., Gordley, L. L., Jr., J. J. T., Esplin, R. W., 1999. Overview of the SABER experiment and preliminary calibration results. In: Larar, A. M. (Ed.), *Optical Spectroscopic Techniques and Instrumentation for Atmospheric and Space Research III*. Vol. 3756. International Society for Optics and Photonics, SPIE, pp. 277 – 288.
URL <https://doi.org/10.1117/12.366382>
- Saur, J., Neubauer, F. M., Glassmeier, K.-H., May 2010. Induced magnetic fields in solar system bodies. *Space Science Reviews* 152 (1), 391–421.
URL <https://doi.org/10.1007/s11214-009-9581-y>
- Shume, E. B., Denardini, C. M., de Paula, E. R., Trivedi, N. B., 2010. Variabilities of the equatorial electrojet in Brazil and Perú. *J. Geophys. Res.* 115, doi:10.1029/2009JA014984.
- Singh, D., Gurubaran, S., He, M., 2018. Evidence for the Influence of DE3 Tide on the Occurrence of Equatorial Counterelectrojet. *Geophys. Res. Lett* 45, 2145–2150, doi:10.1002/2018GL077076.
- Soares, G., 2018. ANALYSIS OF THE EQUATORIAL COUNTER ELECTROJET LONGITUDINAL VARIATIONS. thesis, Observatório Nacional.
- Soares, G., Yamazaki, Y., Matzka, J., Pinheiro, K., Morschhauser, A., Stolle, C., Alken, P., 2018a. Equatorial counter electrojet longitudinal and seasonal variability in the american sector. *Journal of Geophysical Research: Space Physics* 123 (11), 9906–9920.
URL <https://agupubs.onlinelibrary.wiley.com/doi/abs/10.1029/2018JA025968>
- Soares, G., Yamazaki, Y., Matzka, J. e. a., 2019a. Longitudinal variability of the equatorial counter electrojet during the solar cycle 24. *Studia Geophysica et Geodaetica* 63, 1573–1626.
URL <https://doi.org/10.1007/s11200-018-0286-0>

- Soares, G. B., Matzka, J., Pinheiro, K., 2018b. Preliminary minute means geomagnetic observatory tatuoca (ttb), 2008 to 2017. GFZ Data Services 1.
URL <http://doi.org/10.5880/GFZ.2.3.2018.005>
- Soares, G. B., Matzka, J., Pinheiro, K., Martins, C., Rosales, D., Vidal, E., 2020. Hourly mean values of the geomagnetic field horizontal component h at the geomagnetic observatories tatuoca (ttb) and huancayo (hua), 1957 to 2019. GFZ Data Services 1.
URL <https://doi.org/10.5880/GFZ.2.3.2020.002>
- Soares, G. B., Yamazaki, Y., Matzka, J., Pinheiro, K., Stolle, C., Alken, P., Yoshikawa, A., Uozumi, T., Fujimoto, A., Kulkarni, A., 2019b. Longitudinal variability of the equatorial counter electrojet during the solar cycle 24. *Studia Geophysica et Geodaetica* 63.
- Soares, G. B., Yamazaki, Y., Morschhauser, A., Matzka, J., Pinheiro, K., 2022. Pceej equatorial electrojet model data for years 2003-2010 and 2014-2018. GFZ Data Services 1.
URL <https://doi.org/10.5880/GFZ.2.3.2022.003>
- St-Louis, B., 2011. INTERMAGNET Technical Reference Manual, Version 4.5. Tech. rep., INTERMAGNET.
- Stening, R. J., 1995. Variations in the strength of the sq current system. *Annales Geophysicae* 13 (6), 627–632.
URL <https://angeo.copernicus.org/articles/13/627/1995/>
- Stolle, C., Manoj, C., Luhr, H., Maus, S., Alken, P., 2008. Estimating the daytime equatorial ionization anomaly strength from electric field proxies. *J. Geophys. Res* 113.
- Sugiura, M., Poros, D. J., 1969. An improved model equatorial electrojet with a meridional current system. *Journal of Geophysical Research* (1896-1977) 74 (16), 4025–4034.
URL <https://agupubs.onlinelibrary.wiley.com/doi/abs/10.1029/JA074i016p04025>
- Takeda, M., 1996. Effects of the strength of the geomagnetic main field strength on the dynamo action in the ionosphere. *Journal of Geophysical Research: Space Physics* 101.
- Takeda, M., 1999. Time variation of global geomagnetic sq field in 1964 and 1980. *Journal of Atmospheric and Solar-Terrestrial Physics* 61 (10), 765–774.

URL <https://www.sciencedirect.com/science/article/pii/S1364682699000280>

Takeda, M., 2013. Contribution of wind, conductivity, and geomagnetic main field to the variation in the geomagnetic sq field. *Journal of Geophysical Research: Space Physics* 118.

Tapping, K. F., 2013. The 10.7 cm solar radio flux (f10.7). *Space Weather* 11, 394–406.

URL <https://agupubs.onlinelibrary.wiley.com/doi/abs/10.1002/swe.20064>

Tarpley, J., 1973. Seasonal movement of the sq current foci and related effects in the equatorial electrojet. *Journal of Atmospheric and Terrestrial Physics* 35 (6), 1063 – 1071.

URL <http://www.sciencedirect.com/science/article/pii/0021916973900056>

Teitelbaum, H., Vial, F., 1991. On tidal variability induced by nonlinear interaction with planetary waves. *J. Geophys. Res. Sp. Phys.* 96.

Thébault, E., Purucker, M., Whaler, K. A., Langlais, B., Sabaka, T. J., Aug 2010. The magnetic field of the earth's lithosphere. *Space Science Reviews* 155 (1), 95–127.

URL <https://doi.org/10.1007/s11214-010-9667-6>

Thébault, E., Finlay, C. C., D.Beggan, C., Alken, P., Aubert, J., Barrois, O., Bertrand, F., Bondar, T., Boness, A., Brocco, L., et al., 2015. International Geomagnetic Reference Field: the 12th generation. *Earth Planets Space* 67, doi:10.1186/s40623-015-0228-9.

Torta, J. M., Marsal, S., Curto, J. J., Gaya-Piqué, L. R., Mar 2010. Behaviour of the quiet-day geomagnetic variation at livingston island and variability of the sq focus position in the south american-antarctic peninsula region. *Earth, Planets and Space* 62 (3), 297–307.

URL <https://doi.org/10.5047/eps.2009.11.004>

Wardinski, I., 2007. *Geomagnetic Secular Variation*. Springer Netherlands, Dordrecht, pp. 346–350.

URL https://doi.org/10.1007/978-1-4020-4423-6_125

Weimer, D. R., 2005. Improved ionospheric electrodynamic models and application to calculating joule heating rates. *Journal of Geophysical Research: Space*

Physics 110 (A5).

URL <https://agupubs.onlinelibrary.wiley.com/doi/abs/10.1029/2004JA010884>

Wienert, K. A., 1970. Notes on geomagnetic observatory and survey practice. Vol. 1. UNESCO.

Winch, D., 2007. Periodic External fields. Springer Netherlands, Dordrecht, pp. 809–816.

URL https://doi.org/10.1007/978-1-4020-4423-6_262

Yamazaki, Y., Kosch, M. J., 2014. Geomagnetic lunar and solar daily variations during the last 100 years. *Journal of Geophysical Research: Space Physics* 119 (8), 6732–6744.

URL <https://agupubs.onlinelibrary.wiley.com/doi/abs/10.1002/2014JA020203>

Yamazaki, Y., Maute, A., 2017. Sq and eej—a review on the daily variation of the geomagnetic field caused by ionospheric dynamo currents. *Space. Sci. Rev.* 206, 299–405.

Yamazaki, Y., Richmond, A. D., Maute, A., Liu, H., Pedatella, N., Sassi, F., 2014a. On the day-to-day variation of the equatorial electrojet during quiet periods. *J. Geophys. Res. Space Physics* 119, 6966–6980.

Yamazaki, Y., Richmond, A. D., Maute, A., Wu, Q., Ortland, D. A., Yoshikawa, A., Adimula, I. A., Rabiou, B., Kunitake, M., Tsugawa, T., 2014b. Ground magnetic effects of the equatorial electrojet simulated by the tie-gcm driven by timed satellite data. *J. Geophys. Res. Space Physics* 119.

Yamazaki, Y., Stolle, C., Matzka, J., Liu, H., Tao, C., 2018. Interannual variability of the daytime equatorial ionospheric electric field. *J. Geophys. Res. Space Physics* 123, 4241–4256.

Yamazaki, Y., Yumoto, K., Cardinal, M., et al., 2011. An empirical model of the quiet daily geomagnetic field variation. *Journal of Geophysical Research* 116.

Yamazaki, Y., Yumoto, K., Uozumi, T., Abe, S., Cardinal, M. G., McNamara, D., Marshall, R., Shevtsov, B. M., Solov'yev, S. I., 2010. Reexamination of the sq-eej relationship based on extended magnetometer networks in the east asian region. *Journal of Geophysical Research: Space Physics* 115 (A9).

URL <https://agupubs.onlinelibrary.wiley.com/doi/abs/10.1029/2010JA015339>

- Yizengaw, E., Moldwin, M. B., Zesta, E., Biouele, C. M., Damtie, B., Mebrahtu, A., Rabi, B., Valladares, C. F., Stoneback, R., 2014. The longitudinal variability of equatorial electrojet and vertical drift velocity in the african and american sectors. *Ann. Geophys.* 32, 231–238, doi:10.5194/angeo-32-231-2014.
- Zhou, Y.-L., Lüher, H., Alken, P., 2018a. The sidebands of the equatorial electrojet: General characteristic of the westward currents, as deduced from champ. *Journal of Geophysical Research: Space Physics* 123.
- Zhou, Y.-L., Lüher, H., Xu, H.-w., Alken, P., 2018b. Comprehensive analysis of the counter equatorial electrojet: Average properties as deduced from champ observations. *Journal of Geophysical Research: Space Physics* 123.
- Çelik, C., Tunçer, M. K., Tolak-Çiftçi, E., Zobu, M., Oshiman, N., Tank, S. B., 04 2012. Solar and lunar geomagnetic variations in the northwestern part of Turkey. *Geophysical Journal International* 189 (1), 391–399.
URL <https://doi.org/10.1111/j.1365-246X.2012.05382.x>